THE UNIVERSITY *of* EDINBURGH

The effect of perinatal adversity on structural connectivity of the developing brain

Manuel Blesa Cábez

Edinburgh Medical School: Clinical Sciences

University of Edinburgh

This dissertation is submitted for the degree of

Doctor of Philosophy

March 2018

Abstract

Globally, preterm birth (defined as birth at <37 weeks of gestation) affects around 11% of deliveries and it is closely associated with cerebral palsy, cognitive impairments and neuropsychiatric diseases in later life.

Magnetic Resonance Imaging (MRI) has utility for measuring different properties of the brain during the lifespan. Specially, diffusion MRI has been used in the neonatal period to quantify the effect of preterm birth on white matter structure, which enables inference about brain development and injury.

By combining information from both structural and diffusion MRI, is it possible to calculate structural connectivity of the brain. This involves calculating a model of the brain as a network to extract features of interest. The process starts by defining a series of nodes (anatomical regions) and edges (connections between two anatomical regions). Once the network is created, different types of analysis can be performed to find features of interest, thereby allowing group wise comparisons.

The main frameworks/tools designed to construct the brain connectome have been developed and tested in the adult human brain. There are several differences between the adult and the neonatal brain: marked variation in head size and shape, maturational processes leading to changes in signal intensity profiles, relatively lower spatial resolution, and lower contrast between tissue classes in the T1 weighted image. All of these issues make the standard processes to construct the brain connectome very challenging

to apply in the neonatal population. Several groups have studied the neonatal structural connectivity proposing several alternatives to overcome these limitations.

The aim of this thesis was to optimise the different steps involved in connectome analysis for neonatal data. First, to provide accurate parcellation of the cortex a new atlas was created based on a control population of term infants; this was achieved by propagating the atlas from an adult atlas through intermediate childhood spatio-temporal atlases using image registration. After this the advanced anatomically-constrained tractography framework was adapted for the neonatal population, refined using software tools for skull-stripping, tissue segmentation and parcellation specially designed and tested for the neonatal brain. Finally, the method was used to test the effect of early nutrition, specifically breast milk exposure, on structural connectivity in preterm infants. We found that infants with higher exposure to breastmilk in the weeks after preterm birth had improved structural connectivity of developing networks and greater fractional anisotropy in major white matter fasciculi. These data also show that the benefits are dose dependent with higher exposure correlating with increased white matter connectivity.

In conclusion, structural connectivity is a robust method to investigate the developing human brain. We propose an optimised framework for the neonatal brain, designed for our data and using tools developed for the neonatal brain, and apply it to test the effect of breastmilk exposure on preterm infants.

Lay summary

Globally, preterm birth (defined as birth at <37 weeks of gestation) affects around 11% of deliveries and it is closely associated with cerebral palsy, cognitive impairments and neuropsychiatric diseases in later life.

Due to new technological advances in magnetic resonance imaging (MRI) it is possible to map the so called “brain connectome”. That is a map of the connections of the brain, resulting in a matrix which represents the connectivity between different regions of the brain.

To calculate the “brain connectome”, two different MRI acquisitions are involved. Firstly, structural MRI which allows us to identify different cortical regions of interest (ROIs), and secondly, diffusion MRI, which is used to map the brain’s white matter and establish the connections between the different cortical ROIs.

In the last few years researchers have made significant improvements in calculating the “brain connectome”. However, almost all the methods have been designed/tested in the adult human brain, and therefore are not suitable for neonatal infants due to several anatomical differences between the adult and neonatal brain.

The aim of this thesis was to optimise the different steps involved in calculating the “brain connectome” to allow its use in the neonatal brain. First, a new atlas was created based on a healthy newborn population for accurate anatomic labelling of different cortical brain regions. After this, the process of

mapping the white matter connections was optimized by adapting state of the art frameworks designed for the adult human brain to the neonatal brain. Finally, the optimised method was used to test the effect that breast milk may have on the “brain connectome” of a group of preterm infants. We found that infants with higher exposure to breastmilk had improved structural connectivity of developing networks, and these benefits were dose dependent with higher exposure correlating with increased white matter integrity.

In conclusion, structural connectivity is a powerful tool to investigate the developing human brain. We propose an optimised framework for the neonatal brain and apply it to test the effect of the breastmilk exposure in preterm infants.

Declaration

I declare that this thesis was composed by myself, that the work contained herein is my own except where explicitly stated otherwise in the text, and that this work has not been submitted for any other degree or processional qualification.

Parts of this work have been published in:

Blesa M, Serag A, Wilkinson AG, Anblagan D, Telford EJ, Pataky R, Sparrow SA, Macnaught G, Semple SI, Bastin ME and Boardman JP (2016) Parcellation of the Healthy Neonatal Brain into 107 Regions Using Atlas Propagation through Intermediate Time Points in Childhood. Front. Neurosci. 10:220. doi: 10.3389/fnins.2016.00220

Manuel Blesa Cábez

Acknowledgements

Firstly, I would like to express my sincere gratitude to my supervisors Prof. James P. Boardman, Dr. Mark E. Bastin and Dr. Ahmed Serag for their support, patience and motivation. Their guidance helped me in all the time of research and writing of this thesis.

I would like also to thank my different labmates who help me during all my Ph.D studies, especially with all the clinical data and the acquisition process, without them this work won't be possible. I also want to mention my friends from different departments for the stimulating discussions, for the sleepless nights we were working together before deadlines, and for all the fun we have had in the last years.

Also I would like to thank to my girlfriend, Sara Medina, for her unconditional support during all the stages of my Ph.D, especially during the stages of frustration and despair.

Last but not the least, I would like to thank my family. My parents and my sister for supporting me spiritually throughout writing this thesis and my life in general, without their support, I won't be here. I would like to make special mention to my uncle, who recently passed away.

Publications

Published journal papers

Monnelly VJ, Anblagan D, Quigley A, **Cabez MB**, Cooper ES, Mactier H, Semple SI, Bastin ME and Boardman JP (2018). **Prenatal methadone exposure is associated with altered neonatal brain development.** NeuroImage: Clinical. 2018;18:9-14.

Dickie DA, Shenkin SD, Anblagan D, Lee J, **Blesa Cabez M**, Rodriguez D, Boardman JP, Waldman A, Job DE and Wardlaw JM (2017) **Whole Brain Magnetic Resonance Image Atlases: A Systematic Review of Existing Atlases and Caveats for Use in Population Imaging.** Front. Neuroinform. 11:1. doi: 10.3389/fninf.2017.00001

Blesa M, Serag A, Wilkinson AG, Anblagan D, Telford EJ, Pataky R, Sparrow SA, Macnaught G, Semple SI, Bastin ME and Boardman JP (2016) **Parcellation of the Healthy Neonatal Brain into 107 Regions Using Atlas Propagation through Intermediate Time Points in Childhood.** Front. Neurosci. 10:220. doi: 10.3389/fnins.2016.00220

Serag A, **Blesa M**, Moore EJ, Pataky R, Sparrow SA, Wilkinson AG, Macnaught G, Semple SI and Boardman JP (2016). **Accurate Learning with Few Atlases (ALFA): an algorithm for MRI neonatal brain extraction and comparison with 11 publicly available methods.** Scientific Reports. 2016;6:23470.

Submitted journal papers

Blesa M, Sullivan G, Anblagan D, Telford EJ, Quigley AJ, Sparrow SA, Serag A, Semple SI, Bastin ME and Boardman JP **Early breast milk exposure modifies brain connectivity in preterm infants.** NeuroImage. *Under review*.

Conference abstracts

Blesa M, Sullivan G, Telford EJ, Semple SI, Quigley A, Bastin M and Boardman JP. **Early breast milk exposure modifies brain connectivity in preterm infants.**

In Neonatal Society Autumn Meeting (2017)

Blesa M, Serag A, Anblagan D, Telford EJ, Sparrow SA, Semple SI, Bastin ME and Boardman JP. **Fixel-based morphometry detects alterations in specific fibres in association with preterm birth: a proof-of-concept study.**

In International Society for Magnetic Resonance in Medicine (2017)

Blesa M, Serag A, Anblagan D, Telford EJ, Sparrow SA, Semple SI, Bastin ME and Boardman JP. **Anatomically constrained tractography and structural connectome of the neonatal brain.**

In International Society for Magnetic Resonance in Medicine (2017)

Blesa M, Serag A, Wilkinson AG, Anblagan D, Telford EJ, Pataky R, Sparrow SA, Macnaught G, Semple SI, Bastin ME and Boardman JP.

Parcellation of the Healthy Neonatal Brain into 107 Regions Using Atlas Propagation through Intermediate Time Points in Childhood.

In Neonatal Society Summer Meeting (2016) and International Society for Magnetic Resonance in Medicine (2016).

List of contents

List of figures

List of tables

List of abbreviations

5TT	Five tissue type file
ACT	Anatomically-constrained tractography
ALFA	Accurate Learning with Few Atlases
AD	Axial diffusivity
ADC	Apparent diffusion coefficient
ANTS	Advanced Normalization Tools
BET	Brain extraction tool
BPD	Bronchopulmonary dysplasia
CC	Cluster coefficient
CP	Cerebral palsy
CPL	Characteristic path length
cSD	Constrained spherical deconvolution
CSF	Cerebrospinal fluid
cUS	Cranial ultrasonography
DEBM	Donor expressed breast milk
dGM	Deep grey matter
DTI	Diffusion tensor imaging
dMRI	Diffusion magnetic resonance imaging
EBC	Edinburgh birth cohort
EPI	Echo-planar imaging
FA	Fractional anisotropy
FDR	False discovery rate

FFD	Free form deformation
FOD	Fibre orientation distributions
FSL	FMRIB's software library
GA	Gestational age
GE	Global efficiency
GMH	Germinal matrix haemorrhage
GM	Grey matter
GMWMI	Grey matter-white matter interface
HCA	Histological chorioamnionitis
HMF	Human Milk Fortifier
IQ	Intelligence quotient
IVH	Intraventricular heamorrhage
LE	Local efficiency
LIFE	Linear fascicle evaluation
MD	Mean diffusivity
MRI	Magnetic resonance imaging
NBS	Network-based statistics
NODDI	Neurite orientation dispersion and density imaging
PVE	Periventricular echogenicity
PVL	Periventricular leukomalacia
RD	Radial diffusivity
ROI	Region of interest
SEGMA	Automatic SEGMentation Approach
SIFT	Spherical-deconvolution informed filtering of tractograms

sMRI	Structural magnetic resonance imaging
SW	Small-worldness
TBSS	Tract-based spatial statistics
TDI	Tract-density imaging
TE	Echo time
TFCE	Threshold-free cluster enhancement
TPN	Total parenteral nutrition
TR	Repetition time
WM	White matter
WMA	white matter abnormalities
WMI	white matter injury

1. General Introduction

1.1. Preterm birth

A preterm birth is defined as a birth at less than 37 weeks gestational age (GA) and globally it is estimated to affect around 11% of deliveries every year (1). Prematurity is the leading cause of death in children under the age of 5 years and almost 1 million children die each year due to the complications of a preterm birth (2, 3). In almost all countries with reliable data, preterm birth rates are increasing (1, 4).

A preterm birth can be initiated by multiple mechanisms (5). There are several risk factors associated with preterm birth, including maternal diabetes and high blood pressure, being pregnant with more than one baby, tobacco smoking, a number of vaginal infections, psychological stress, socio-economic deprivation, being very overweight or underweight before pregnancy, being pregnant with a baby resulting from in vitro fertilization, getting pregnant too soon after having a baby or drinking alcohol or using recreational drugs during the pregnancy (5-7). In addition, studies have identified a multitude of underlying biological pathways and possible genetic and epigenetic mechanisms that influence birth timing and baby size (8-12). However, effective prediction of a preterm birth remains difficult, relying on a combination of clinical history, cervical length measurements and biochemical markers such as foetal fibronectin, thereby limiting the effectiveness of targeted interventional strategies (13, 14). Unless required

for other medical reasons, it is recommended not to induce labour before 39 weeks.

1.1.1. Neurodevelopmental Outcome after Preterm Birth

Over 50% of all infants whose GA is less than twenty-six weeks suffer developmental impairment in some form, including behavioural and emotional disturbance, autistic spectrum disorder, attention deficit hyperactivity disorder and psychiatric disease (15-19). Premature infants are at a greater risk of cerebral palsy (CP), cognitive impairment and neuropsychiatric disease later in life (20, 21). These problems persist into adulthood and are greater the earlier the baby is born (22-24).

The lower the gestational age, the proportionally higher the risk of developing CP, which is diagnosed in 20% of premature survivors of less than 26 weeks GA by the age of 6 years (25, 26). To decrease the risk of brain injury and improve outcomes, different medical treatments have been proven, for example, antenatal steroids, antenatal magnesium sulphate, avoidance of postnatal transfer, reducing postnatal sepsis and optimising nutrition (27-30). For instance, early malnutrition influences neurodevelopment and may modify the risk of brain injury associated with a preterm birth. Optimised protein and energy intake in the first 28 days is associated with increased brain growth and fractional anisotropy (FA) (31-33). It has also been shown that breastfeeding, when compared with formula feeding, is associated with

increased performance in intelligence tests amongst the general population, and this effect may be enhanced in low birthweight infants (34-38).

However, CP is not the only adverse consequence that can result from a premature birth: fine motor and coordination impairments are also quite widespread in such populations (39-41). Although the personal impact of these conditions is lower than that of CP, they are likely to contribute to a poor performance in early education, which has been frequently reported with subjects from this cohort (40).

Wood et al. proved using the Bayley Scales of Infant Development that extremely preterm subjects performed significantly worse in mental and psychomotor development experiments compared to term-born control subjects, both tested at 30 months of age (19). It has been found that children born extremely preterm with a mild neurological impairment, performed worse than expected at 6 years of age in comparison to control subjects in experiments which tested their mental abilities in processing sequential and simultaneous information (21, 25).

The previously mentioned neurocognitive outcomes are connected with a variety of disorders that affect domains such as language, learning, attention, memory and behaviour (18, 25, 42, 43).

A high prevalence of sensory morbidity (44, 45) and mild visual or hearing impairment (25, 46) in preterm compared with term groups is also worth mentioning. A lucid summary extracted from “Preterm Birth: Causes, Consequences, and Prevention.” by Behrman, R.E. and Butler, A.S. (2007)

can be found in Table 1.1. The table describes how each study population was defined using birth weight or gestational age, or both.

Table 1.1: Sensory Impairments in Children Born Preterm

						Percentage Severe Impairment	
Study	**Year of Birth**	**No. of Subjects**	**Age (yr)**	**Gestational Age (wk)**	**Birth Weight (g)**	**Visual**	**Hearing**
Vohr et al., 2005 (26)	1997–1998	910	1.8	22–26		1	1.8
		512		27–32		0.4	1.8
Hintz et al., 2005 (47)	1993–1996	355	1.8	<25		2.3	4.3
	1996–1999	467				1.1	2.6
Marlow et al., 2005 (25)	1995	241	6	<26		2	6
Jacobs et al., 2000 (48)	1990–1994	470	1-2	23–26		2	4
Lefebvre et al., 1996 (49)	1987–1992	217	1.5	23–28		0.5	0.5
Wilson-Costello et al., 2005 (50)	1990–1998	145	1.8		<750	1	10
		272			750–999	1	6
		682			<1,000	1	7
Mercier et al., 2005 (51)	1998–2001	2446	2		<1,000	1.4	2.1
Mikkola et al., 2005 (52)	1996–1997	173	5		<1,000	9	4
Hack et al., 2005*	1992–1995	200	8		<1,000	0	2
Hack et al., 2000 (53)	1992–1995	221	1.8		<1,000	1	9
Hansen and Greisen, 2004 (54)	1994–1995	183	5	<28	<1,000	3.3	0
Doyle et al., 2005 (55)	1991–1992	224	8		<1,000	1.3	1.3

* Two percent of the subjects required hearing aids and 14 percent had hearing impairments.

There is also a higher risk of developing behavioural problems when a child is born premature. A common behavioural problem is, for instance, attention deficit disorder (18, 56). Furthermore, there is evidence of a link between an increased incidence of psychiatric symptoms that may be the basis of certain disorders (such as schizophrenia or autism), and preterm teenagers (57). In addition, deficits in cognition that manifest during childhood appear to prevail much later into adult life (58, 59).

Finally, other important somatic impairments such as long-term respiratory impairment (60) or increases in cardiovascular risk (61), are common in preterm populations, but it is difficult to quantify their impact in infancy and early childhood, although these may become more important in later life (62).

1.2. Preterm Brain Injury

A large number of infants who are born prematurely suffer from brain injury, which often underlies neurologic development in the ways that have been described in the previous subsection. Hence, it is of a great importance to public health to investigate these kinds of injuries in order to characterise atypical brain development and to enable investigation of causal pathways to injury and early detection of children at risk of long term impairments.

Preterm brain injury can be classified as haemorrhagic (Germinal Matrix Hemorrhage-Intraventricular Hemorrhage [GMH-IVH]), or ischaemic (periventricular leukomalacia [PVL]).

1.2.1. Germinal Matrix Hemorrhage-Intraventricular Hemorrhage

During the first 48 hours of life, following rupture of the germinal matrix vasculature, there is a high chance of developing GMH-IVH (63-65). GMH usually presents as an asymmetric lesion, involving bleeding from the thin-walled veins within the germinal matrix. If this bleeding occurs in the ventricular system, GMH evolves into IVH. This bleeding may cause obstruction of the medullary veins, resulting in venous hemorrhage and coagulation necrosis of deep periventricular white matter (WM), resulting in a haemorrhagic parenchymal infarction (HPI) (Figure 1.1.).

GMH-IVH and HPI may result in a residual porencephalic cyst near the ventricular or posthemorrhagic hydrocephalus, or both.

1.2.2. Periventricular leukomalacia

It is generally thought that premature brain injuries consist mainly of PVL, which is a cerebral white matter injury (WMI) (66). Recent works have also revealed that PVL is commonly accompanied by neuronal or axonal diseases that affect the cerebral WM, basal ganglia, cerebral cortex, thalamus, brain stem and cerebellum (67). Thus, there is a specific term for when PVL and neuronal/axonal disease appear together; they are generally referred as “encephalopathy of prematurity”.

PVL has two neuropathological components: the focal periventricular necrotic component and diffuse gliosis in the surrounding cerebral WM (Figure 1.1.).

Cystic lesions secondary to necrotic foci in the WM characterize the first component.

It is extremely hard to detect neurodevelopmental impairment due to PVL in newborns and children aged under 6 months. The reason is that PVL shares many symptoms with other medical conditions so infants do not clearly show the signs of impairment, thus, it can take a long time to reach the correct diagnosis, missing a window of opportunity for early interventions to improve outcomes. However, there are some signs that could be sought in order to speed up the PVL identification process such as: vision and/or hearing problems, difficulties with coordination and intellectual or cognitive impairment (59, 67). Neonatal imaging may provide a tool for early identification, taking into account, that MRI predicts adverse motor outcomes slightly better than ultrasound, but both methods are insensitive and neither predicts cognitive problems (68).

1.2.2.1. PVL: Focal brain injury

The focal component of PVL consists of necrosis of the deep periventricular white mater, resulting in a loss of all cellular elements in the area. The necrotic foci can be separated into two types depending on the size of the lesion and the different histopathological evolutions: macroscopic (necrosis > 1 mm which evolves over several weeks into a cyst) and microscopic (necrosis ≤ 1 mm which evolves over several weeks into glial scars) (67).

The nomenclature to differentiate PVL subtypes depends on necrotic foci size but not on the diffuse component. For instance, the macroscopic focal

necrotic component of PVL with diffuse gliosis is referred to as “cystic PVL” (c-PVL). This is a serious injury, but currently its incidence is quite low thanks to improved neonatal intensive care: less than 3% of the infants who suffer very low birth weight (VLBW, less than 1500g) experience it, which accounts for the smallest portion of the PVL population (67, 69, 70).

On the other hand, microscopic focal necroses are called “non cystic PVL” and they occur much more frequently. This type of injury evolves over several weeks, turning into glial scar, which is very difficult to visualize by neuroimaging. The percentage of VLBW preterm babies presenting with this injury is between 20 and 50%.

A common error is to refer to non-cystic PVL as “diffuse PVL” with the purpose of differentiating it from c-PVL, because both c-PVL and non-cystic PVL have one diffuse component and large or small cysts (71).

1.2.2.2. PVL: Diffuse brain injury

The diffuse component of PVL is characterised by an initial decrease in the premyelinating oligodendrocytes (pre-OLs), astrogliosis and microgliosis (72-74). The timing of the appearance and spatial distribution of susceptible OL lineage cells coincides with the magnitude and distribution of acute ischemic injury in several experimental models of WMI, hence its name. The changes in white matter FA with brain maturation observed via MRI correspond closely with maturation of the OL lineage (75).

Although the decrease of the pre-OLs is one of the causes of the diffuse PVL, recent findings support an alternative mechanism where myelination disturbances involve a potentially reversible process linked to arrested pre-OL maturation. Hence, chronic diffuse WMI is characterized by an aberrant response to acute injury, which involves a disrupted regeneration and repair process, whereas pre-OLs are regenerated but remain dysmature (75).

The decrease in pre-OLs is associated with an increase in oligodendroglial progenitors (OPCs), a mechanism that has been observed in several animal models (76). However, when the injury is due to PVL, OPCs do not seem to differentiate correctly into mature oligodentrocytes (the myelin producers), which are often missing their characteristic projections (or processes). As a result, hypomyelination and ventriculomegaly can occur later in the life of the subject (76-79).

The cause for the disturbance in the OPCs maturation is still unknown, but it has been widely documented in an animal model of PVL (80, 81). It was found that the progenitor cells are vulnerable to hypoxic-ischaemic events, which are very frequently seen in premature infants.

The halting of preOL maturation may adversely influence subsequent white matter maturation. Recent studies support the hypothesis that viable OLs and myelination are critical for axon survival (82). Serial neuroimaging studies are needed to better define the progression of WMI in at risk human preterm infants (83-85).

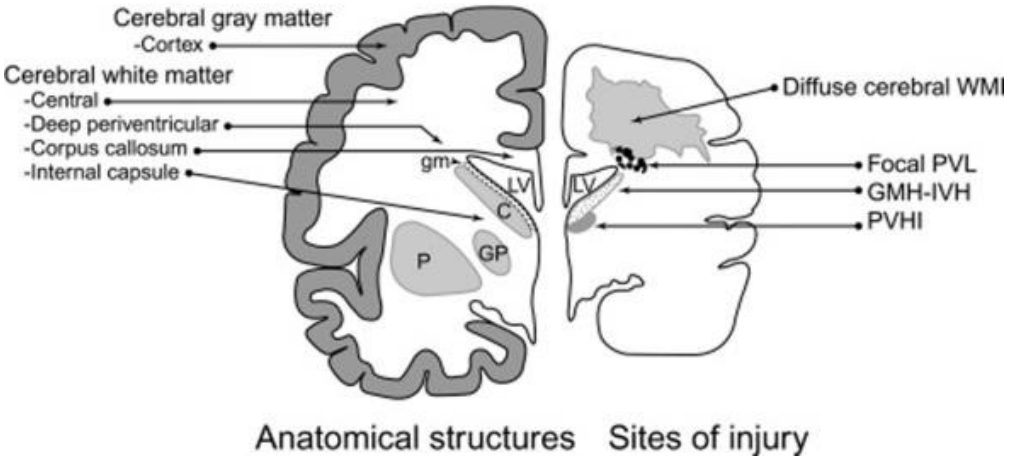

Figure 1.1: Anatomical structures and sites of pathology in the developing brain. The normal anatomical structures at term and the different sites of injury in the preterm brain: diffuse cerebral WMI in the future central cerebral WM, focal (cystic) PVL in the deep periventricular WM, GMH-IVH at the wall of the LV, and PVHI that may be associated with germinal matrix haemorrhage, are shown from left to right (LV = lateral ventricle; C = caudate, P = putamen, GP = globus pallidus). From "Diffuse White Matter Injury and Neurologic Outcomes of Infants Born Very Preterm in the 1990s" by Brunssen and Harry. 2007. Journal of Obsteric, Gynecologic & Neonatal Nursing (86) and "Neurobiology of Periventricular Leukomalacia in the Premature Infant" by Volpe. 2001. Pediatric Research (66).

1.2.3. Detection and grading of the preterm brain injury

The most common way to diagnose preterm brain injury is by cranial ultrasonography (cUS) at the cotside, or by MRI. In cUS examinations, echogenicity is measured, that is the extent to which different surfaces reflect ultrasound waves. Higher echogenicity means that the surface of interest reflects a big portion of the incident sound waves, which enables anatomic inference.

PVL often presents as areas of increased periventricular echogenicity (PVE) relative to the signal from the choroid plexus, when normally the echogenicity of the WM should be lower than that of the choroid plexus. It is often presumed that diffuse periventricular hyperechogenicity is correlated with the diffuse neuropathological component of PVL; however the basis and extent of this correspondence are uncertain (87).

Using the most common classification, PVL is graded into four main types (88, 89):

- **Grade I**: Non-cystic PVL as PVE present for more than seven days, seen in the coronal and sagittal plane, being as or more echogenic than the choroid plexus.
- **Grade II:** PVE evolving into focal cystic lesions.
- **Grade III:** PVE evolving into extensive cystic lesions.
- **Grade IV:** Diffuse echogenicity evolving into periventricular and subcortical cystic lesions.

For the GMH, the most commonly used system is the grading system proposed by Burstein, Papile et al. (90) that includes the following grades:

- **Grade I**: Restricted to the subependymal region/germinal matrix which is seen in the caudothalamic groove.
- **Grade II:** Extension into normal sized ventricles and typically filling less than 50% of the volume of the ventricle.
- **Grade III:** Extension into dilated ventricles.

- **Grade IV:** Grade III with parenchymal haemorrhage.

Nowadays with the increase of MRI in neonatal practice, it is possible to detect brain injury with better definition than with cUS. Moreover, MRI can reveal subtle alterations not visible to ultrasound. For example, it has been found that MRI detects GMH-IVH with double the sensitivity as with cUS (91). The signal of the IVH evolves from isointense to slightly hypointense on T1-weighted (T1w) MRI and to marked hypointense on T2-weighted (T2w) MRI. Following this, the intensity of the signal starts to increase, first on T1w then on T2w MRI. Over the next months, the hemorrhage becomes hypointense on images obtained with both sequences (92).

In PVL, the most common MRI-visible abnormality at term-equivalent age is diffuse and excessively high signal intensity on T2w images (93, 94). In addition, a diffuse abnormal signal intensity can also be seen as a loss in T1w signal and is commonly associated with ventricular dilatation and increased extracerebral cerebrospinal fluid (CSF) which may represent the diffuse component of PVL (95). PVL also shows abnormalities in the diffuse MRI signal and in other water diffusion parameters identified from diffusion MRI, for example the apparent diffusion coefficient (ADC) (96, 97). Although the neurobiological basis of abnormal signal intensities is unclear, it is related to cognitive and behavioural impairments, and the alteration of the mean diffusivity (MD) of the WM in the developing brain, and has been associated with short term measures of neurodevelopmental outcome in infants without focal cerebral lesions (98). These observations are indicative of subtle

microstructural alterations which may reflect a disturbance of normal maturational processes with long-term consequences (66, 99).

A summary of the neuroimaging findings for the different brain injuries can be seen in Table 1.2 (adapted from “Clinical neuroimaging in the preterm infant: Diagnosis and prognosis” by Hinojosa-Rodriguez, M. et al. 2017. Neuroimage: Clinical (71)).

1.2.4. Outcome of the preterm brain injury

GMH and low-grade IVH may resolve by term and do not necessarily increase the risk of an adverse outcome, but moderate to severe IVH (grades III and IV) is associated with high incidences of neurodevelopmental disabilities in surviving infants, such as CP, cognitive, behavioral and visual problems (100-103), although the nature and extent of this disability varies according to the size and location of the haemorrhage (104, 105).

The outcome of the babies with PVL depends on the severity and extension of the injury; going from spastic diplegia, slight developmental delays and deficits in posture, vision systems and motor skills in the patients with minor injuries (106-108), to more extensive signs of brain damage and eventually development of CP (106, 108) or epilepsy (109) in patients with severe PVL. The severity of the CP is related to the level of injury. Those infants with severe PVL have high levels of muscle tone and frequent seizures. When they grow, they may be quadriplegic, exhibiting a loss of function or paralysis of all limbs.

Infants with severe PVL typically begin to exhibit different signs of CP. Some of the abnormal neurological signs can be seen from 36 weeks conceptual age, but is necessary to wait until between six to nine months of age to try to evaluate the definitive signs (110).

A summary of the major clinical outcomes for the different preterm brain injuries can be seen in Table 1.1 (from “Clinical neuroimaging in the preterm infant: Diagnosis and prognosis” by Hinojosa-Rodriguez, M. et al. 2017. Neuroimage: Clinical (71))

Table 1.2: Summary of the different preterm brain injuries

Preterm brain injury detected by MRI	**Neuropathological findings**	**Main clinical outcomes**
Cystic white matter abnormalities (WMA)	Cystic PVL. Often bilateral cysts	Cerebral palsy with diplegia or quadriplegia
	Porencephalic cyst secondary to periventricular hemorrhagic infarction. Often unilateral	Location-dependent. Motor cortex: hemiplegic cerebral palsy
Diffuse WMA	Diffuse component of cystic PVL (moderate-to-severe WMA)	Cognitive impairment/behavioral problems
	Non cystic PVL (mild-to-moderate WMA)	Cognitive impairment/behavioral problems
	Diffuse white matter gliosis (normal-to-mild WMA)	Unknown
Germinal matrix hemorrhage - intraventricular hemorrhage	Breaking of the germinal matrix vessels	Depends on the location and severity Grade III/Periventricular hemorrhagic infarction: cerebral palsy, cognitive, behavioral and visual problems

1.3. Magnetic Resonance Imaging

MRI is a non-invasive imaging technique used in medicine to form pictures of the anatomy and of the physiological processes of the body in both health and disease.

MRI is based on the principle that certain atomic nuclei absorb and emit radio frequency energy when placed in an external magnetic field. In clinical and research MRI, hydrogen atoms are most often used to generate a detectable radio-frequency signal that is received by coils in close proximity to the anatomy being examined. The main reason to use hydrogen atoms is because the average adult human body consists of ~65% water molecules.

The magnetic field aligns the spins of the atoms mainly in two directions, parallel and antiparallel. The intensity of the field and the spin of the atom establish the frequency of the magnetic resonance of the nuclei, and also the proportion of atoms in each one of the states.

This proportion obeys the Maxwell-Boltzmann law, which states that at body temperature, in a field of 1.0 Tesla, both states are nearly equal; only a small excess (~3 x 10^{-6}) of spins can be expected to be found in the lower energy (spin-up) state. The very large number of atoms in a small piece of volume makes it possible to measure the small difference of atoms in different states.

In MRI imaging, an electromagnetic radiation pulse (RF pulse) is emitted at a certain resonance frequency. Nuclei in the parallel or low energy state will

change to the anti-parallel or high energy state, and will return to the low energy state at the end of the RF pulse, emitting energy in form of photons that reflects the difference between energy states. These photons can be detected using proper instruments.

Because the main magnet generates a constant field, all the nuclei that have the same magnetic moment have the same resonance frequency. This means that a signal that causes an MRI in these conditions can be detected, but with the same value of all parts of the body, so there is no spatial information. To solve this problem, gradient coils are added. Each of the coils generates a magnetic field of a certain intensity with a controlled frequency. These magnetic fields alter the magnetic field already present and, therefore, the resonance frequency of the nuclei. By using three orthogonal coils it is possible to assign to each region of the space a different resonance frequency, so that when resonance occurs at a certain frequency it will be possible to determine the region of the space from which it originates.

By modifying the acquisition parameters and pulse sequences it is possible to obtain different signal properties for tissues or physiological processes.

There are three main modalities of MRI: structural MRI (sMRI), diffusion MRI (dMRI) and functional MRI (fMRI). The last method is outside of the scope of this thesis, so I will focus on the other two modalities.

For the sMRI, the most common sequences are T1-weighted (T1w) and T2-weighted (T2w) scans. There are two main parameters to create the different contrasts: the repetition time (TR), that is the length of time between

corresponding consecutive points on a repeating series of pulses and echoes; and the echo time (TE), that is the time between the RF excitation pulse and the centre of the acquired echo signal. To create a T1w image, magnetization is allowed to partially recover before measuring the MR signal by changing the TR. For this purpose, the TR is short. In this acquisition, the TE is also kept short to minimise the T2w effects. This image weighting is useful for assessing the cerebral cortex and is especially useful for identifying tissue with a high fat content. To create a T2w image, in opposition to T1w, the magnetization is allowed to decay before the signal acquisition. This is done by increasing the TE. The TR is also long to allow T1 recovery and hence minimize T1w effects. This image weighting is useful for detecting WM lesions. Ideally both images should be used together, because they provide complementary information. For example in the human healthy adult brain, WM in T1w scans looks brighter than grey matter (GM), in opposition to how they look on T2w; this contrast difference may allow us to identify features in one of the modalities that are not possible to see in the other (Figure 1.2.).

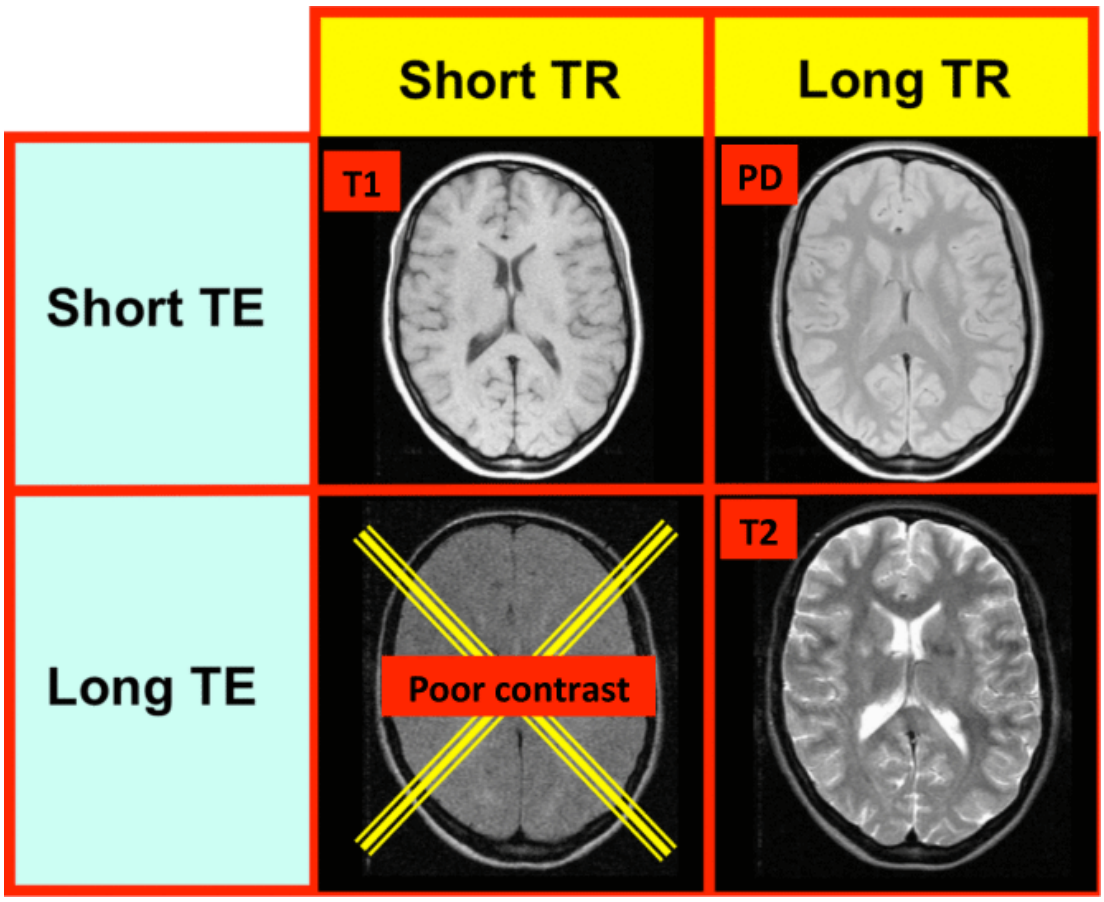

Figure 1.2: Relationship between TR and TE with different image contrasts. From (http://mriquestions.com/image-contrast-trte.html).

Several analyses beyond a simple visual exploration can be applied to the sMRI data to obtain different properties to identify if the subject has some pathologies and to assess myelination. These techniques allow us, for example, to obtain accurate tissue segmentation of the brain (111), anatomical parcellations in the different cortical regions of interest (ROIs) (112) or to create myelin maps of the brain (113), amongst other parameters.

1.3.1. Diffusion MRI

Diffusion MRI is a technique that uses different gradient pulses to stimulate the water molecules and measure their movement in tissue. Due to thermal

excitation, water molecules exhibit Brownian motion (114), but inside different tissues, this motion is restricted due to the membranes of different cellules (Figure 1.3.). Diffusion MRI is the only technique that allows one to measure the water molecule displacement in-vivo.

To create MRI images sensitive to water diffusion, the homogeneity of the applied magnetic field must vary (linearly), which is achieved by using a pulsed field gradient. The protons will begin to precess at different rates, proportional to the magnet strength at each point of the gradient. This results in a dispersion of the phase and a signal loss.

To re-phase the spins of the protons, a new gradient pulse with the same magnitude and opposite direction has to be applied. Since the protons have moved during the interval between pulses due to the Brownian motion, they will not be fully re-phased, hence the signal detected by the MRI equipment will be smaller.

The above described method was initially designed for nuclear magnetic resonance, by Stejskal and Tanner (115). They linked the reduction of the signal to the amount of diffusion through the following equation:

$$\frac{S(TE)}{S_0} = e^{-[\gamma^2 G^2 \delta^2 \left(\Delta - \frac{\delta}{3}\right) D]}$$

Where S_0 is the signal intensity without the diffusion weighting, S is the signal with the gradient, γ is the gyromagnetic ratio, G is the strength of the gradient pulse, δ is the duration of the pulse, Δ is the time between the two pulses, and D is the diffusion-coefficient.

To know where this attenuated signal comes from exactly, another pulse has to be introduced in the mix. This is what is known as a “motion-probing” pulse, and it is applied together with the magnetic gradient pulses that are used in regular MRI to locate the signal. That combination of pulses produces the appearance of cross-terms, which makes the Stejskal-Tanner equation inaccurate. The interactions between pulses must be calculated and integrated in the function, and the equation becomes too complex. Thus, Le Bihan suggested a simplification by representing all the gradient terms as a “b factor” (which depends on the acquisition parameters) (116). The formula for calculating the signal attenuation becomes, then:

$$\frac{S(TE)}{S_0} = e^{-[b*ADC]}$$

The diffusion coefficient *D* is replaced by an apparent diffusion coefficient (ADC) to indicate that the diffusion process is not free in tissues, but hindered and modulated by many mechanisms (restriction in closed spaces, tortuosity around obstacles, etc.)

The WM of the brain is highly organized and restricts the movement of the water molecules, providing a faster diffusion in the direction of the fibres and slower perpendicularly to them (117) (Figure 1.3.).

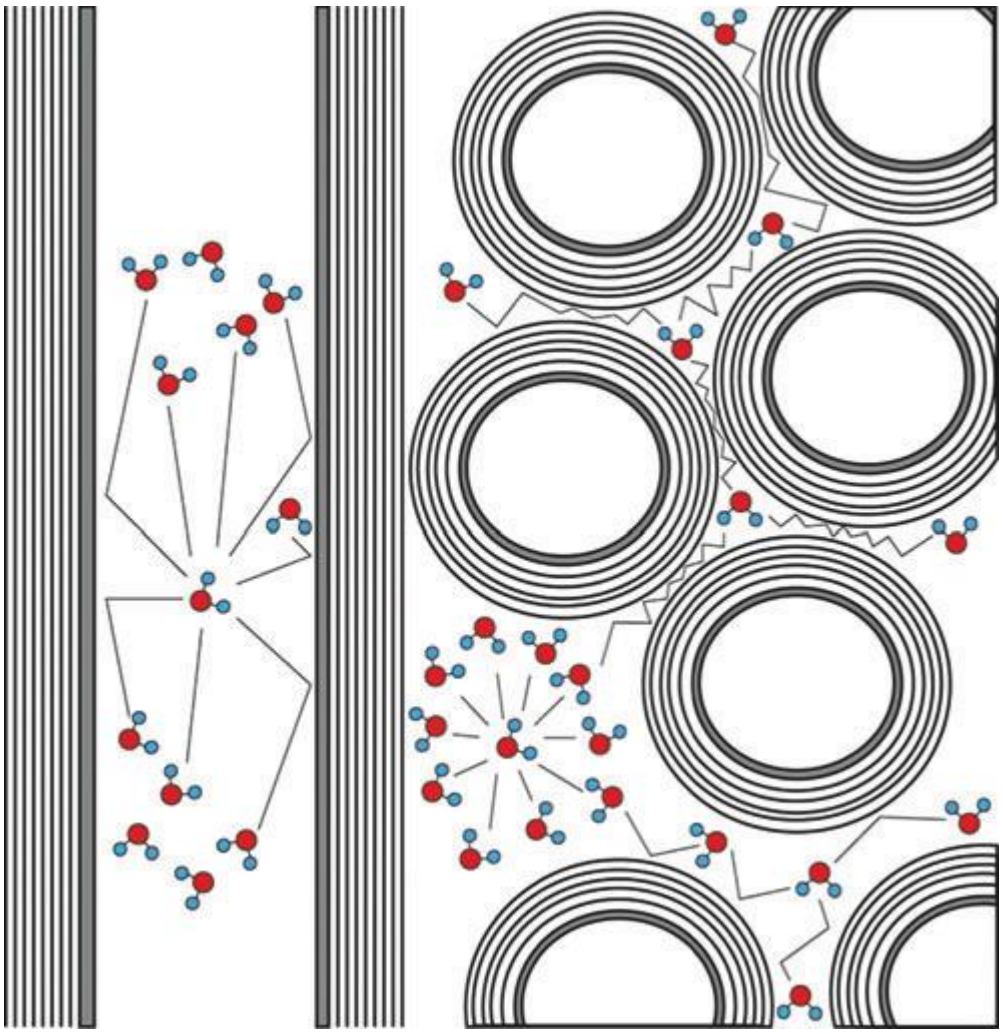

Figure 1.3: Movement of water molecules in constrained environment. A representation of how the water molecules interact with the myelinated axons. It is possible to observe how water diffuses parallel to the axons and is restricted in the perpendicular direction. From "Characterization of Cerebral White Matter Properties Using Quantitative Magnetic Resonance Imaging Stains" by Alexander, A.L. et al. 2011. Brain Connectivity (118).

By applying several gradients, it is possible to detect movement of water molecules in different directions, and how it is restricted by microstructural properties of tissues.

There are several mathematical models which are available to quantify this phenomenon of the directionality of the WM: from the more simple diffusion tensor imaging (DTI) (119) to more complicated models like Q-ball imaging

(Q-Ball) (120), constrained spherical deconvolution (cSD) (121) or diffusion spectrum imaging (DSI) (122).

The DTI model represents each voxel as an ellipsoid (tensor) that quantifies the water movement inside it. From this tensor representation it is possible to obtain different information, from scalar values that allow inference about WM microstructural integrity, such as FA or MD; to more complex representations of the fibre directions of the brain, in, for example, tractography.

From the tensor representation of the DTI model, it is possible to obtain the three eigen values that represent the axes of the tensor ($\lambda_{1,2,3}$) in each voxel, where the first value represents the longer axis of the tensor. The previously mentioned FA and MD are defined using eigen values. FA is a scalar between 0 and 1 that indicates the degree of anisotropy of the diffusion process:

$$FA = \sqrt{\frac{1}{2}} \frac{\sqrt{(\lambda_1 - \lambda_2)^2 + (\lambda_2 - \lambda_3)^2 + (\lambda_3 - \lambda_1)^2}}{\sqrt{\lambda_1^2 + \lambda_2^2 + \lambda_3^2}}$$

MD provides an average of the three axes and represents the diffusivity in the voxel:

$$MD = \frac{\lambda_1 + \lambda_2 + \lambda_3}{3}$$

Both metrics have been widely used in different MRI studies as biomarkers for different diseases (123-125) and especially to study brain development (97, 126-133).

However the DTI model has some disadvantages, the most important one being the impossibility of representation of complex fibre distributions, for instance, FA is naturally low in normal WM areas where fibres cross (134). To overcome this limitation different mathematical models have been suggested based on more complex acquisition sequences. These methods have the ability to detect complex fibre distributions in the brain (those complex distributions are present in around 90% of the brain voxels (135)) (Figure 1.4.).

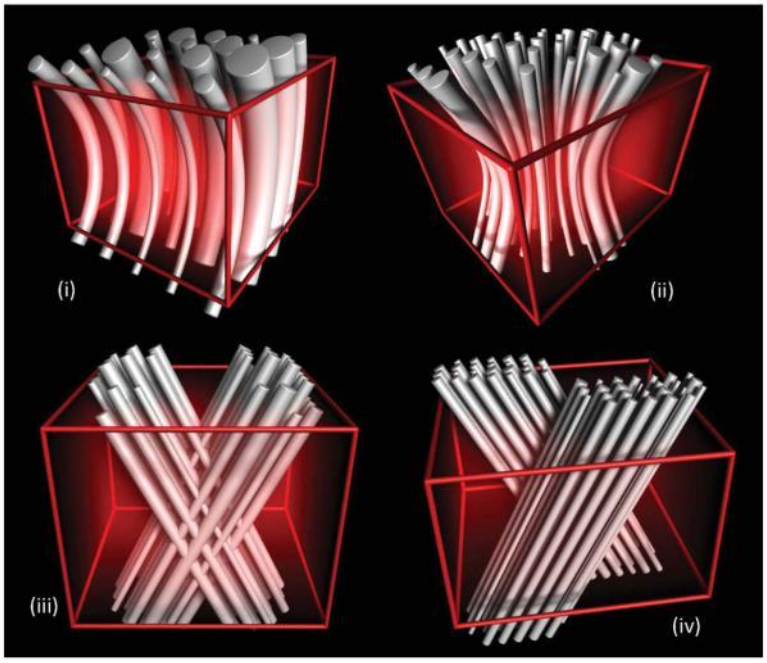

Figure 1.4: Simulated configurations of a complex fibre bundle. The following configurations of "crossing-fibers" are shown: bending (i) and fanning (ii) fibre bundles, interdigitating fibres (iii) and adjacent (iv) fibre bundles. From "Diffusion Tensor Imaging and Beyond" by Tournier, J.D. et al. 2011. Magnetic Resonance in Medicine (136).

Diffusion MRI can be also used to obtain more insightful information on tissue features, such as the axon diameter (137, 138) or the microstructural complexity of dendrites and axons (139). Usually these methods rely on a

model that relates microscopic features of tissue architecture to MRI signals. In general, the approach acquires a set of images with different sensitivities and fits a model to each voxel (140). However, these models require specially acquired data and are outside of the scope of this thesis.

1.3.1.1. Tractography

Tractography is the technique of tracing brain tracts using diffusion MRI data. By using one of the previously mentioned models, in each voxel the direction(s) of the water molecule displacement can be fitted (141, 142). By following these directions it is possible to track different fibre tracts. Tractography has been used in a number of different applications, such as surgical planning (143) or to find differences in WM architecture between groups (144, 145). It has also been employed in several studies of the developing brain to find global differences between term born and preterm born neonates (146, 147), to see the effects of different treatments (29) or different diseases (148, 149), to delineate (in-vivo) different tracts during brain development (150) or to establish patterns of development (151).

Tractography is a powerful tool that is continuously evolving and more advanced frameworks are being created that allow the research and clinical community to create more accurate representations of brain fibres, for example by allowing them to impose anatomical constrains on the tracts (152, 153). However almost all tools were designed and tested for the human adult brain, and so cannot be applied to neonatal data. For instance, one of

the most widely used mechanisms for seeding fibre tracts in the adult brain is to use the grey matter/white matter interface (GMWMI) (152-154); but due to differences in GM/WM tissue contrast in the neonate which limit tissue segmentations, several studies have used use a mask created by thresholding the FA maps as a seeding region. There is a need for the neonatal research community to produce more accurate algorithms in order to be able to apply the more advanced frameworks already in use with the adult brain.

1.3.2. MRI of the developing brain

The brain of a neonate has a higher water content than that of an adult brain, especially in the case of premature babies, and so T1 and T2 values are greater. Thus, to optimize image quality, the imaging sequences need to be adjusted by increasing the TR, TE and inversion time (155).

The usual MRI sequences for clinical assessments in neonates are T1w, T2w, dMRI and inversion recovery, while sometimes susceptibility weighted imaging (SWI) and MR angiography can also be considered (156).

The 1.5-3 T MRI systems available in clinical practices do not allow the differentiation of the most frequent (although subtle) neuropathological patterns such as non-cystic PVL (71, 157). The reason for this is that the conventional qualitative MR used for imaging the whole brain has millimetre resolution, while the processes associated with microcystic necrosis (for

instance, the focal component of non-cystic PVL), as the name suggests are of micron order resolution.

1.4. Image registration

Image datasets can be acquired through using different techniques, at different times or on different objects. To be able to compare them, they have to be combined into one co-ordinate system so that they can be matched according to certain features. This process is known as image registration.

In order to perform a registration, an algorithm executes an unknown geometric transformation for each point of one dataset so that the objects present in an image are aligned with those of a reference image. The goal is to identify the spatial correspondence between datasets that minimizes the differences amongst certain features of the depicted objects.

Image registration can be linear (all pixels of an image rotate uniformly) or nonlinear (deformable). Rigid deformations can be very effective when no anatomic changes are expected, but in many scenarios there are great differences even within the same dataset. Deformable registration can handle local distortion between two images. Usually the linear transformations are used as an initialization for the nonlinear transformation.

The registration algorithm is composed of three main elements: 1) a deformation model, 2) an objective function and 3) an optimization method (158).

1.4.1. Deformation model

Several models have been developed for the nonlinear transformations (for a review see Sotiras et al. (158)), and the choice on which one to use depends on the user and the problem at hand. There is not a unique solution for which model to use. An interesting review of the different models and their performance in registering different human brain imaging datasets was performed by Klein et al. (159). For this work I will mainly use two of the most popular models: Free-Form Deformations (FFDs) (160) and symmetric normalization (SyN) (161).

In the FFDs method a rectangular grid becomes deformed under the influence of the control points. B-splines serve the purpose of interpolating the dense deformation field from a given control point configuration (160). Meanwhile, SyN methodology uses a symmetric parameterization of the shortest path of diffeomorphisms connecting two neuroanatomical configurations. The SyN formulation uses a bidirectional gradient descent optimization which gives results that are unbiased with respect to the input image (161).

1.4.2. Matching criteria

The goal of registration is to maximise the similarity between two images. There are two main types of matching criteria: geometric-based or intensity-based correspondence (162). Geometric methods match the spatial correspondence of different landmarks defined in different anatomical

positions, and intensity-based methods quantify the alignment of images by evaluating an intensity-based criterion over the whole image domain.

The second method has the advantage of better quantification and representation of the accuracy of the estimated dense field at the expense of increasing the computational cost considerably.

1.4.3. Optimisation method

Once the deformation model and the matching criteria are chosen, the aim of optimization is to infer the optimal transformation that best aligns two images according to the selected deformation model and matching criteria. The selection of the different optimisation methods determines the quality of the final result. Different matching criteria usually have several local minima that may lead the registration process to converge. A good optimization method should be able to ignore all the local minima and converge on a global solution that generates an accurate registration (163). Different optimization methods have been reviewed and their performance has been evaluated in rigid and non-rigid registration problems in the literature (164, 165).

1.5. Structural connectivity brain network

One of the most common applications of tractography is to combine it with a sMRI parcellated image to create a structural connectivity brain network. This refers to the existence and structural integrity of tracts connecting different brain areas (i.e. WM tracts connecting cortical areas/nuclei). This approach

has been called “connectomics” (166), and it allows exhaustive mapping of inter-regional structural connectivity within the brain, enabling one to build a graph model of the neural circuits known as a structural brain network or “connectome” (167) (Figure 1.5.). This is a matrix representation of the previously mentioned network where the rows and columns are the nodes and the numbers inside the matrix are a metric inferred from the WM connections between two regions (edges). Physical properties of the fibres such as FA, intra-axonal volume (131, 139) and MD as well as the number of fibres (e.g., percent of all fibres passing from/ending in two regions) can be used as metrics, amongst others.

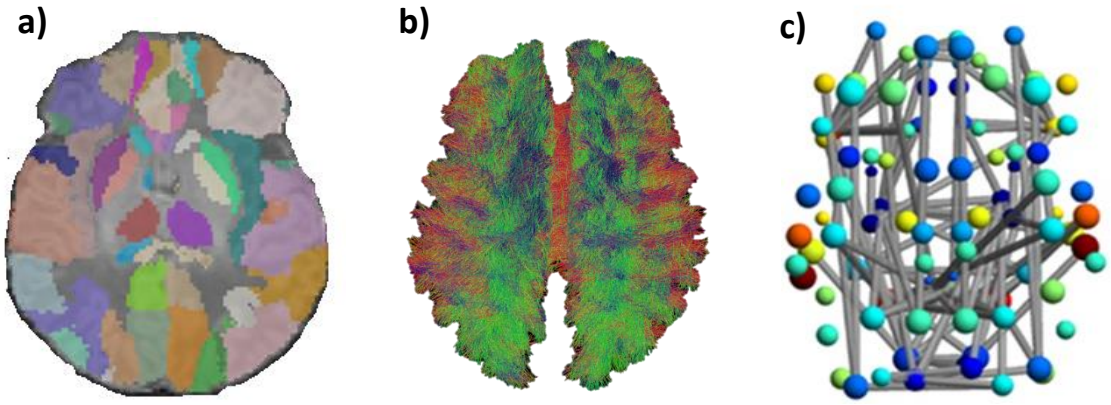

Figure 1.5: Main steps of the structural connectome framework. From left to right: a) parcellation of the brain in different ROIs; b) tractography of the diffusion MR image; c) merging of both information and creation of a network. Adapted from “Imaging connectivity: MRI and the structural networks of the brain.” by Clayden, J.D. et al. 2013. Functional Neurology (168).

These matrices can be analysed in different ways to investigate differences between and within groups. After pre-processing steps such as the removal of anatomically implausible connections (169) or the thresholding of matrices in order to remove spurious or noisy links (for a review of analysing the

structural brain networks see Fornito *et al*. (170)), there are two main methods of comparing different groups:

- Apply graph theory and mathematical modelling to extract complex information about the dynamic of the networks, such as topological measures of the network (e.g. global efficiency) (171).

- Edge-wise comparison and statistical analysis to identify connections associated with a particular effect or contrast of interest, such as a group difference in a case-control comparison or a correlation with clinical measures (172); this allows us, for example to identify different sub-networks related to a pathology.

Connectomics has been used successfully on different human populations to construct structural brain networks in relation to features/diseases: the association of sex with brain size (173), intelligence (174), the effect of schizophrenia on the brain network (124, 175, 176), Alzheimer disease (177, 178) or the evolution of brain networks across lifespan (179). This method has also been successfully applied to non-human populations, for example mice (180) or monkeys (181). Recently a new field has emerged called “comparative connectomics”**,** defined as the comparison of the topological layout of nervous systems across species with the aim of identifying common features in networks of different species (182).

1.5.1. Structural connectivity in the developing brain

More recently, different studies employed structural connectomics to study the neonatal population. Yap et al. characterized normal development of the human brain during the first stages of life, from 2 weeks until 2 years (183); Shi et al. combined these data with morphological networks (184) to study neonates who are at a high risk of schizophrenia, and found that neonates at a genetic risk of schizophrenia had altered structural associations and fibre connections (148). Ratnarajah et al. found hemispheric differences in structural connectivity in neonatal brains (185) and Zhao et al. found regional differences in the maturation of the brain (186). Employing different connectome weights, Pannek et al. found that diffusion metrics produced differences between term and preterm born neonates, but only quantitative T2 relaxation time measures were associated with the degree of prematurity (187).

Brown et al. studied the topology and longitudinal change in the structural connectome of a cohort of normative preterms showing how different network metrics evolve with age (146). The same group also used a machine learning algorithm to predict gestational age (GA) from the connectome of preterm infants (188), and different frameworks (one based on the identification of anatomical subnetworks and another using convolutional neural networks) to predict the Bayley cognitive and motor scores obtained 18 months after birth (189, 190). Keunen et al. related the neonatal connectome to IQ and processing speed at the age of 5, providing evidence that the blueprint of

later cognitive achievement is already present at term-equivalent age and suggest that WM connectivity strength may be a valuable predictor for long-term cognitive functioning (191).

Tymofiyeva et al. applied an automated template-free structural connectivity framework to map the connectome across different ages, and observed increasing brain network integration and decreasing segregation with age in term-born subjects (192). Comparing the neonate and the adult connectome, van den Heuvel et al. found the presence of an early small-world modular architecture of the human neonatal connectome (193); Ball et al. report that the rich club (194) organization is present well before the normal time of birth and may provide the fundamental structural architecture for the subsequent emergence of complex neurological functions (195); and Wee et al. provided novel evidence that the variability of brain anatomical organization at birth predicted internalizing and externalizing behaviours in early childhood, suggesting that foetal brain development plays a crucial role in behavioural development later in life (196).

Finally, Batalle et al. demonstrated the existence of a core of key connections that are not affected by GA at birth. However, they also found that local connectivity involving thalamus, cerebellum, superior frontal lobe, cingulate gyrus and short range cortico-cortical connections was related with GA at birth and contributed to an altered global topology of the structural brain network (131). This is consistent with earlier findings implicating atypical cortothalammic connectivity in relation to age at birth (197-202), that persists

at age 2 years, and may contribute to later impairment, and is part of a wide disconnectivity phenotype.

1.5.2. Limitations of structural connectivity studies in the developing brain

The over-arching framework in creating the structural connectome is constant and independent of the data used to create it, but each step needs to be carefully designed for the data used. For example, anatomical parcellation of the adult human brain is often carried out using Freesurfer (203), but in neonatal age groups the most common strategy used for the parcellation is atlas registration (204). However, this approach has several limitations in neonates, when variation in brain structure over time is large. In recent times, more sophisticated approaches are being developed to parcellate the neonatal brain using more information than is provided by simple atlas registration, for example, by adding information on the age of the neonate using spatio-temporal templates (205) and using the intensity of the image not only to guide the registration, but also to increase the accuracy of the parcellation using the expectation-maximization algorithm (206-209).

Another area of uncertainty in neonatal structural connectivity is optimal tractography construction. Ideally, an accurate tissue segmentation is needed to generate an anatomically plausible seeding region. For instance, following the idea that, for adult data, a mask derived from thresholding the FA data at 0.2 provides a good estimation of the WM, several studies use an FA threshold to generate a seeding area, and this has varied between 0.08 and

0.2 (146, 148, 183, 185, 187-189, 192, 193, 210), (191). This approach of FA thresholding has several limitations in neonates, not least because of low FA values and a large partial volume effect. Furthermore, these thresholds may be too restrictive and remove parts of the WM or allow tracts to cross CSF (Figure 1.6.). Only a few studies used another strategy to restrict the seeding, for example, to seed from different anatomical areas/ROIs (185, 195, 196) or using a tissue segmentation to generate the GMWMI in order to impose anatomical constraints (131).

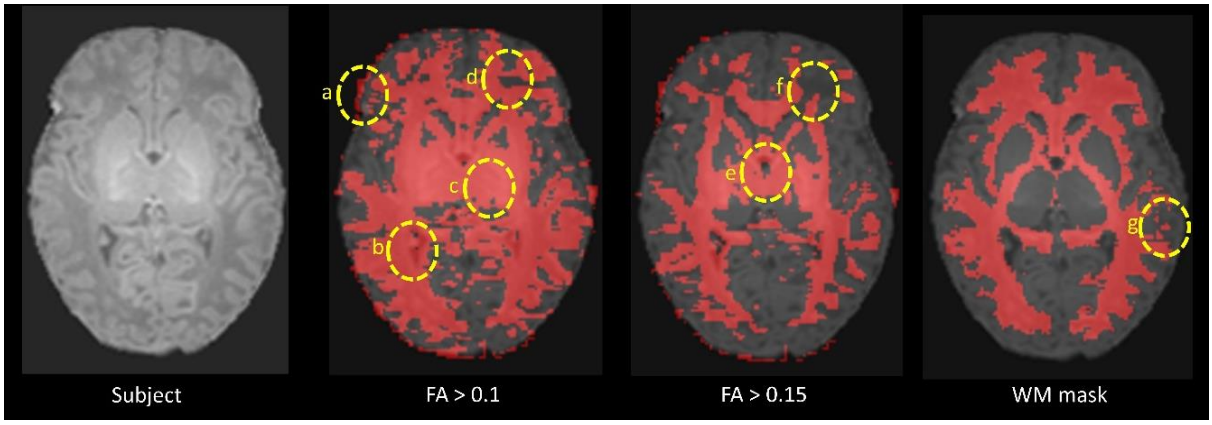

Figure 1.6: Effect of different FA thresholds. Different FA thresholds can allow tracts to cross through the CSF (b and e), include some GM areas (c), go outside of the brain (a), while some WM areas are not selected (d and f). WM seeding is much more accurate, but in some areas tissues are misclassified (g) due to the low contrast between tissues.

Another factor to be taken into account is the tracking algorithm. Due to the low b-values that are often used to acquire the neonatal diffusion MRI data (usually between 750-1000 s/mm^2), the majority of published work has been performed using deterministic tensor based tracking algorithms (146, 148, 183, 185, 186, 188, 189, 191-193, 196, 210). Only a few groups have attempted to solve the crossing fibre problem. Pannek et al. and Ball et al. used a probabilistic algorithm based on the “balls and sticks” fitting of up to

two fibres per voxel (187, 195, 211); Batalle et al. (131) used dMRI data acquired with a b value high enough to resolve crossing fibres using the cSD and iFOD2 algorithms (121, 212); and recently Tosselli et al. used cSD with low b values in neonates to improve the tractography results (213).

2. Hypotheses and methods

This thesis aims to test the following hypotheses:

1. A structural neonatal atlas can be created with the following features to represent ‘normality’, contain 107 labels transformed from adult space, and be interoperable across modalities:
    a. generated exclusively from healthy control subjects;
    b. Anatomic features which are consistent with adult labels to support longitudinal modelling;
    c. Operable across sMRI and dMRI;
    d. Contains symmetric templates which are provided to facilitate studies of cerebral laterality.
2. Creation of a novel optimized framework which combines connectomics with along-tract statistics for automated group-wise comparisons of neonates:
    a. using ACT with age-specific segmentation and atlasing;
    b. using linear fascicle evaluation (LiFE) to optimize the tractography data, and connectivity matrices constructed to test for differences between groups;
    c. and to establish the proof of concept of the framework by replicating a previous observation that dMRI parameters are altered in specific tracts in preterm infants with exposure to antenatal $MgSO_4$ for foetal neuroprotection compared to those without the exposure

3. Exposure to breastmilk in the weeks after preterm birth promotes brain development, evaluated by:
    a. Constructing the connectome using ACT with spherical-deconvolution informed filtering of tractograms (SIFT), and using Network-based statistics (NBS) to perform an edge-wise comparison of the connectomes between groups. The global network measures are also compared between the groups with different breast milk exposures;
    b. Tract-based Spatial Statistics (TBSS) to calculate voxel wise differences in FA, MD, axial and radial diffusivity (AD and RD) across the WM skeleton based on breast milk exposure;
    c. Optimized algorithms for brain extraction and tissue classification to measure the effect of breastmilk exposure on global and local brain tissue volumes.

The first hypothesis with the correspondent sub hypotheses is the third chapter of this thesis and has been already published. The second hypothesis (and sub hypotheses) corresponds to the fourth chapter. Finally, the last hypothesis (and sub hypotheses) is the fifth chapter of the thesis, and is currently, submitted and under review

2.1. Methods

2.1.1. Babies used in the study

98 neonates with GA at birth between 23^{+2} ($weeks^{+days}$) and 41^{+6} weeks were recruited from the Royal Infirmary of Edinburgh between July 2012 and

August 2015. These infants were a sub-cohort of the first wave of the Theirworld Edinburgh Birth Cohort (TEBC, www.tebc.ed.ac.uk) ; the full cohort has been previously reported (29, 201, 214, 215).

The group was divided into those babies with GA at birth <37 weeks (n = 65), and healthy controls recruited from postnatal wards with GA 37^{+2}-41^{+6} weeks (n = 33). Exclusion criteria included major congenital malformations, chromosomal abnormalities, congenital infection, overt parenchymal lesions (cystic periventricular leukomalacia, hemorrhagic parenchymal infarction) or post-hemorrhagic ventricular dilatation. Demographic information is shown in T2.1. Ethical approval was obtained from the National Research Ethics Service (South East Scotland Research Ethics Committee 02) and informed consent was obtained from the person with parental responsibility for each individual participant included in the study.

Table 2.1: Overview of the main characteristics of the employed cohort

	Preterm (*n* = 65)	**Term (*n* = 33)**
Mean GA at birth/weeks (range)	29^{+3} (23^{+2}-34^{+6})	39^{+5} (37^{+2}-41^{+6})
Mean GA at scan/weeks (range)	39^{+7} (38-42^{+5})	42^{+2} (39-47^{+1})
Mean birth weight/kg (range)	1.16 (0.55–1.54)	3.42 (2.35-4.67)

In the following chapters, the population will be described in more detail, taking all the parameters needed for the study design into account.

2.1.2. MRI acquisition protocol

A Siemens MAGNETOM Verio 3T MRI clinical scanner (Siemens Healthcare Erlangen Germany) and 12-channel phased-array head coil were used to acquire the following sequences: T1w MPRAGE (TR = 1650 ms, TE = 2.43

ms, inversion time = 160 ms, flip angle = 9°, voxel size = 1 × 1 × 1 mm^3, and acquisition time = 7 min 49 s); T2w SPACE[1] (TR = 3800 ms, TE = 194 ms, flip angle = 120°, voxel size = 0.9 × 0.9 × 0.9 mm^3, acquisition time = 4 min 32 s); and dMRI using a protocol consisting of 11 T2- and 64 diffusion-weighted (b = 750 s/mm^2) single-shot spin-echo echo planar imaging (EPI) volumes acquired with 2 mm isotropic voxels (TE = 106 ms and TR = 7300 ms). To reduce eddy current induced artefacts and shimming errors to a minimum in the dMRI protocol, an optimized bipolar gradient pulse scheme was employed with a manually selected shim box covering a region extending from the top of the head to several centimetres below the chin.

Infants were scanned without sedation in natural sleep using the feed-and-wrap technique. Physiological stability was monitored using procedures described by Merchant et al. (216). Ear protection was provided for each infant (MiniMuffs, Natus Medical Inc., San Carlos, CA).

Structural images were reported by an experienced paediatric radiologist (A.J.Q. and A.G.W) using the system described by Leuchter et al. (217) and images with evidence of injury (post-haemorrhagic ventricular dilatation, porencephalic cyst or cystic periventricular leukomalacia) or central nervous system malformation were excluded.

[1] SPACE is an acronym for: Sampling Perfection with Application optimized Contrasts using different flip angle Evolution. Is a closely related Fast (Turbo) spin echo technique with special modifications optimizing it for isotropic 3D imaging.

3. Parcellation of the healthy neonatal brain into 107 regions using atlas propagation through intermediate time points in childhood

3.1. Introduction

Labelled atlases provide anatomic information for a range of structural and diffusion MRI (sMRI, dMRI) analysis tasks including structural connectivity mapping and spatio-temporal modelling. In early brain development such approaches have the potential to provide neuroscientific and clinical advances including: provision of quantitative measures of typical brain growth *in vivo*, so defining 'normal' for a newborn population; mapping of atypical trajectories following adverse exposures such as preterm birth; evaluation of tissue effects of neuroprotective treatment strategies that are ready for evaluation in humans; uncovering neural substrates for childhood impairment; and facilitating investigation of the early life origins of adult neurological and psychiatric disease.

The majority of human brain atlases have been developed using adult data [for review see Evans et al. (2012) (218)], and their use for studying the brain during early life may not be valid due to differences in adult and newborn anatomy and image properties (219-223). The latter include marked variation

in head size and shape, maturational processes leading to changes in signal intensity profiles, relatively lower spatial resolution, and lower contrast between tissue classes (224-229). Such differences can lead to misclassification of tissues/structures, so it is essential to match the study group to age-appropriate reference volumes and a number of templates have been developed for this purpose (230-233).

Atlases can be created by manual delineation of a single subject or a small number of subjects. Several investigators have defined protocols to delineate regions of interest (ROIs) in neonatal data. For example, Gilmore and colleagues manually parcellated a single neonatal brain into 16 cortical regions, 20 subcortical regions, brainstem and cerebellum (234); Goussias and colleagues manually parcellated 20 neonatal brains (15 preterm and 5 term-born infants) into 50 regions (the ALBERTs atlas) (235); and Kabdebon et al. (2014) created a 94 region neonatal single-subject template by adapting an adult brain atlas (236) and used it to derive probability maps for the locations of 6 main sulci in cohort of 16 newborn infants (237). In recent work, Alexander and colleagues (238) manually labelled 33 cortical areas per hemisphere corresponding to those in the Desikan-Killiany adult brain atlas (239) in three term neonates. While such atlases describe anatomical detail well (234, 237, 238), they may not capture population diversity adequately (218), are time-consuming to generate and are susceptible to inter- and intra-rater variability.

Some of these issues can be overcome using computational modelling techniques. For example, the University of North Carolina (UNC) atlas was created using image registration and label fusion to propagate an adult brain atlas to 95 neonates through 2 and 1 year old templates (236, 240). Wu and colleagues used large deformation registration to propagate 62 neuroanatomical labels from adults to 15 neonatal brains and performed multi-atlas labelling based on accurate prior-based tissue segmentation (241). Makropoulos and colleagues performed multi-atlas segmentation by label fusion using the ALBERTs atlas (242), and subsequently propagated the segmentations (plus labels of cortical ribbon) to the coordinate space of Serag et al. (205) and averaged these data with an age kernel at each timepoint to create a 4D atlas with 87 labelled structures (243). While these atlases are generally generated from a large cohort and capture population diversity, they are prone to registration error due to shape and tissue contrast differences between adult and neonatal brains.

There are also approaches that combine single subject parcellation with computational methods to create a template. For example, Oishi and colleagues created a template from 20 subjects and propagated a manually labelled single subject (122 regions including WM parcellations) to the template using image registration (244); and subsequently, Zang and colleagues modified the atlas to represent the average anatomic features of the study group by evolving the initial atlas to the representative ‘center’ of the study population, based on the morphological information (245).

In summary, recent advances in standardised delineation of ROIs and computational modelling have led to the development of templates for studies of childhood brain development. However, most existing neonatal atlases contain less anatomical information compared to adult atlases, often include atypical participants which leaves uncertainty about ‘normal’ representation. They also work mainly with one modality and use labelling protocols that do not map readily to established adult atlases, and none facilitate studies of laterality in early life when it may be desirable to distinguish asymmetries in the study population from those of the atlas. These limitations led us to create a new neonatal atlas (ENA33), which has the following features:

1. ENA33 is generated exclusively from healthy control subjects, so represents ‘normal.’
2. The atlas has 107 anatomical regions transformed from an adult atlas, so it is consistent with adult label protocols.
3. ENA33 is operable across different modalities including sMRI and dMRI.
4. Symmetric templates are provided to facilitate studies of cerebral laterality.

3.2. Materials and methods

3.2.1. Overview

The atlas construction framework consists of two main steps. First, each subject is parcellated into anatomical ROIs using temporal registration (246) of an adult atlas (247) via intermediate spatio-temporal templates of the National Institutes of Health Pediatric Database (NIHPD) (248, 249). Second, a groupwise atlas is constructed from the parcellated cohort of healthy neonates using Symmetric Group Normalization (SyGN) (250).

3.2.2. Participants

For the atlas construction, 33 healthy infants born at term (>37 weeks' GA) with mean GA at birth 39^{+5} weeks (range 37^{+2}-41^{+6}) and with mean birthweight of 3.42 kg (2.35-4.67) were used. Subjects underwent MRI at mean 42^{+2} weeks (range 39-47^{+1}). Results from a subset of the group have been reported previously (29).

3.2.3. Image registration

For each registration between two different volumes, a linear transformation was first computed and used as an initialisation to compute a non-linear transformation. In other words, a transformation $T(\mathbf{x})$ for a point $\mathbf{x}$ in 3D space with coordinates x, y and z is computed as follows (160):

$$T(\mathbf{x}) = T_{global}(\mathbf{x}) + T_{local}(\mathbf{x})$$

where T_{global} represents the linear transformation and T_{local} represents the non-linear transformation. The computed transformation maps all the points of a 'Target' volume to a 'Source' volume ($T_{Target,Source}$). Note that the addition of the transformations is different from the composition, the addition represents that the output from one transformation (in this case the affinely registered image) is the input to the following transformation, meanwhile the composition of transformations works by combining all the transformations together in a single transformation, and then, applying it to the moving image.

The interpolation used for all intensity images was B-spline because of its efficacy (251); and Nearest Neighbor interpolation was used for label maps so as not to introduce new classes.

3.2.4. Pre-processing

For dMRI, FA and MD volumes were calculated using the Camino Diffusion MRI Toolkit (http://cmic.cs.ucl.ac.uk/camino) (252). For each subject, the T1w volume was selected as the reference anatomy to which the T2w scan was linearly registered (6 degrees of freedom) using NiftyReg (http://cmictig.cs.ucl.ac.uk/research/software/niftyreg) (253, 254). Then FA and MD volumes were mapped to the same T1w space using the transformation of the first T2w volume of the dMRI dataset (B0) to T1w using

Advanced Normalisation Tools (ANTs, http://stnava.github.io/ANTs) (161) with mutual information as the similarity metric (255). Intra-subject registration of water diffusion maps involved linear plus a non-linear registration with the aim of minimising distortions associated with the single-shot spin-echo echo planar imaging acquisition sequence. We used affine and SyN (161) with a four-level multi-resolution scheme which ran until convergence or a fixed (maximum) number of iterations was reached. We allowed up to 100 iterations at the first level, 100 iterations at the second, 100 iterations at the third and 20 iterations at the full resolution. The rest of the parameters were set to default settings.

A brain mask was computed from the T1w volumes by removing non-brain tissues and skull using the ALFA method (256). The resulting mask was applied to all co-registered modalities, and all volumes were corrected for intensity inhomogeneity using the N4 method (257). Before the process of label propagation and template creation, all the subjects were affine registered to the 42 weeks template of Serag et al. (205).
All the results were checked after this preprocessing stage to ensure that the N4 method and the skull stripping performed correctly.

3.2.5. Tissue segmentation

To create tissue segmentations, T1w volumes were first registered non-linearly to the closest age-matched T1w template from the 4D atlas (258) using Free-Form Deformation (160) implemented in NiftyReg (253, 254) with

default parameters. Then, the expectation-maximisation (EM) algorithm (209, 222) was used to classify each voxel into a tissue class based on voxel intensity information and spatial-based probabilities (259); after this, segmentations were mapped back to the subject's native space. The tissue probability maps were constructed by averaging the tissue segmentations to produce maps of GM, WM and CSF.

3.2.6. Temporal registration via spatio-temporal atlases

To parcellate the neonatal brain, the SRI24/TZO adult brain atlas (247) with 90 ROIs (cortical and sub-cortical structures only) was propagated to the neonatal template using a spatio-temporal atlas from the online database of the NIHPD (248, 249) containing age-dependent templates between birth and 4.5 years old (4.5, 3.5, 2.5, 2, 1.5, 1.25, 1, 0.75, 0.5, 0.25 and 0 year [neonate]) (McConnell Brain Imaging Centre; http://www.bic.mni.mcgill.ca/ServicesAtlases/NIHPD-obj2). The SRI24/TZO atlas is based on the transformed version of the single-subject Automated Anatomical Labeling (AAL) atlas (236) to 24 healthy subjects.

To model the very wide anatomical differences between adult and neonatal brain, we used the LISA method (246) where spatio-temporal atlases are used to aid the registration process between two volumes taken over large time-intervals as it provides prior information about the missing anatomical evolution between the two volumes to be registered. Given a pair of structural images from the adult atlas (I_{SRI24}) and our neonatal cohort (I_{NEO}), we aim to

find a transformation $T_{NEO,SRI24}$ that maps every location in I_{NEO} to I_{SRI24} by estimating a deformation field to register I_{SRI24} to I_{NEO}. To do this, we first mapped each template of the NIHPD to the preceding one: $T_{3.5\to4.5} = NIHPD_{3.5} \to NIHPD_{4.5}$, $T_{2.5\to3.5} = NIHPD_{2.5} \to NIHPD_{3.5}, \ldots, T_{0\to0.25} = NIHPD_{0} \to NIHPD_{0.25}$. After this step, the adult atlas was mapped to the 4.5 year atlas ($T_{4.5\to SRI24} = NIHPD_{4.5} \to SRI24$) and the neonatal NIHPD template to NEO ($T_{0\to NEO} = NEO \to NIHPD_{0}$). All the transformations were then concatenated together:

$$T_{NEO\to SRI24} = T_{NEO\to0} \circ T_{0\to0.25} \circ \ldots \circ T_{4.5\to3.5} \circ T_{4.5\to SRI24}$$

Finally, the combined transformation from the previous step ($T_{NEO\to SRI24}$) was used to derive the registration between the I_{SRI24} and I_{NEO}. The temporal registration process used is summarized in Figure 3.1.

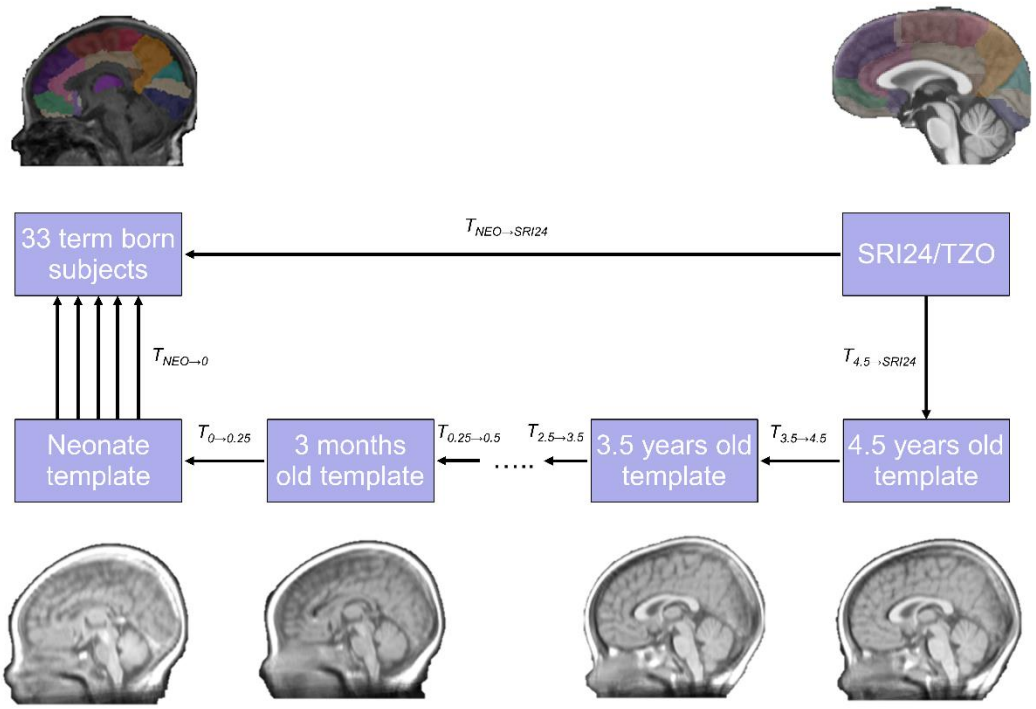

Figure 3.1: The framework used for temporal atlas propagation. The SRI24/TZO adult atlas is propagated to the neonatal template from the NIHPD atlas through intermediate time points, and finally to the cohort under study.

After registration, the transformation allowed locations in the target volume to be mapped to locations in the source volume. All the temporal registrations were performed using affine plus SyN (161) with mutual information as the similarity metric (255), since this is suitable for contrast changes associated with myelination of the brain during development. The last step, $T_{0 \to NEO} = NEO \to NIHPD_0$, was performed using cross correlation (260), because in this case the neonatal T1w template of the NIHPD was registered to subjects where there was no change in the contrast, so registration is intra-modality.

3.2.7. Template and atlas construction

For template creation, we used the Symmetric Group Normalization (SyGN). This method works by coupling the intrinsic symmetry of each pairwise registration and optimizing the shape-based sharpening/averaging of the template appearance. The method has been used in previous studies with successful results (250, 261, 262).

The SyGN method robustly maps populations to a common space by finding the template and set of transformations that gives the “smallest” parameterization of the dataset (250). The metric distance between the average affine transformation and the identity affine transformation as well as the diffeomorphism lengths gives the size of the parametrization. The method may be initialised using an external template or an inital template ($\bar{I}$) that can be derived from the database of *n* images (I_i). In this work, a 42 weeks template (the closest age-matched template to the mean of the cohort under study) from the 4D atlas (205) was used as an initial template.

SyGN optimizes the shape of $\bar{I}$ via a diffeomorphism, ψ (which contains an affine transformation with 12 degrees of freedom), such that the size and shape of the brain converges to the group mean. This is achieved by optimizing the following energy iteratively,

$$E_{\bar{I}} = \sum_i E_{SyN,\prod}\left(\bar{I}, I^i, \phi^i\right) \text{ where } \forall i, \phi^i\,(\mathbf{x}, 0) = \psi(\mathbf{x})$$

here ψ is a diffeomorphism representing the initial conditions of each optimal transformation (ϕ^i) that maps every point **x** in a 3D space of a image (I^i) to a reference image ($\bar{I}$). The solution for each pairwise problem is obtained using SyN (161). The algorithm iteratively minimizes the energy $E_{\bar{I}}$ with respect to the set of ϕ^i through distributed computing (263). In this study, all volumes were previously affine registered to the initial template, so ψ did not contain an affine transformation. The procedure first optimizes the mappings with a fixed template, then, optimizes the template appearance with fixed shape and mappings, and, finally, optimizes the template shape. The process then repeats. The final template is obtained after four iterations.

The final transformations were applied to map the corresponding label maps, tissue segmentation, and T2w, FA and MD volumes to the final template space. To create the final label map majority-voting (264) of all the propagated labels to the template space was used because it is known to perform well in studies of neonates (240).

Studies of brain laterality benefit from a symmetric atlas because of the challenge of distinguishing asymmetries in the study group from those in atlas space, so we created a symmetric version of the atlas. This was created by flipping each subject's T1w volume left to right, and using each volume as an independent subject in the template creation. Basically, the symmetric template contains 66 subjects, the 33 subjects plus the 33

subjects flipped, the transformations are then calculated independently for each one of the 66 images and then, the final transformed images, averaged in the template space, creating the final T1w symmetric template. The main difference between this approach and averaging each subject with the flipped version of itself and then doing the atlas, is that in our approach each transformation is calculated independently for the original image and the flipped image, instead of calculating one transformation for each averaged subject. The final transformations were then applied to the other modalities which were also flipped including the label maps using methods described by Fonov and colleagues (248, 249). To create the final symmetric label map majority-voting (264) was also used. Other symmetric atlases have been created for different purposes, as could be the analysis of development of brain asymmetry in the context of language development (265), but they have to be used carefully, as in fact, these atlases lose the asymmetry contained in the human brain (266).

An additional colour map to the standard coding scheme of the SRI24/TZO was created using brainCOLOR (267) to aid visualisation of lobes. This computes the optimal colour assignments for regions in a 2D or 3D brain image using a brute force strategy to maximize the distinguishability of adjacent regions while simultaneously choosing perceptually similar colours for groups of regions.

3.2.8. Validation

Cross-correlation (CC) between registration of consecutive time points of the spatio-temporal atlas was used to evaluate accuracy of the final registration using methods described for temporal modelling of perinatal MRI data (259).

After temporal propagation, labels were inspected and edited where necessary by a radiologist experienced in neonatal brain MRI (A.G.W.) according to the protocols defined in the *The Human Brain During the Third Trimester* (268) using ITK-SNAP (http://www.itksnap.org) (269). After the template was created, all labels were re-checked according to the same protocol.

The accuracy of registration used for label propagation between the subjects and the registered atlas was tested. To do this, five landmarks were placed in ten randomly selected subjects and the atlas; the atlas was then registered to the subjects using affine and SyN (161) using cross-correlation as the similarity metric. The Euclidean distance between the landmarks of the subjects and those of the registered atlas were measured (270-273). The landmarks were placed at: the most rostral point of right and left superior temporal gyrus viewed in the coronal plane at the level of the third ventricle (referred to as cortical left and right in Table 3.2); the wall of the right and left bodies of the lateral ventricles at the level of the third ventricle in coronal plane (referred to as ventricles left and right in Table 3.2); and the floor of the fourth ventricle in the sagittal plane (referred as cerebellum in Table 3.2). To

investigate potential bias due to intra- and inter-rater variability in landmark placement, landmarks were placed by the same rater twice and by another rater. Raw measurements and intraclass correlation coefficient (ICC) using a two way mixed effects model are reported.

To evaluate agreement of volumetric measurements obtained from ENA33 with those of a comparable atlas,(the UNC atlas, which is derived from the same adult atlas), we compared lobar volumes using the protocol described by Tzourio-Mazoyer et al. (236): *Central Region, Frontal Lobe, Temporal Lobe, Parietal Lobe, Occipital Lobe, Limbic Lobe, Insula and Sub Cortical Gray Nuclei* plus the *Corpus Callosum, Lateral Ventricles*, the *Brainsteam* and the *Cerebellum*. The proportion of intra-cranial volume of each region was calculated. Both label maps were multiplied by the respective mask, then the lobular volume was divided by the brain volume (mask volume).

To investigate differences between the asymmetric and symmetric versions an Asymmetry coefficient (*S*) was calculated. The coefficinet (*S*) is defined as:

$$S = \frac{2*|V_L - V_R|}{V_L + V_R}$$

where V_L is the volume of the left ROI and V_R is the volume of right ROI. The main difference with the index defined in previous studies (274, 275) is that, originally, the index is defined to perform voxel-wise studies, and here it is

adapted to a volumetric analysis. If template construction and label fusion were completely error free across the volume then *S* would have a value of 0 for all regions in the symmetric version.

3.2.9. Volumetric Analysis

We non-linearly registered the final atlas to all subjects using ANTs (161) with the same parameters as above, with the aim of calculating the volume and different dMRI metrics of all ROIs for both hemispheres of the brain. The volumes and dMRI metrics for each region were calculated using FSL (http://fsl.fmrib.ox.ac.uk) (276).

3.3. Results

3.3.1. Neonatal brain parcellation

ENA33 is shown in transverse sections using default colour scheme (generated by ITK-SNAP) in Figure 3.2, and Table 3.1 lists the labels. The 3D volume rendered atlas is shown in Figure. 3.3., using the default and brainCOLOR colour coding generated schemes.

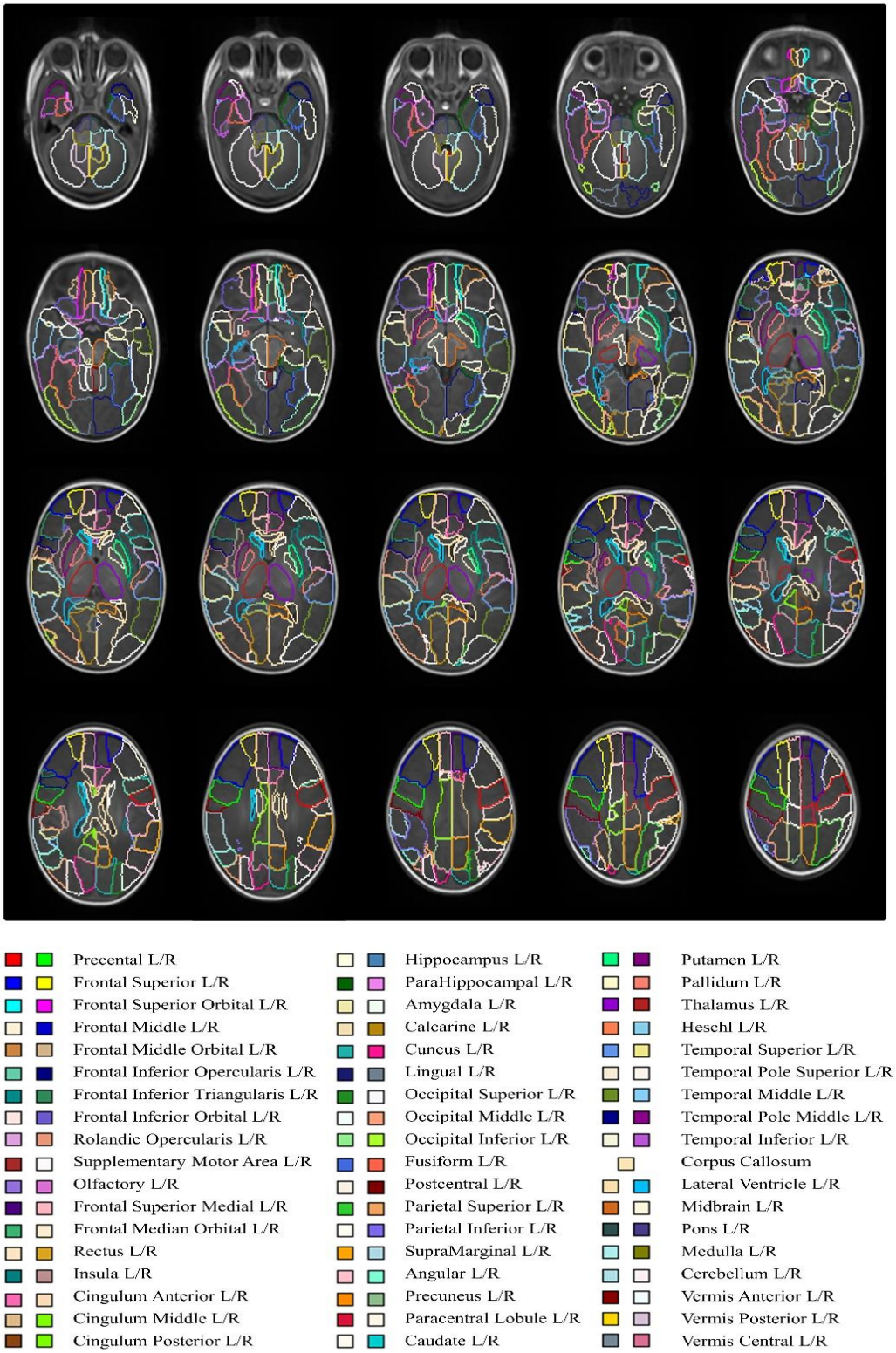

Figure 3.2: Anatomical parcellation of the neonatal brain (axial view). The slices have 3 mm distance.

Table 3.1: Anatomical definition of all the ROIs and the correspondent Label ID

Anatomical Definition	Label ID	Anatomical Definition	Label ID
Precentral Left	1	Fusiform Left	55
Precentral Right	2	Fusiform Right	56
Frontal Superior Left	3	Postcentral Left	57
Frontal Superior Right	4	Postcentral Right	58
Frontal Superior Orbital Left	5	Parietal Superior Left	59
Frontal Superior Orbital Right	6	Parietal Superior Right	60
Frontal Middle Left	7	Parietal Inferior Left	61
Frontal Middle Right	8	Parietal Inferior Right	62
Frontal Middle Orbital Left	9	SupraMarginal Left	63
Frontal Middle Orbital Right	10	SupraMarginal Right	64
Frontal Inferior Opercularis Left	11	Angular Left	65
Frontal Inferior Opercularis Right	12	Angular Right	66
Frontal Inferior Triangularis Left	13	Precuneus Left	67
Frontal Inferior Triangularis Right	14	Precuneus Right	68
Frontal Inferior Orbital Left	15	Paracentral Lobule Left	69
Frontal Inferior Orbital Right	16	Paracentral Lobule Right	70
Rolandic Opercularis Left	17	Caudate Left	71
Rolandic Opercularis Right	18	Caudate Right	72
Supplementary Motor Area Left	19	Putamen Left	73
Supplementary Motor Area Right	20	Putamen Right	74
Olfactory Left	21	Pallidum Left	75
Olfactory Right	22	Pallidum Right	76
Frontal Superior Medial Left	23	Thalamus Left	77
Frontal Superior Medial Right	24	Thalamus Right	78
Frontal Median Orbital Left	25	Heschl Left	79
Frontal Median Orbital Right	26	Heschl Right	80
Rectus Left	27	Temporal Superior Left	81
Rectus Right	28	Temporal Superior Right	82
Insula Left	29	Temporal Pole Superior Left	83
Insula Right	30	Temporal Pole Superior Right	84
Cingulum Anterior Left	31	Temporal Middle Left	85
Cingulum Anterior Right	32	Temporal Middle Right	86
Cingulum Middle Left	33	Temporal Pole Middle Left	87
Cingulum Middle Right	34	Temporal Pole Middle Right	88
Cingulum Posterior Left	35	Temporal Inferior Left	89
Cingulum Posterior Right	36	Temporal Inferior Right	90
Hippocampus Left	37	Corpus Callosum	91
Hippocampus Right	38	Lateral Ventricle Left	92
ParaHippocampal Left	39	Lateral Ventricle Right	93
ParaHippocampal Right	40	Midbrain Left	94
Amygdala Left	41	Midbrain Right	95
Amygdala Right	42	Pons Left	96
Calcarine Left	43	Pons Right	97
Calcarine Right	44	Medulla Left	98
Cuneus Left	45	Medulla Right	99

Cuneus Right	46	Cerebellum Left	100
Lingual Left	47	Cerebellum Right	101
Lingual Right	48	Vermis Anterior Left	102
Occipital Superior Left	49	Vermis Anterior Right	103
Occipital Superior Right	50	Vermis Posterior Left	104
Occipital Middle Left	51	Vermis Posterior Right	105
Occipital Middle Right	52	Vermis Central Left	106
Occipital Inferior Left	53	Vermis Central Right	107
Occipital Inferior Right	54		

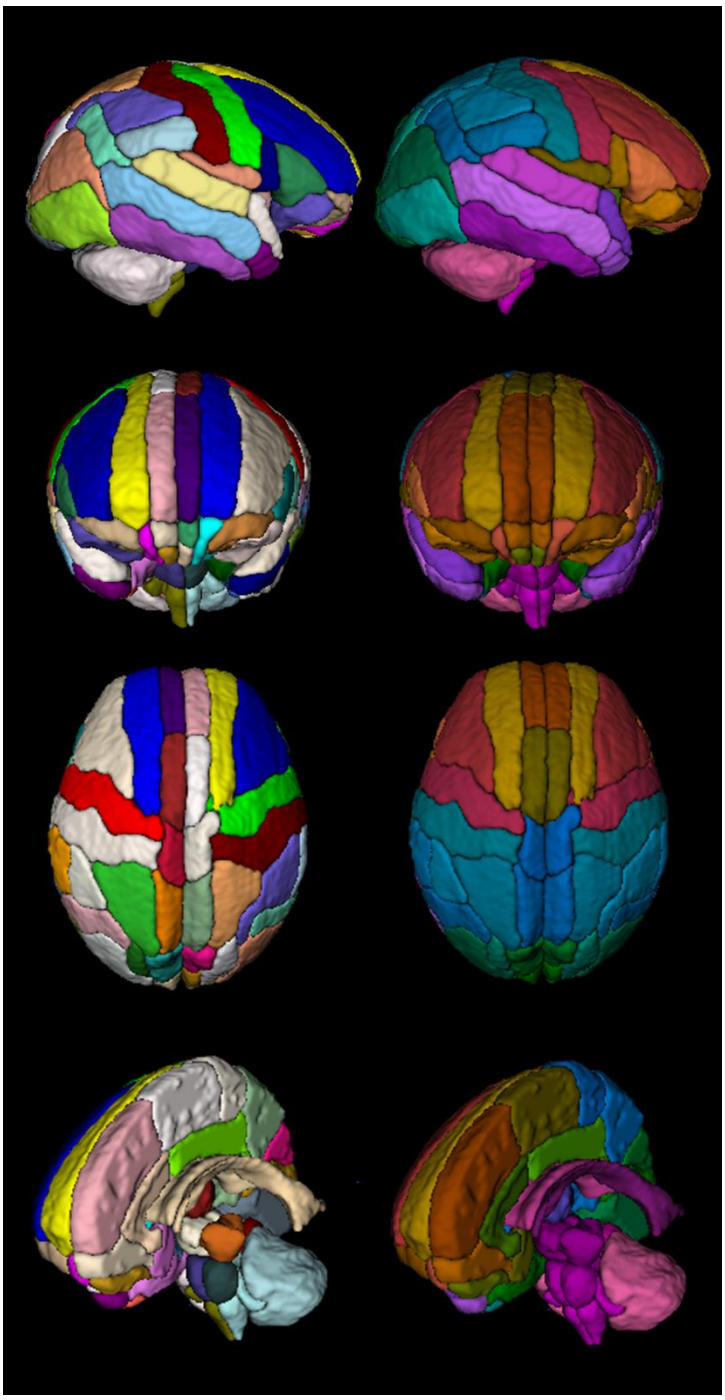

Figure 3.3: 3D rendered of the atlas. Comparing both color codes: standard color code (left column) versus created color code (right column).

An intial step from adult to 4.5 years was used because we found that no additional benefit was conferred by the inclusion of three time points at 15.5, 10.5 and 6.5 years: the normalised cross correlation between registered

images generated using both approaches was ≈0.98.

3.3.2. Application of the atlas to multi-modal data

Figure 3.4 shows the templates for available modalities. Nine participants had T2w volumes that were free of motion artefact and suitable for registration, so the T2w template shown is constructed from this subset.

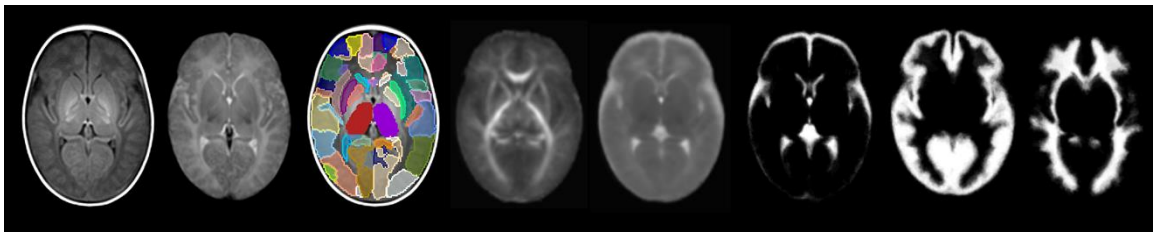

Figure 3.4: Different template modalities: *From l*eft to right: T1w template, T2w template, label parcellation map overlaid on T1w template, FA template and MD template. and tissue probability maps for CSF, GM and WM

Figure 3.5 shows the symmetric version of the atlas compared with the asymmetric version, and Figure 3.6 shows the differences in S for each ROI. S was <0.05 for all regions in the symmetric version, and values ranged from 0.01-0.9 in the asymmetric version.

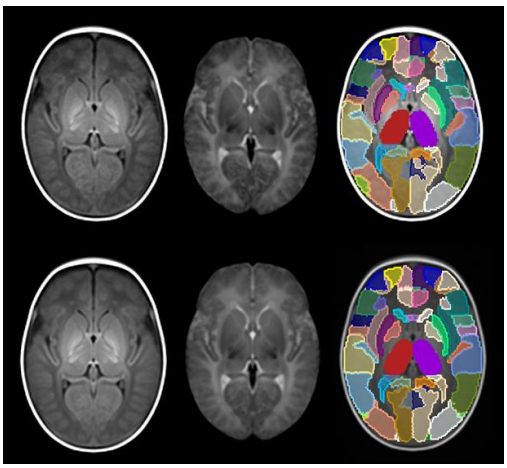

Figure 3.5: Upper row: asymmetric version of the atlas; Lower row: symmetric version of the atlas. From left to right: T1w template, T2w template, and label parcellation map overlaid on T1w template

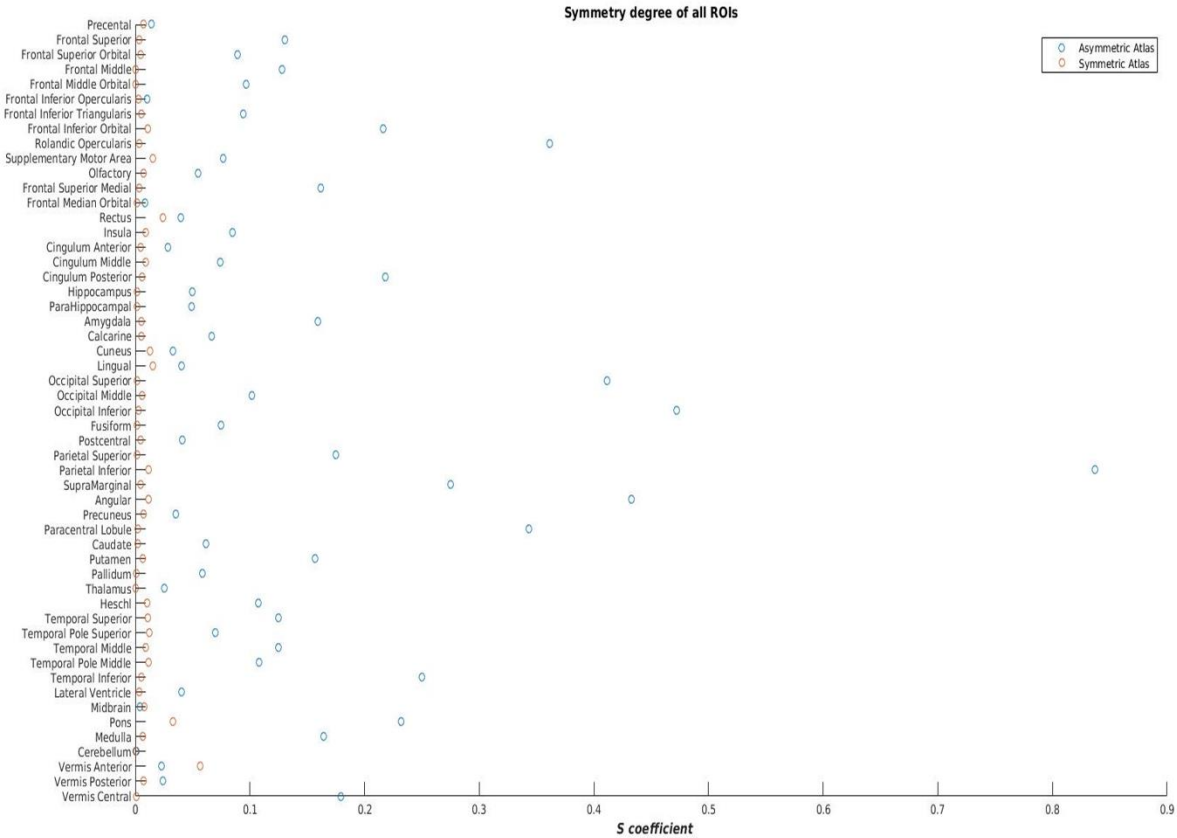

Figure 3.6: Asymmetry coefficient in the asymmetric atlas and the symmetric versions of ENA33.

3.3.3. Validation

Cross correlation between the intermediate time points was high (0.93±0.05). The smallest values were 0.81 and 0.87 for the last two steps (3 month to 1 months and 6 months to 3 months), which is a period of dynamic change in signal intensity associated with myelination. The rest of the values were above 0.94.

Assessment of parcellations by an expert (A.G.W.) according to a reference atlas [(*The Human Brain During the Third Trimester* (268)] led to minor edits in thalamus, pallidum, and putamen bilaterally. The following labels were added manually: *posterior fossa* (with its corresponding sub-areas), *lateral ventricles* and *corpus callosum*. After the template was created, the labels were checked again, and minor corrections were made at the brain–CSF boundary only.

The Euclidean distance between landmarks in native space and those of the registered atlas were in an acceptable range for both raters (Table 3.2), and the ICC was >0.95 for intra- and inter- rater variation.

Table 3.2: Landmark registration accuracy (Euclidean distance between ENA33 and individuals)

	Distance (mm)		
	Rater 1	Rater 1 second time	Rater 2
Landmark	**Mean (SD)**	**Mean (SD)**	**Mean (SD)**
Cortical Left	1.29 (0.82)	1.17 (0.79)	1.66 (0.81)
Cortical Right	1.58 (0.91)	1.58 (0.86)	1.89 (1.21)
Cerebellum	1.15 (0.59)	1.02 (0.59)	1.16 (0.61)
Lateral Ventricle Left	1.89 (0.49)	1.86 (0.59)	2.33 (0.60)
Lateral Ventricle Right	1.77 (0.63)	1.85 (0.92)	2.08 (0.85)

There was broad agreement between the lobar volumes calculated as a proportion of intracranial volume from ENA 33 and the UNC atlas, shown in Table 3.3.

Table 3.3: Volumes of interest calculated from ENA33 and UNC atlases

	ENA 33 Atlas	UNC Atlas
Region	**Proportion of intracranial volume (%)**	**Proportion of intracranial volume (%)**
Central Region	7.57	7.46
Frontal Lobe	34.41	36.3
Temporal Lobe	8.80	11.19
Parietal Lobe	8.53	11.6
Occipital Lobe	13.23	14.55
Limbic Lobe	5.9	8.57
Insula	1.46	1.74
Sub Cortical Gray Nuclei	3.53	3.75
Corpus Callosum	1.06	--
Lateral Ventricles	0.55	--
Brainsteam	1.98	--
Cerebellum	5.58	--

3.3.4. Analysis of normative data from 33 healthy newborns

Labels were propagated to the images of the 33 healthy infants to provide

reference sMRI data for each ROI. Table 3.4 shows the mean volumes for all ROIs.

Table 3.4: Volumes for all brain regions.

	Right Hemisphere	Left Hemisphere
Region	**Mean (SD) / cm^3**	**Mean (SD) / cm^3**
Precental	8.87 (1.19)	9 (1.17)
Frontal Superior	9.96 (1.54)	8.59 (1.26)
Frontal Superior Orbital	1.51 (0.22)	1.4 (0.22)
Frontal Middle	11.6 (1.74)	13.27 (1.61)
Frontal Middle Orbital	2.36 (0.37)	2.56 (0.41)
Frontal Inferior Opercularis	2.77 (0.36)	2.71 (0.44)
Frontal Inferior Triangularis	2.89 (0.56)	3.03 (0.57)
Frontal Inferior Orbital	5.32 (0.78)	4.23 (0.66)
Rolandic Opercularis	5.37 (0.74)	3.67 (0.54)
Supplementary Motor Area	5.81 (0.74)	5.33 (0.77)
Olfactory	1.25 (0.16)	1.31 (0.2)
Frontal Superior Medial	5.96 (1.04)	6.84 (1.12)
Frontal Median Orbital	1.47 (0.28)	1.47 (0.3)
Rectus	1.17 (0.2)	1.13 (0.17)
Insula	3.67 (0.28)	3.46 (0.28)
Cingulum Anterior	2.47 (0.27)	2.38 (0.32)
Cingulum Middle	3.53 (0.4)	3.85 (0.42)
Cingulum Posterior	0.35 (0.07)	0.44 (0.08)
Hippocampus	2.08 (0.18)	2.2 (0.18)
ParaHippocampal	2.58 (0.22)	2.41 (0.23)
Amygdala	0.65 (0.06)	0.76 (0.06)
Calcarine	4.26 (0.55)	3.8 (0.57)
Cuneus	3.72 (0.51)	3.55 (0.47)
Lingual	7.35 (0.69)	7.83 (0.89)
Occipital Superior	2.24 (0.34)	3.45 (0.38)
Occipital Middle	5.7 (0.74)	6.43 (0.71)
Occipital Inferior	3.34 (0.43)	5.52 (0.53)
Fusiform	5.73 (0.74)	5.06 (0.54)
Postcentral	6.82 (0.98)	7.08 (0.91)
Parietal Superior	5.72 (0.73)	4.65 (0.57)
Parietal Inferior	2.42 (0.33)	5.75 (0.8)
SupraMarginal	3.81 (0.54)	2.98 (0.51)
Angular	3.47 (0.55)	2.25 (0.42)
Precuneus	7.17 (0.69)	7.14 (1.03)
Paracentral Lobule	2.17 (0.29)	3.2 (0.45)
Caudate	1.03 (0.12)	1.1 (0.14)
Putamen	1.29 (0.13)	1.57 (0.17)
Pallidum	1.56 (0.24)	1.7 (0.24)
Thalamus	3.81 (0.24)	3.89 (0.28)

Heschl	1.04 (0.24)	0.94 (0.17)
Temporal Superior	6.47 (0.69)	7.24 (0.69)
Temporal Pole Superior	2.65 (0.34)	2.91 (0.35)
Temporal Middle	7.46 (0.82)	8.61 (1.02)
Temporal Pole Middle	1.53 (0.29)	1.35 (0.23)
Temporal Inferior	8.24 (0.86)	6.38 (0.78)
Lateral Ventricle	2.58 (0.6)	2.75 (0.77)
Midbrain	1.88 (0.11)	1.86 (0.1)
Pons	0.83 (0.1)	1.03 (0.12)
Medulla	2.24 (0.2)	2.57 (0.2)
Cerebellum	11.24 (1.28)	11.17 (1.33)
Vermis Anterior	0.8 (0.16)	0.82 (0.18)
Vermis Posterior	2.03 (0.4)	1.97 (0.36)
Vermis Central	0.69 (0.09)	0.85 (0.13)
Corpus Callosum	2.63 (0.36)	

3.4. Discussion

Using MRI data from 33 healthy newborn infants, we created a neonatal brain atlas that parcellates the brain into 107 anatomical regions that can be applied to T1w, T2w, dMRI (FA and MD) and tissue probability maps; it also contains a symmetric version of all templates. The framework for atlas creation was based on temporal propagation of a labelled adult brain atlas (SRI24/TZO) via a sequence of MRI templates from childhood to early infancy which may make it suitable for modelling human brain growth using a consistent set of labels over time. The basis for considering that one-to-one mapping of adult to neonatal structures would be feasible stems from the consistent observation that human cortical gyrification is established during the third trimester of pregnancy, so such that the ‘adult’ configuration is present in the healthy infant born at full term, and this can be discerned using MRI (277-280).

The SRI24/TZO atlas was used because it represents brain anatomy in an unbiased population-averaged coordinate system, and at the same time, provides a large number of structures in crisp definition so is suitable for label propagation (247). An initial temporal registration step from adult to 4.5 years was used because we found that no additional benefit was conferred by the inclusion of three time points at 15.5, 10.5 and 6.5 years.

There is inverted contrast of WM and GM signal between neonatal and adult brain volumes which might suggest that the ideal registration between adult and neonatal templates should be performed between neonatal T1w and adult T2w volumes. However, the use of intermediate templates avoids marked step-wise changes in contrast and it was possible to achieve accurate temporal registration using T1w volumes with mutual information as the similarity metric (246). The diffeomorphic registration algorithm described by (161) was used because of its accuracy as demonstrated in a recent comparison of non-rigid registration techniques (159), but other algorithms may also be suitable for this framework, including Free-Form Deformation (160), Large Deformation Diffeomorphic Metric Mapping (LDDMM) (281), or FNIRT (276) among others. For multi-modality template construction, the SyGN framework was used, because of its ability to produce population-specific templates. The main advantage of the method is that it iteratively optimizes the template appearance and template shape (261).

The validation strategy we used was both qualitative and quantitative. The

requirement for manual editing by an expert according to protocols defined in the *The Human Brain During the Third Trimester* (268) was limited to a small number of ROIs. We tested accuracy of temporal registration using cross-correlation and results demonstrated high accuracy of the registration approach (mean CC of 0.93). To confirm accuracy of label propagation we used a landmark approach, and found Euclidean distances in an acceptable range for landmarks selected to represent the cortex, ventricular system and cerebellum. Both intra- and inter- rater variability were low, and the magnitude of difference is likely to be acceptable for most applications.

The volumes reported in this cohort of normal infants are of similar magnitude and variance to those reported in other smaller studies of healthy newborns, albeit at the level of tissue class or larger regions interest, rather than corresponding ROIs (69, 282, 283). We found very similar measurements of lobar volumes as a proportion of ICV between ENA33 and the UNC atlas, which uses a similar label protocol to ENA33. The small differences between the two atlases could be due to the propagation approach (in this work more time points were used, and an extra registration step is implemented), to differences in template construction method and/or to the manual corrections, or they could reflect normal population variation. Further studies that include large numbers of participants with sharing of data and protocols from multiple centres will be required to determine the extent to which small differences in measured values represent population diversity versus methodological variation.

It should be noted that partial volume effects are not significant for measures derived from the structural volumes with voxel size of ~1 mm^3 because the template is resampled from 0.86 to 1 mm^3 (284-286). For acquisitions with larger voxel sizes (for example dMRI with 2 mm^3) it is possible that partial volume effects could confound the extracted metrics.

A beneficial feature of ENA33 is provision of a symmetric version with labels, which is novel for a neonatal populations and could have utility for future study designs involving neonatal data that require identification of asymmetry in the study group. The asymmetry coefficient (*S*) was <0.05 for all structures in the symmetric atlas but ranged from 0.01-0.9 in the asymmetric atlas which reflects the wide regional variation and the magnitude of asymmetry in the healthy newborn brain. The asymmetric coefficient is not exactly 0 because the 42 weeks template used for the initialization of the template creation process contains a degree of asymmetry that is propagated through the process.

The atlas could be used for different voxel-wise studies or multi-modal applications that are substantially improved by the use of a specific neonatal template, including voxel-based techniques such as TBSS (123, 127), Statistical Parametric Mapping (SPM) (284), structural connectivity and network analyses or volumetric studies. This atlas can be used to perform studies of laterality when it is important to distinguish template asymmetries

from those of the study population.

3.5. Conclusion

In this work, we present a new framework for atlasing the brain in early life. The resulting atlas (ENA33) contains 107 regions with high spatial definition which can be applied to give anatomical context to T1w, T2w volumes, and FA and MD data, whilst also providing tissue probability maps. The method of generating the labels of ENA33 makes the atlas consistent with some adult atlases, a fact that is very useful in future studies. A symmetric version of the atlas is also generated for studies of laterality in the developing brain. The atlas is available to the research community by contacting the Brain Images of Normal Subjects (BRAINS) repository (http://www.brainsimagebank.ac.uk) (287).

4. Combining connectomics with along-tract statistics to study brain development in preterm infants

4.1. Introduction

As we stated in the introduction, diffusion magnetic resonance imaging is a powerful technique for investigating connectivity of neural systems using tract-specific and connectomic approaches. The field has evolved rapidly in recent years with the development of ‘higher-order’ methods which: enable estimation of orientations and relative contributions of fibre populations within each voxel; combine anatomical information with dMRI to create biologically plausible tractography data and estimates of connectivity (152); combine tractography information with tissue microstructural models (288, 289); and enable calculation of along-tract water diffusion parameters (290).

Premature birth is a leading cause of neurocognitive/psychiatric impairment across the life course and is closely associated with altered connectivity of neural systems including thalamic, cortico-spinal, callosal and cerebellar networks (29, 197). It is likely that these changes form part of a more generalized ‘disconnectivity’ phenotype (146, 187, 193), which may have important clinical implications because network ‘disconnection’ predicts reduced information transfer efficiency - a foundational competence for cognition in later life (291).

Interest in MRI based group-wise analyses of neonates is motivated by the need to understand: genetic and environmental risk and resilience factors for perinatal brain injuries (29); the role of imaging biomarkers in evaluating neuroprotective treatments; and in studies of prognosis and early risk stratification (29, 199). Anblagan et al. (29) reported that preterm infants exposed to antenatal magnesium sulfate ($MgSO_4$), which is offered to women in threatened preterm labour at less than 30 weeks of gestation as it is associated with reduced rates of cerebral palsy among offspring (27), had slightly lower tract-averaged MD in the splenium of the corpus callosum compared with unexposed preterm infants.

It is challenging to apply advanced tractography frameworks, which have largely been developed and / or tested in adults to the neonatal brain due to fundamental differences between adult and neonatal structural and dMRI data (219). Early studies of the developing brain structural connectome used whole-brain tractography approaches in which FA was used to create seeding regions and deterministic tensor propagation algorithms to generate tracts (146, 193). Recent innovations in developing brain connectomics include: probabilistic tracking using a two-compartment partial volume model of water molecule diffusion and fitting up to two fibres per voxel (187, 195) or incorporation of anatomical information by ROI-to-ROI and remove tracts entering into the CSF (195). Most recently, Batalle et al. (131) applied ACT (152) with SIFT (289) to reduce the number of false positives.

In the tract analysis field, Berman et al. (292) performed tract-specific measurements of water diffusion parameters by placing ROIs in different

slices; Partridge et al. (293) used a similar approach to asses WM maturation in the premature brain; Dubois et al. (294) centred all bundles to a common origin to establish anatomical correspondence (295); and to demonstrate a direct quantitative relationship between the microstructural maturation of the optic radiations and the functional development of visual perception during early infancy. Geng et al. (151) explored ten fibre tracts, including commissural, association and projection tracts, with tract-based analysis and investigated how they evolve during the first 2 years of life. This was achieved by creating a diffusion tensor MRI atlas and generating tractography data in that space after the fibres were back-mapped to each subject. This resulted in consistent atlas tract geometry across subjects while replacing the diffusion information with values mapped from each subject (145).

Yeatman et al. created the Automated Fiber Quantification method which enables calculation of MRI parameter profiles along a tract of interest, and showed that children (9-16 years) born preterm have altered tract profiles, which correlate with behaviour (296). Finally, Pecheva et al. (297) used tract-specific analysis (298) to study the effects of age at scanning and prematurity at birth on major WM tracts in a large cohort of infants. They described the effects of age at scan on water diffusion tensor metrics in nine tracts, showing that tract-specific analysis is indeed sensitive to the developmental changes.

Here, we extend the methodology of these studies by combining connectomics with along-tract statistics to create a fully automated

framework for group-wise comparisons of neonates. To do this we used the ACT framework (152) adapted to neonates with age-specific segmentation and atlasing tools (256, 299). Next, LiFE was applied to optimize the tractography data (288), and connectivity matrices constructed to test for differences between groups. Finally, regions that showed significant differences in a comparison of infants with and without antenatal $MgSO_4$ exposure were used to seed tracts from one to the other, and along-tract statistics were used to compare FA and MD values along the length of the tract (290).

4.2. Materials and Methods

4.2.1. Overview

The optimized framework for neonatal connectome construction is shown in Figure 4.1. The following pipeline was used: denoising (300) and upsampling diffusion data, MRtrix (301) (http://www.mrtrix.org/); skull stripping of structural data using ALFA (256) (http://brainsquare.org/); mask propagation from the structural data to the diffusion data, NiftyReg (253) (http://cmictig.cs.ucl.ac.uk/wiki/index.php/NiftyReg/); eddy current correction, FSL (276) (https://fsl.fmrib.ox.ac.uk/fsl/fslwiki/FSL/) of the diffusion data; bias field correction, N4 (257) (http://stnava.github.io/ANTs/) of both modalities; EPI distortion and alignment, ANTs (161) (http://stnava.github.io/ANTs/); parcellation and segmentation, the previously created atlas and SEGMA (299); constrained spherical deconvolution (302) and ACT (152), MRtrix; optimizing tractography, LiFE (288) (https://github.com/francopestilli/life/);

and connectome construction, MRtrix and the Brain Connectivity Toolbox (171) (https://sites.google.com/site/bctnet/).

Once the connectome data were created, along-tract statistics were used to investigate the nature of connectome differences between preterm infants exposed to antenatal $MgSO_4$ versus those who were not (290) (https://github.com/johncolby/along-tract-stats/wiki/) (Table A1).

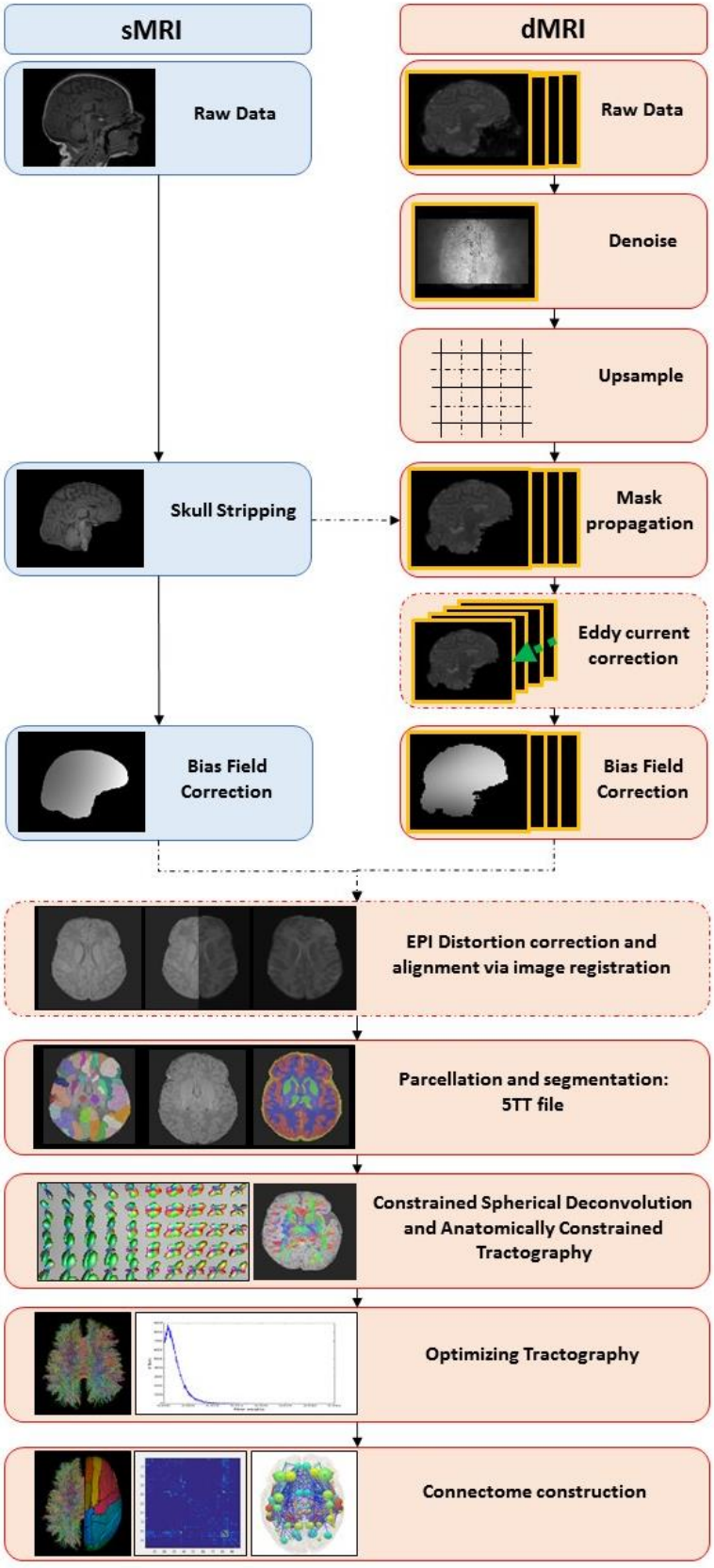

Figure 4.1: Overview of the neonatal brain connectome framework.

Currently, there is not a unique way to derive the structural connectome. Multiple approaches exist depending on the study and research group. Some of the steps involved are still quite novel to be performed in neonatal structural connectivity, for example the denoising, the up-sampling or the bias field correction of the diffusion data. Other steps such as skull stripping and registration can be performed using several different software packages. The post-processing of the tractography is also quite uncommon due to the novelty of these approaches/toolboxes. Moreover, this analysis can be performed either in the template space or in the subject native space. All these different methods are valid and is up to the researcher to make the choice of software and different steps involved in the process, taking into account the question of interest and the proficiency in the available software packages.

4.2.2. Participants

65 preterm infants (mean GA at birth 29 weeks and 3 days (29^{+3}), range 23^{+2}–34^{+6} weeks) were employed for this study, underwent brain MRI at term equivalent age (mean GA 39^{+7} weeks, range 38–42^{+5} weeks) (Table 4.1). 49% of the infants were exposed to $MgSO_4$, the rest were not.

Table 4.1: Demographic information for the participants.

	Infants exposed to antenatal $MgSO_4$ (n=32)	**Infants not exposed to antenatal $MgSO_4$ (n=33)**
GA birth/weeks (mean and range)	28^{+4} (26^{+1} –31^{+5})	30^{+1} (23^{+2} –34^{+6})
Birth weight/kg (mean and range)	1.112 (0.815–1.440)	1.199 (0.550–1.540)
GA at image acquisition/weeks (mean and range)	39^{+4} (38–42^{+1})	40^{+2} (38–42^{+5})
Weight at image acquisition (mean and range)	3.003 (2.460–4.870)	2.777 (2.070–3.780)
Postnatal sepsis*	13 (40.3%)	14 (42.4%)
Bronchopulmonary dysplasia**	10 (31.2%)	8 (24.2%)

* Postnatal sepsis was defined by: 1) positive blood culture growing pathogenic bacteria; *or* 2) blood cultures negative or positive for coagulase negative staphylococcus (CoNS) *plus* generalized signs of infection *plus* physician decision to treat with antibiotics for 5 days or more.

**Defined as need for supplemental oxygen and/or respiratory support at 36 weeks' GA

4.2.3. T1-weighted pre-processing

For each T1w volume, the brain mask was generated by removing non-brain tissue and skull using ALFA, a machine-learning based method that was evaluated on neonatal MRI data (256), followed by a bias field correction using N4 (257).

4.2.4. Diffusion MRI pre-processing

The first step was to denoise the dMRI data (300, 303) followed by up-sampling by a factor of 2 to match the resolution of the T1w volumes using cubic b-spline interpolation. Following this step, eddy current correction was performed using FSL. The first non–diffusion-weighted volume (B0) was set

as the target into which the remaining 74 volumes were co-registered (12 degrees of freedom) using tri-linear interpolation. Diffusion-encoding gradient directions were rotated accordingly (304).

The brain mask was then propagated from the T1w volume with free-forms nonrigid registration using default parameters. This was implemented in NiftyReg with normalised mutual information as the similarity metric. Finally, each dMRI dataset was corrected for bias field inhomogeneity by first estimating the inhomogeneity field map from the B0 volume, then applying the field map to correct all other volumes.

4.2.5. EPI distortion correction and alignment of both modalities

To correct the dMRI data for distortions associated with the single-shot spin-echo EPI acquisition sequence, a registration based method was used (305). First, the T1w volume was co-registered (6 degrees of freedom) to the B0 volume. The B0 volume was then registered to the T1w volume using the symmetric image normalization method (SyN) implemented in Advanced Normalisation Tools (ANTs, http://stnava.github.io/ANTs/) with a four-level multi-resolution scheme that ran until convergence or a fixed (maximum) number of iterations was reached. We allowed up to 100 iterations for the first 3 levels and 20 iterations at the full resolution, but restricted the deformation direction to the phase encoding direction only. Finally, the computed transformation was applied to the remaining volumes of the dMRI data. There is no need to reorient the diffusion gradient vectors after the EPI distortion correction since the underlying directionality of diffusion

sensitization is unaffected by the presence of EPI distortions (306). The transformation was also applied to the brain mask. All registrations of the EPI distortion corrected data used mutual information as a similarity metric (307). Maps of FA and MD were then calculated for each subject using FSL DTIFIT (276).

4.2.6. Anatomical parcellation and tissue segmentation

The T1w template of the atlas created in the third chapter was used to parcellate the T1w volume of each participant using rigid, affine and SyN registration with cross correlation as the registration metric.

The previously created atlas has 107 ROIs, but for the structural connectivity we do not include the WM or CSF ROIs, as we are only focused on the GM parcellation. Because of this, the ROIs corresponding to the corpus callosum, lateral ventricles, pons, brainstem and medulla oblongata were removed resulting in parcellation of 98 ROIs (Table 4.2).

The ACT framework requires a 'five-tissue type' (5TT) file composed of five tissue probability maps: cortical GM, deep grey matter (dGM), WM, CSF, while the last type is reserved for pathological tissues (n.b. this is an empty file in the current study). The main requirement of the 5TT file is that the sum of the intensities across all volumes for one voxel should be one. In the original implementation (152) the 5TT file is generated based on methods for adult segmentations, but these are unsuitable for neonatal data. To generate the 5TT segmentation, we used SEGMA (299) which is an automatic SEGMentation Approach for human brain MRI, using sliding window and

random forests, that provides accurate segmentations across the life course (including neonatal period). In summary, a number of manually labelled images (k=10) 'uniformly' distributed in the low-dimensional data space were used as training data (256) (the segmentation of the training data is documented in the following section); tissue classification was performed using a machine learning based label fusion technique. With the training data correctly segmented, we proceeded to segment all T1W volumes to create the 5TT file and the GMWMI NIfTI volumes for each subject. All tissue segmentations were visually inspected and manual editing was not required (Figure 4.2).

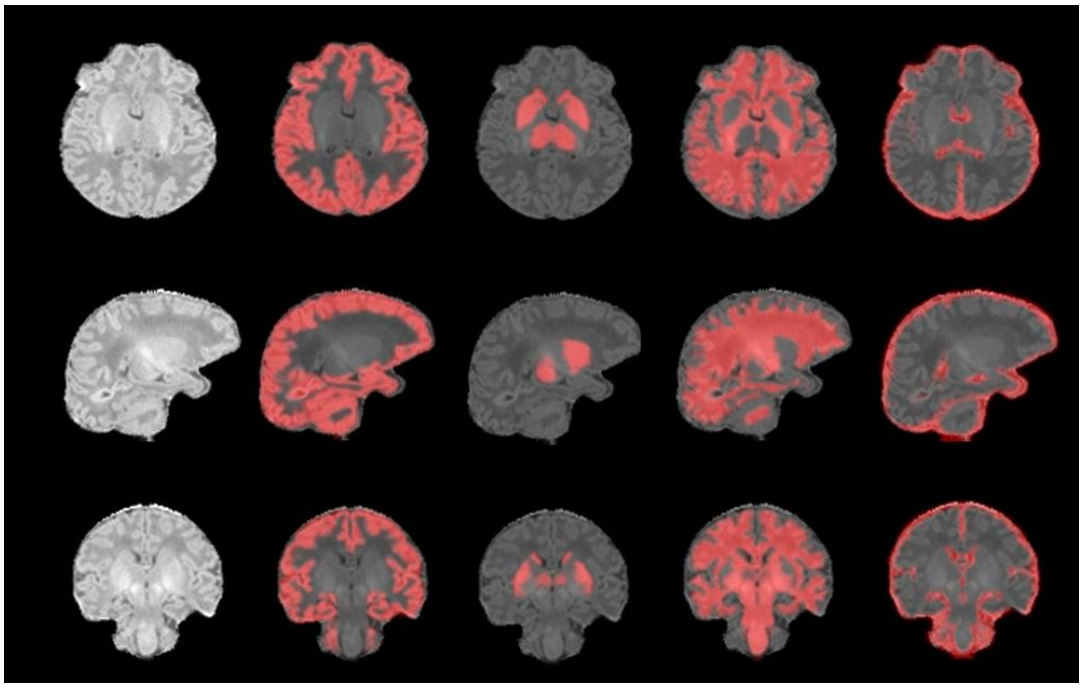

Figure 4.2: Tissue segmentation for ACT. The first row shows the axial view of the T1w volume of a single subject and from left to right overlaid on this T1w volume, the tissue probability maps obtained from the segmentation: GM, dGM, WM and CSF. The second row shows the same but for the sagittal view and the third for the coronal view.

Table 4.2: Anatomical definition of the ROIs of the connectome

Anatomical Definition	Label ID	Anatomical Definition	Label ID
Precentral Left	1	Occipital Superior Right	50
Precentral Right	2	Occipital Middle Left	51
Frontal Superior Left	3	Occipital Middle Right	52
Frontal Superior Right	4	Occipital Inferior Left	53
Frontal Superior Orbital Left	5	Occipital Inferior Right	54
Frontal Superior Orbital Right	6	Fusiform Left	55
Frontal Middle Left	7	Fusiform Right	56
Frontal Middle Right	8	Postcentral Left	57
Frontal Middle Orbital Left	9	Postcentral Right	58
Frontal Middle Orbital Right	10	Parietal Superior Left	59
Frontal Inferior Opercularis Left	11	Parietal Superior Right	60
Frontal Inferior Opercularis Right	12	Parietal Inferior Left	61
Frontal Inferior Triangularis Left	13	Parietal Inferior Right	62
Frontal Inferior Triangularis Right	14	SupraMarginal Left	63
Frontal Inferior Orbital Left	15	SupraMarginal Right	64
Frontal Inferior Orbital Right	16	Angular Left	65
Rolandic Opercularis Left	17	Angular Right	66
Rolandic Opercularis Right	18	Precuneus Left	67
Supplementary Motor Area Left	19	Precuneus Right	68
Supplementary Motor Area Right	20	Paracentral Lobule Left	69
Olfactory Left	21	Paracentral Lobule Right	70
Olfactory Right	22	Caudate Left	71
Frontal Superior Medial Left	23	Caudate Right	72
Frontal Superior Medial Right	24	Putamen Left	73
Frontal Median Orbital Left	25	Putamen Right	74
Frontal Median Orbital Right	26	Pallidum Left	75
Rectus Left	27	Pallidum Right	76
Rectus Right	28	Thalamus Left	77
Insula Left	29	Thalamus Right	78
Insula Right	30	Heschl Left	79
Cingulum Anterior Left	31	Heschl Right	80
Cingulum Anterior Right	32	Temporal Superior Left	81
Cingulum Middle Left	33	Temporal Superior Right	82
Cingulum Middle Right	34	Temporal Pole Superior Left	83
Cingulum Posterior Left	35	Temporal Pole Superior Right	84
Cingulum Posterior Right	36	Temporal Middle Left	85
Hippocampus Left	37	Temporal Middle Right	86
Hippocampus Right	38	Temporal Pole Middle Left	87
ParaHippocampal Left	39	Temporal Pole Middle Right	88
ParaHippocampal Right	40	Temporal Inferior Left	89
Amygdala Left	41	Temporal Inferior Right	90
Amygdala Right	42	Cerebellum Left	91
Calcarine Left	43	Cerebellum Right	92
Calcarine Right	44	Vermis Anterior Left	93
Cuneus Left	45	Vermis Anterior Right	94
Cuneus Right	46	Vermis Posterior Left	95

Lingual Left	47	Vermis Posterior Right	96
Lingual Right	48	Vermis Central Left	97
Occipital Superior Left	49	Vermis Central Right	98

4.2.6.1. Tissue segmentation of the training data

The tissue segmentation for the training data was generated in a semi-automated way as follows:

Cortical grey matter. The image was segmented into 10 or more different tissue classes using Atropos (308) with *KMeans* (the number of tissues vary depending of the subject) and those that best represent the cortex were chosen. The GM of the cerebellum was included in this tissue class.

Deep grey matter. The sub-cortical structures were obtained via image registration of the neonatal atlas created in the third chapter. The following regions were merged to create the dGM tissue class: *Thalamus*, *Caudate*, *Putamen* and *Pallidium.*

Cerebrospinal fluid. This signal class was obtained using the expectation-maximization (EM) algorithm (222). T1w volumes were first registered non-linearly to the closest age-matched T1w template from the 4D atlas (205). Then, the EM algorithm was used to classify each voxel into a tissue class based on voxel intensity information and spatial-based probabilities (258, 259); after this step segmentations were mapped back into the subject's native space.

White Matter. To create the WM mask, the sum of the segmentations listed above was subtracted from the brain mask (256).

The tissues were then merged to one file and the resulting segmentation assessed for anatomical correctness.

4.2.7. Anatomically-constrained tractography

Finally, the sMRI and dMRI data were preprocessed and aligned. Fibre orientation distributions (FOD) were estimated by constrained spherical deconvolution (cSD) at each voxel using a harmonic order (l_{max}) of 8 (302, 309). The remaining ACT parameters were: algorithm iFOD2 (212) with seeding at the GMWMI; initial FOD amplitude threshold 0.15 and final amplitude 0.1; step size 1 mm; 4 samples per step; maximum curvature per step 45°; backtracking and cropping the tracts at the GMWMI. 100,000 tracts were generated with a minimum length of 20 mm and maximum length of 200 mm, which is consistent with previous studies that have used LiFE for tractography optimisation (288, 310, 311). The final result can be seen in Figure 4.3.

4.2.8. Optimizing connectome: Linear Fascicle Evaluation (LiFE)

First, all of the tracts not ending in any ROI of the whole brain parcellation were removed. Next LiFE was applied to improve the quality of connectomes. The method solves a set of simultaneous linear equations to estimate a weight for each WM fascicle, which is used to measure the contribution of each tract to the final predicted diffusion signal. Only those tracts that make a positive contribution to the diffusion MRI data were retained (288). This

removes redundant tracts and false positives (312), which can lead to unwanted effects on network measures if retained (288, 289, 313).

To visualize the effect of LiFE on the tractography data, the tract-density imaging (TDI) (314) results from one subject is shown before and after the application of LiFE in Figure 4.5.

4.2.9. Connectome construction and analysis

The connectome was constructed by assigning to an edge a weight based on the raw number of tracts between regions: $w(e_{i,j}) = c_{i,j}$. where $e_{i,j}$ represents the connection between the nodes i and j; $w(e_{i,j})$ is the weight of the connection $e_{i,j}$; and $c_{i,j}$ is the number of tracts between i and j. After, connections with less than five tracts were set to 0, resulting in a network with a size of 98 × 98 (131, 315) (see Table 4.2 for a list of the ROIs).

Any implausible tracts traversing from one cortical hemisphere to any contralateral subcortical node were discarded (169). All connectivity matrices were normalised between 0 and 1.

The connectomes were separated in two groups: preterms exposed to antenatal $MgSO_4$ versus unexposed preterms. The mean and the standard deviation were calculated for each connection of each group, and values outside the range of mean ± 3 standard deviations were removed. Finally, a *t*-test was applied to each connection and type one error was controlled using false discovery rate (FDR) (316).

4.2.10. Along-tract statistics

If a connection showed significant differences between the two groups in the previous step we selected the ROIs involved in the altered connection, and generated 100 tracts from one ROI to the other. After this we applied LiFE to each bundle of tracts generated. Finally, we extracted along-tract information (FA and MD); by doing so the path that connects two ROIs is investigated, focusing only on the connection that shows differences in tract-counting matrices.

In order to define the spatial location of differences we used methods described by Colby et al. (290). In summary the ROI was used to seed the tractography, and tracts were included if they terminated in the corresponding ROI identified from the connectome analysis (290). For a given tract, tracts were reoriented to a common origin, then re-parameterized with cubic B-splines and resampled, so that each had the same number of points spread evenly along its length. The underlying voxel volume was resampled at the new vertices, and these values were collapsed across tracts at each analogous group of vertices to obtain mean scalar estimates along the tract. Once the different scalars were calculated along the tract, statistical comparison was performed between both groups using ANOVA implemented in R, with adjustment for factors that are known to influence dMRI parameters in WM and / or are associated with WM injury: bronchopulmonary dysplasia, sepsis, GA at birth and GA at scan.

4.3. Results

4.3.1. Tractography reconstruction

Figure 4.3 shows zoomed views of cortical and deep GMWMI respectively. Streamline terminations are shown as coloured dots. With ACT (Figures 4.3c and 4.3d) tracts terminating within WM are rejected and terminations only occur at the GMWMI and within the subcortical structures. In considering the performance of ACT at the deep GM/WM boundaries, Figure 4.3c shows that no tracts terminate within CSF, corpus callosum or internal capsule.

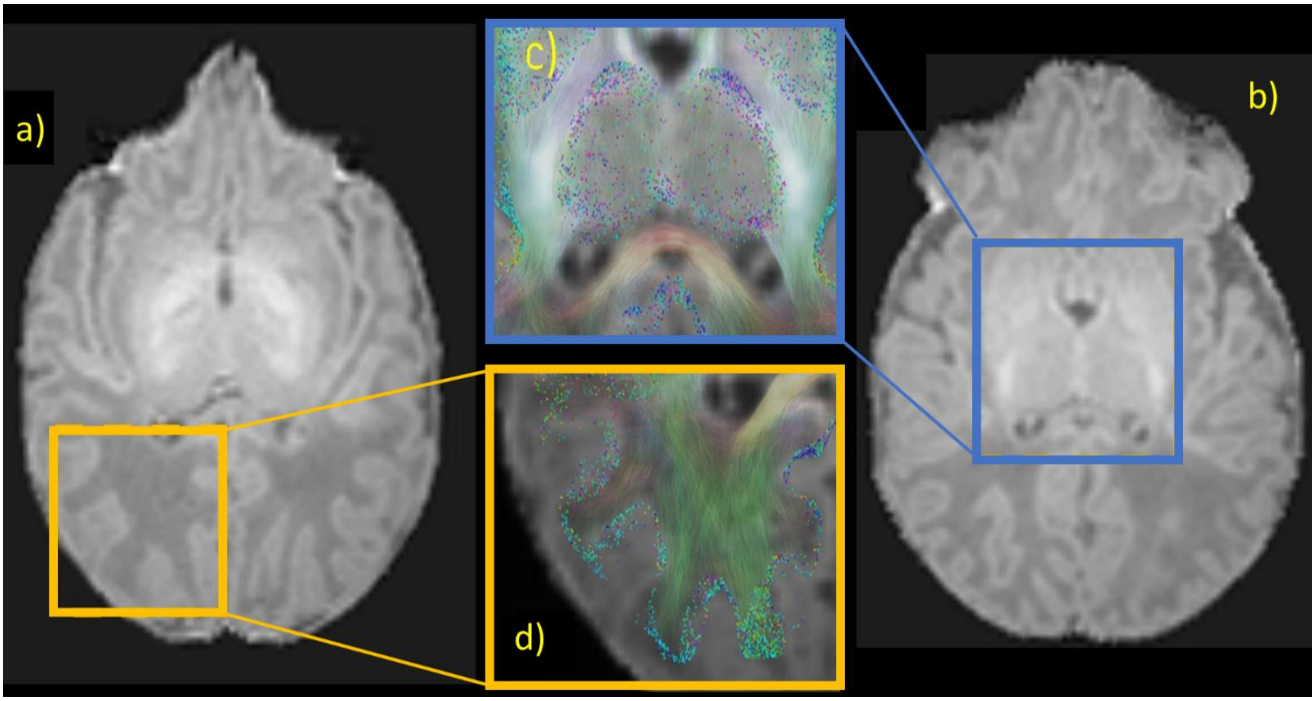

Figure 4.3: Tractography reconstruction with ACT. a) zoomed region of interest at the cortical GMWMI, b) zoomed region of interest at the sub-cortical GMWMI, and panels show termination of tracts in the subcortical regions (c) or in the cortical GMWMI (d). Streamline colours indicate tangent orientation (red: left-right; green: anterior-posterior; blue: inferior-superior).

We assessed the effect of ACT in comparison with FA thresholding as a seeding strategy (FA ≥ 0.15 to seed regions and FA ≤ 0.1 to end tracts). The rest of parameters were set according the original paper of Smith et al. (152). The result can be shown in Figure 4.4, where we used TDI (314) to overlay the results of the tractography and the tract termination over the T1w volume of the subject represented in Figure 4.3. The FA seeding strategy produces terminations inside the WM (figures 4.4c and 4.4g) and also there are several parts of WM that are not covered by the tracts due to the low FA in the neonatal brain (figures 4.4b and 4.4f).

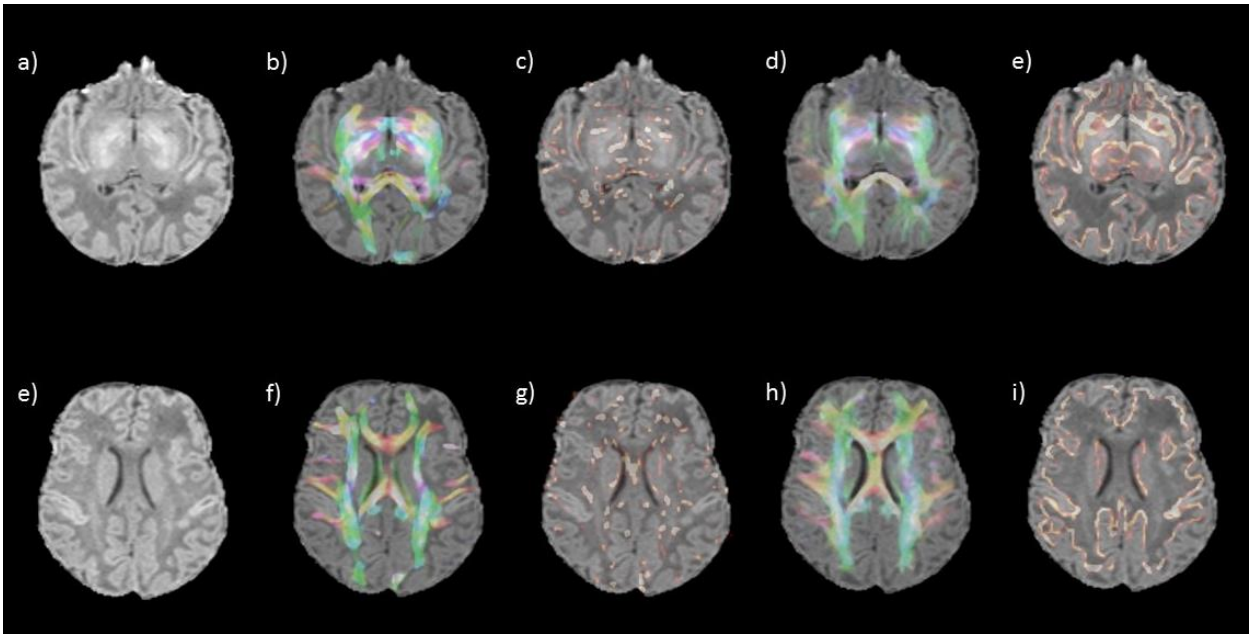

Figure 4.4: Comparison of seeding strategies. a) and e) different slices of the T1w volume of a single subject; b) and f) the TDI created using FA as a seeding strategy; c) and g) the map of the tract termination points created using FA as a seeding strategy; d) and h) the TDI created using ACT with GMWMI as a seeding strategy; e) and i) the map of the tract termination points created using ACT with GMWMI as a seeding strategy.

LiFE removed approximately half of the tracts in each subject (Figure 4.5). The intensity of the TDI map is determined by the number of fibres per voxel (a brighter image means more fibres). Figure 4.5a displays the TDI of a subject before the application of LiFE and shows full coverage of the WM but with inhomogeneous distribution of tracts; this is corrected in Figure 4.5b (the same subject, but after the application of LiFE) which shows the same coverage of WM, but with fewer and more uniformly distributed fibres.

Finally, Figure 4.5c displays the number of fibres before and after the application of LiFE and shows that this method removes half of the tracts. The proportion of tracts removed by LiFE did not vary as a function of GA at birth, or exposure to $MgSO_4$.

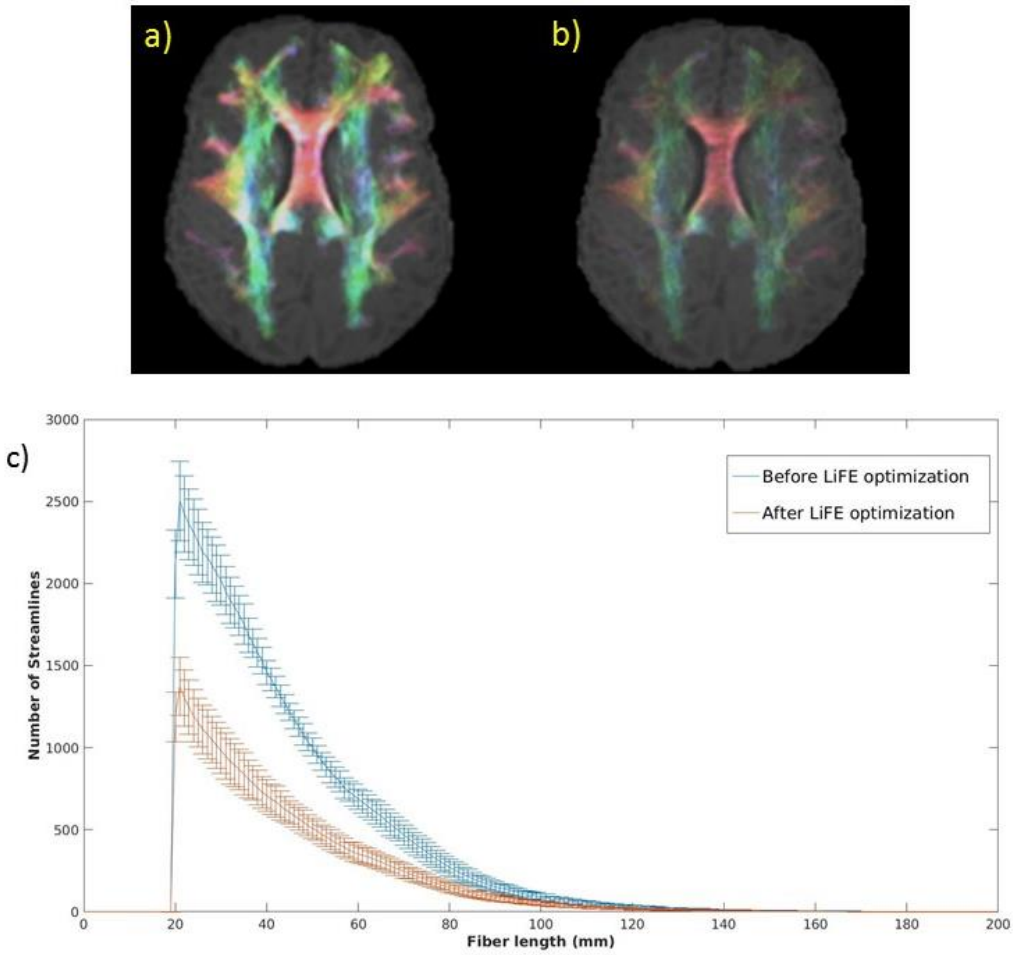

Figure 4.5: The effect of LiFE optimisation. a) and b) TDI of a single subject before and after the application of LiFE; and c) number of tracts depending of the length before and after optimization.

4.3.2. Structural connectivity analysis

The splenium of the corpus callosum, connecting occipital middle left and right regions was the only retained connection that differed between $MgSO_4$ exposed and non-exposed groups, after adjustment for GA at scan, GA at birth, proven sepsis and bronchopulmonary dysplasia; FDR corrected (Figure 4.6).

The difference in the number of streamlines could be due to several factors. The splenium is an area where the fibers are well oriented, and generally well myelinated. Is it difficult to make an assumption of the reason behind this effect. For example a difference in the FA could be due to several factors such as axonal density or different amount of extracellular space. More advanced and complementary images are needed to make further interpretations.

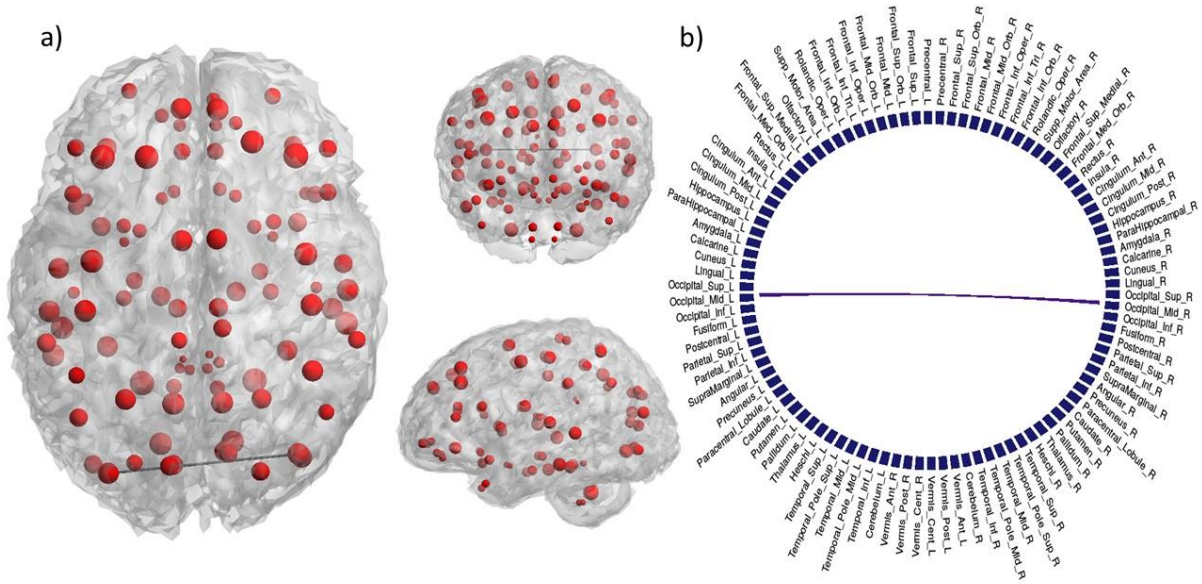

Figure 4.6: Effect of antenatal $MgSO_4$ exposure on the connectome at term equivalent age. Connectome and chord diagram a) Axial, coronal and sagittal view of the brain surface and nodes with the connection that shows differences between groups ($p < 0.05$ corrected), generated with BrainNet (317) (https://www.nitrc.org/projects/bnv/); and b) Chord diagram of the differences between groups ($p < 0.05$ corrected), generated with Circlize (318) (https://cran.r-project.org/web/packages/circlize/index.html).

4.3.3. Along-tract statistics

Having identified a group difference in structural connectivity in the splenium (increased number of streamlines in the $MgSO_4$ exposed group), tracts that connected one ROI (occipital middle left) with the other ROI (occipital middle right) were calculated, and FA and MD along the path was plotted for each group (Figure 4.7). There were significant differences between groups in the FA and the MD (the inferior black line in each graph shows where the differences were located), and the squared area shows the tract location where there were differences in both metrics. There was no group difference in tract averaged mean for either metric.

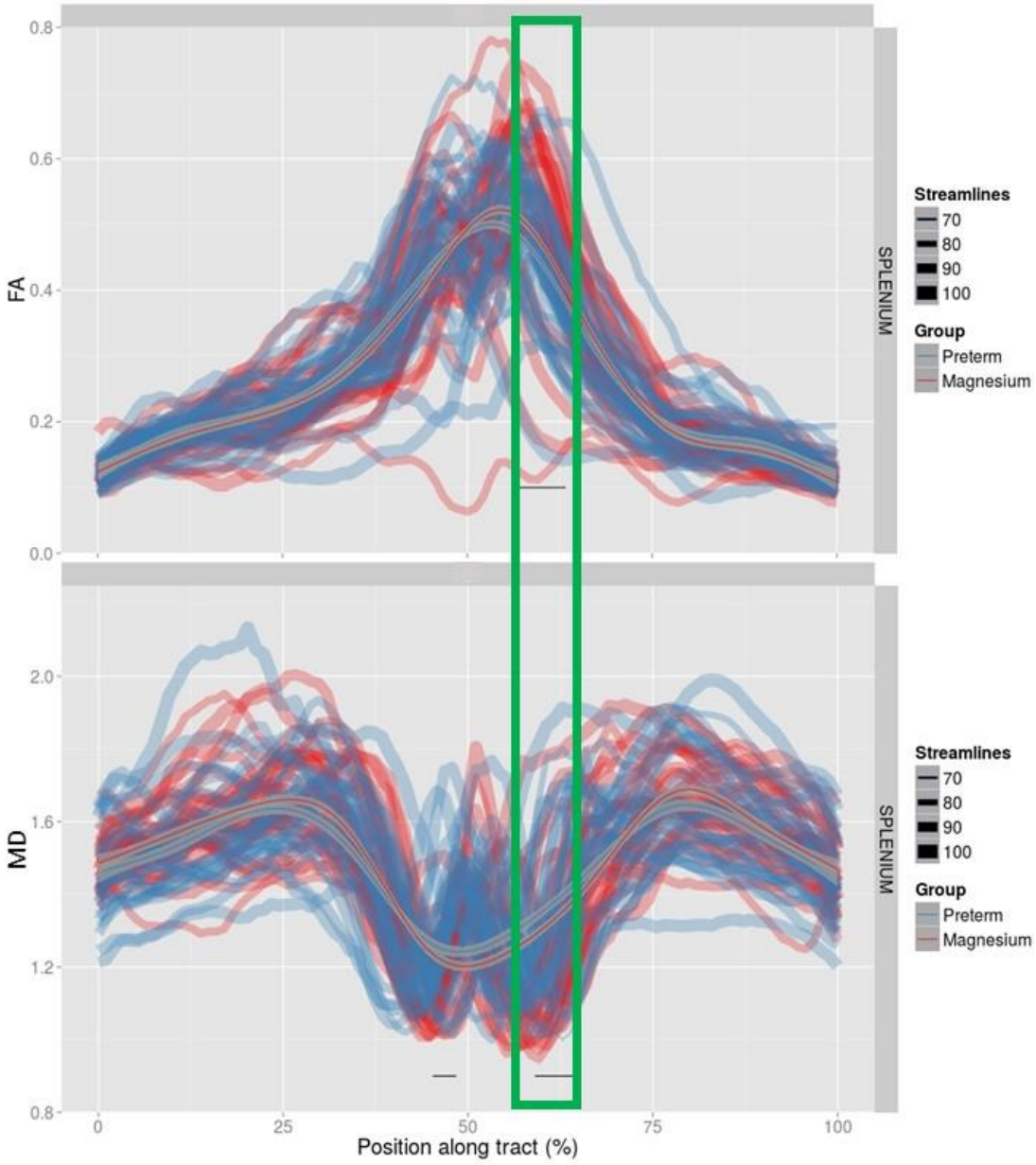

Figure 4.7: FA and MD plotted along the splenium of the corpus callosum, according to antenatal $MgSO_4$ exposure. Along-tract estimates from individual subjects are displayed semi-transparently in the background (line width encodes the relative number of streamlines, a reference for the numbers is in the figure key), and are overlaid with locally weighted smooth estimates of the group means (± pointwise 95% confidence range). The black bars at the bottom of each graph indicate the regions with a significant difference between groups. Squared in green is the area that presents differences in FA and MD.

Groupwise differences can be represented in anatomic space by plotting the *p-values* of mean difference in along-tract statistics overlaid on a representative image. Figures 4.8a and 4.8b show the *p*-value maps overlaid on a mean tract of one representative subject. Figures 4.8c and 4.8d show also the *p-value*, thresholded to visualise values < 0.05. Finally, Figures 4.8e and 4.8f shows the effect size.

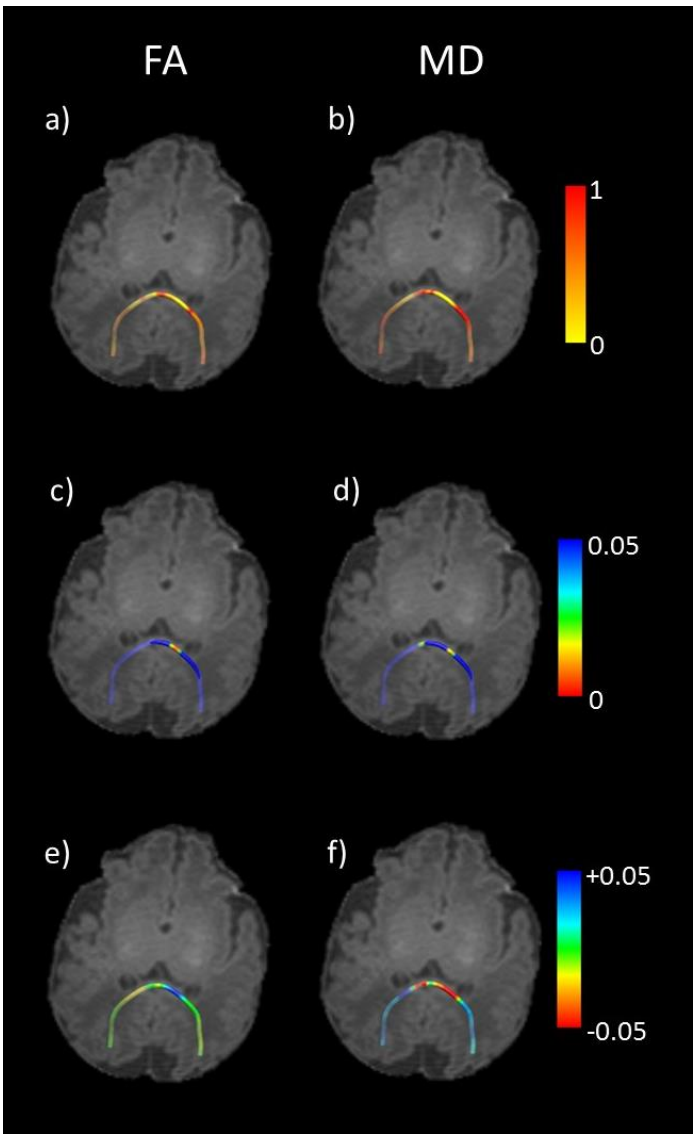

Figure 4.8: Along-tract statistics of the effect of antenatal MgSO4 in the splenium of the corpus callosum. a) Along-tract p-value maps of FA values overlaid on the mean tract of a representative subject; b) along-tract p-value maps of MD values overlaid on the mean tract of a representative subject a); c) and d) show visualisation of p-values <0.05; e) and f) along-tract effect size of FA and MD values overlaid on the mean tract of a representative subject (for FA, cool colours indicate higher FA in $MgSO_4$ exposed infants, and for MD hot colours indicate lower values in infants exposed to $MgSO_4$).

4.4. Discussion

We present a framework for neonatal connectome construction and tract analysis based on the use of learning based approaches and age-specific

atlases. It allows the incorporation of precise anatomical information to constrain streamline generation and provides detailed localised information about variations in FA and MD in regions of altered structural connectivity. We used the ACT framework with seeding at the GMWMI because it improves the biological plausibility of streamline generation, especially when a method to optimize the tractography is added (288, 289, 313). We found that connectivity of the splenium was altered in infants exposed to antenatal $MgSO_4$ versus those who were not which replicates a previous observation made using probabilistic neighbourhood tractography (PNT) (29, 319), and we provide additional information about the anatomic localisation of differences in FA and MD using along-tract statistics (290).

The main advantage of the proposed framework is a fully automated analytic process to construct the neonatal structrual connectome using age-specific and learning based tools in combination with along-tract statistics. Other advantages of this approach are that it can be implemented using any single-shell dMRI data with one structural volume of any contrast because of the EPI distortion correction strategy used (assuming a structural atlas is available for the age group of interest (204) and that assumptions required for ACT are met). Because generic approaches were used for skull-stripping and tissue segmentation, it is possible to generalize the framework for modelling the connectome longitudinally and in other age groups as long as an age-appropriate atlas is used (204). This may be useful for studying typical development, disease progression or treatment effects over the life course.

In the proposed framework water diffusion MRI data were up-sampled to T1w space. Previous studies have shown the benefits of this step, which include improved registration (320) and increased resolution to improve tractography (321). For our dataset there is another benefit: by matching the resolution of the T1w volume, it is possible to perform EPI distortion correction while retaining the relatively high resolution of structural data. To have both modalities (T1w and dMRI) correctly aligned and without distortions is a requirement of ACT.

We considered that a seeding strategy/tracking constraint based on anatomical information (GMWMI) would add value for streamline generation in the developing brain because: it overcomes the need for arbitrary FA thresholding for seeding; relatively lower dMRI resolution in neonatal imaging can lead to partial volume artefact at structures adjacent to CSF, which can lead to voxels at the CSF/tissue interface having an FA value > 0.1 or 0.15 thereby allowing tracts to pass through the CSF, and finally some WM regions present very low FA in the neonate and this can lead to missing tracts and connections. The application of LiFE, which is designed to remove false positives and redundant tracts, removed around half the tracts and this appeared to improve the quality of resulting connectomes (288, 322). It is important to note that if there are missing tracts, LiFE and other methods for optimizing tractography (288, 289, 313) will not correct the problem because they are not capable of adding tracts (311).

To perform connectivity analysis, we chose a strategy based on outlier removal: only connections with at least 5 tracts were counted, and after

separating the different groups connection values outside the range of mean ± 3 standard deviations were removed. The rationale for doing this is to explore as many connections as possible, while retaining interest in connections that could appear in one group only. This approach contrasts with standard backbone network or grid network methods for filtering networks, which take account of the whole group, not different sub-groups. Finally, we tracked fibres from the connections that showed differences for along-tract statistics, which enabled precise anatomic location of alterations in FA and MD values (290). To our knowledge, this is the first use of connectomics and along-tract statistics in an automated unified framework for groupwise comparisons.

To explore the clinical utility of the framework, we tested its efficacy for detecting an expected group-wise difference: specifically, we previously reported altered tract averaged MD in the splenium of the corpus callosum of preterm neonates exposed to antenatal $MgSO_4$ versus unexposed neonates using PNT (29). The present results are consistent in that we found altered connectivity in the splenium of the corpus callosum. Along-tract statistics revealed significantly increased FA and reduced MD at local regions along the splenium of the corpus callosum in infants exposed to antenatal $MgSO_4$ compared with unexposed infants, which is consistent with previous work in which a different technology was used (29).

There are some limitations to the framework. First, it is computationally expensive due to up-sampling of dMRI data, the application of LiFE, and the different registration steps; and second it could be refined further by using

different EPI distortion correction strategies, or with additional pre-processing steps such as removing Gibbs-ringing artefact (323). A limitation of the experiment presented is the low b-value of the acquired data. It is possible that results could be further improved with the use of high b-value or multi-shell acquisitions, which would be expected to resolve crossing fibres more effectively and allow for study of other scalar parameters along the tract (e.g. NODDI (139)).

4.5. Conclusion

In conclusion, we present a fully automated framework to construct the developing brain connectome using age-specific algorithms for brain extraction, tissue segmentation and labelling while incorporating anatomical information (ACT and GMWMI seeding) optimized with LiFE, and along-tract statistics. We demonstrate the utility of the framework for studying the effect of neuroprotective treatment strategies in preterm infants.

5. Early breast milk exposure modifies brain connectivity in preterm infants

5.1. Introduction

Preterm birth is strongly associated with an MRI phenotype that includes altered structural connectivity of developing neural systems, structural alteration in dGM and GM, and long term neurocognitive impairment (131, 147, 199, 324, 325). Co-morbidities of preterm birth, genetic factors, and environmental exposures contribute to WM disease but they do not explain fully the risks for atypical brain development and adverse outcome (69, 126, 127, 214, 326, 327).

Nutritional factors may play an important role in preterm brain development. For example, optimal protein and energy intakes in the first 28 days after preterm birth are associated with increased brain growth (328), and improved WM microstructural development at term equivalent age and neurodevelopmental performance at 18-months (31, 329).

Breastfeeding, when compared with formula feeding, is associated with increased performance in intelligence testing among the general population, and the effect may be enhanced in low birthweight infants (34-38). In a recent meta-analysis of studies that controlled for maternal intelligence, which is a recognised confounder of childhood cognition, breast feeding remained associated with a gain in performance in IQ testing (330). Furthermore,

breast milk appears to have lasting impact on cognition with improved performance at school, during adolescence and through to adulthood (331, 332). MRI studies of children and adolescents report that breast milk feed in infancy is associated with increased white and GM volumes (37, 333), increased cortical thickness (334) and improved WM microstructure (335) when compared with formula feeding. However, the extent to which observations from the general population can be extrapolated to preterm infants is unknown, and this leaves uncertainty about the effect of breast milk on preterm brain development, and the timing, dose and duration of breast milk that might confer benefit.

We combined nutritional data with brain MRI to test the hypothesis that exposure to breast milk enhances early brain development in preterm infants. We investigated the influence of breast milk intake during neonatal care on a comprehensive set of measures of brain development that are based on the MRI phenotype of preterm brain injury (69, 131, 193, 324). We combined sMR and dMRI to perform ACT (152) with SIFT (289) to construct the structural connectome, and compared connectomes using global network measures and edge-wise values using Network-based Statistics (NBS). We used TBSS to calculate voxel wise differences in FA, MD, AD, and RD across the WM skeleton, and used optimized algorithms for brain extraction and tissue classification to measure global and local brain tissue volumes (123, 127).

5.2. Subjects and Methods

5.2.1. Participants

Participants were preterm infants delivered at ≤ 33 weeks who received care at the Royal Infirmary of Edinburgh and had brain MRI performed at term-equivalent age as part of a longitudinal study designed to investigate the effects of preterm birth on brain structure and outcome.

Daily nutritional intake was collected from birth until discharge home from the neonatal unit using electronic patient records. Breast milk exposure was defined as the proportion of in-patient days receiving exclusive breast milk, categorized as ≥ 75% and ≥ 90% of days of in-patient care when exclusive breast milk was given.

The nutritional management of all participants conformed to following principles. Infants with birth weight < 1500 g began parenteral nutrition upon admission to neonatal care. This was delivered using a standard solution (Scottish Neonatal Parenteral Nutrition 2.4 g protein/100 ml, ITH Pharma, London), commencing at 100 ml/kg/day if birth weight < 1000 g and 75 ml/kg/day if birthweight was 1000-1500 g. This was increased to a maximum of 150 ml/kg/day in 25 ml/kg/day increments every 24 hours. Fat and fat-soluble vitamins were provided using Intralipid 20% emulsion, which was commenced within 24 hours of admission at 1 g/kg/day, increasing to 2 g/kg/day on day 2 and 3 g/kg/day on day 3.

Expression of breast milk was encouraged immediately after delivery and colostrum was given as soon as it became available. Enteral feeds were

commenced at 12 ml/kg/day on day one and incremented by 30 ml/kg/day as standard. This increment was reduced to 18 ml/kg/day in babies identified as at high risk of developing necrotising enterocolitis (< 1000 g, IUGR, absent or reversed umbilical artery end diastolic flow doppler). If there was insufficient maternal expressed breast milk by 48 hours of age, donor expressed breast milk was given to supplement maternal milk. Once infants had reached 120 ml/kg/day of enteral feeds, parenteral nutrition was stopped. Feeds continued to increment to a maximum volume of 180-200 ml/kg/day. Human milk fortifier (HMF) (Cow & Gate Nutriprem Human Milk Fortifier, Nutricia) was added to breast milk if weight gain remained sub-optimal despite 14 days of maximal volume breast milk (180-200 ml/kg/day). If mothers chose not to express milk or there was insufficient breast milk to meet the requirements of the infant beyond 34 weeks, donor expressed breast milk was replaced with preterm formula. All infants received multivitamins from day 7 of life and iron supplementation from day 42.

Bronchopulmonary dysplasia (BPD) was defined as the requirement for supplemental oxygen at 36 weeks corrected gestational age. All infants had placental histopathology performed and Histological chorioamnionitis (HCA) was defined using an established system (214).

Postnatal somatic growth was described as the difference between birthweight z-score and weight at scan z-score, calculated using INTERGROWTH-21st reference standards for preterm infants (336).

5.2.2. Structural connectivity

An overview of the complete framework for the network construction can be seen in Figure 5.1. This framework is mainly the one created in the previous chapter (Table A1).

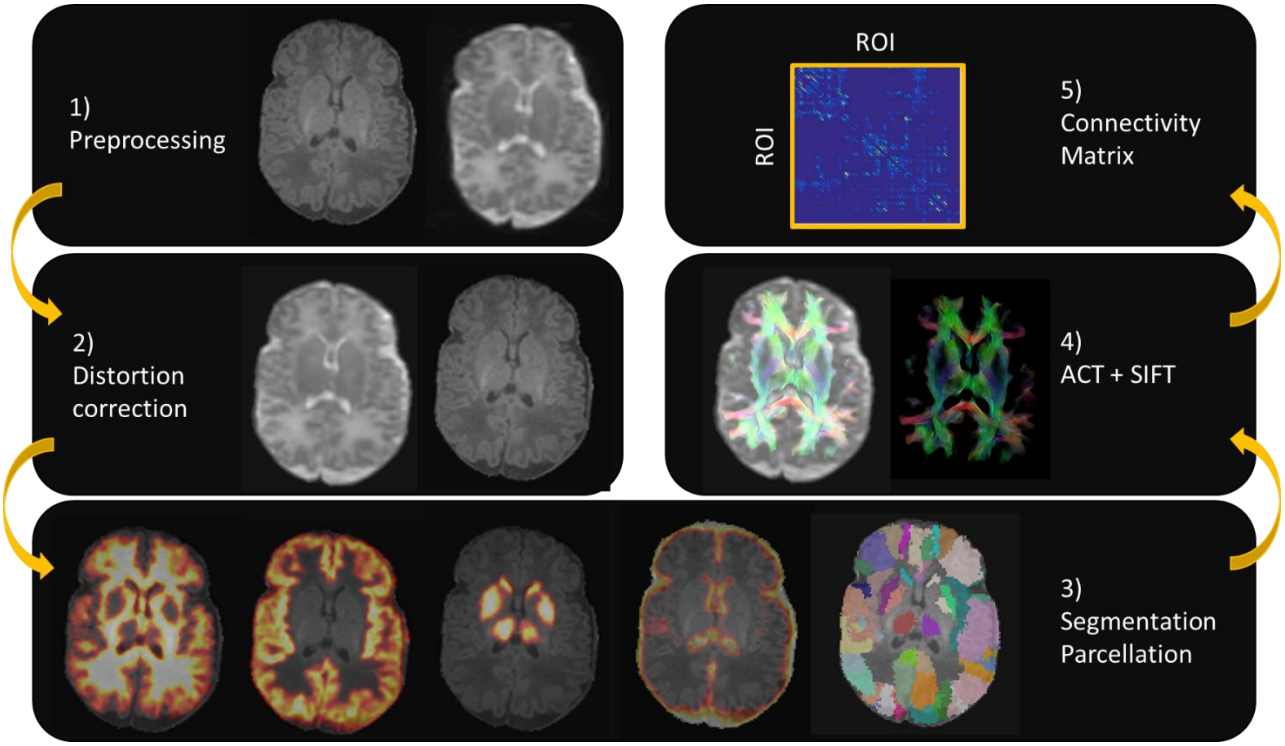

Figure 5.1. Overview of the structural connectome creation framework.

5.2.2.1. Preprocessing

Basically, the preprocessing was the same as explained in the previous chapter. The dMRI volumes underwent a denoising process (300, 303) followed by up-sampling by a factor of 2 to match the resolution of the T1w volumes using cubic b-spline interpolation (320). Then, the dMRI data were corrected for head motion and eddy current distortions (337) with the

correspondent vector rotation, skull-stripped (338) (with manual editing) and corrected for bias field inhomogeneity (257). The T1w volumes were skull-stripped (256) and corrected for bias field inhomogeneities (257). Finally, the T1w volumes were co-registered to the first B0 EPI volumes for each subject and dMRI data were corrected for EPI distortions by non-rigidly registering the EPI volumes to the co-registered T1w volumes, restricting the registration to the phase encoding direction (305, 306). At the end, for each voxel, the water diffusion tensor was estimated using the weighted least-squares method with DTIFIT (337). FA, MD, AD and RD maps were then generated for every subject.

5.2.2.2. Tissue segmentation and Parcellation

The same parcellation and segmentation methods used in the previous chapter, were used.

5.2.2.3. Tractography

Tractography was generated using constrained spherical deconvolution (cSD) (302, 339). The FOD was calculated with a maximum spherical harmonic degree (l_{max}) of 8 (309). We used ACT (152) with the iFOD2 algorithm (212). The ACT parameters were: seeding at the GMWMI; minimum streamline length of 20 mm and maximum length of 200 mm (183, 191); the remainder of parameters were used as default (adjusted for upsampled data (152)). 10 million tracts were generated and SIFT was applied to reduce the number of tracts to 2 million. This reduces the

construction bias of the tractogram and improves the biological accuracy and interpretability of structural connectivity between regions (289).

5.2.2.4. Network Construction

The connectomes were constructed following the same process explained in the previous chapter, resulting also in a matrix of 98x98. Note that the networks were not corrected for the inverse length of the paths, since this correction is not appropriate for tractograms calculated using a GMWMI seeding strategy (340). We refer to those matrices as streamline-weighted matrices (M^{w-NOS}).

In addition, FA-weighted connectomes were also constructed by using the mean FA computed over the $c_{i,j}$ streamlines as an edge weight: $w(e_{i,j}) = \frac{1}{c_{i,j}} \sum_{n=1}^{n=c_{i,j}} \overline{FA}_n$. Where *i*, *j*, $e_{i,j}$, $w(e_{i,j})$ and $c_{i,j}$are defined as before; *n* is each streamline connecting *i* and *j*; and $\overline{FA}_n$ is the mean FA of the tract *n*. This weight is known as the WM tract "integrity" (146, 194). We refer to those matrices as FA-weighted matrices (M^{w-FA}).

Finally, each M^{w-NOS} was binarized and used to filter the correspondent M^{w-FA}. The resulting M^{w-FA} connectomes were not normalised because the FA values for a region-pair connection are averaged across all its $c_{i,j}$streamlines, making it invariant to the number of tractography seeds used (146).

5.2.2.5. Edge-wise comparison

The M^{w-NOS} were thresholded keeping only the connections common to at least 2/3 of the subjects (341), and the threshold was then applied to the M^{w-FA}.

5.2.2.6. Network metrics and analysis

We calculated 5 network parameters: Global efficiency (GE), local efficiency (LE), cluster coefficient (CC), characteristic path length (CPL) and small-worldness (SW).

The CPL is defined as the average shortest path length between all pairs of nodes in the network and is the most commonly used measure of functional integration (342) and the GE is a reated measure defined as the average inverse shortest path length (343). the CPL is primarily influenced by long paths, while the GE is primarily influenced by short paths. Some authors have argued that this may make the GE a superior measure of integration (344).

Simple measures of segregation are based on the number of triangles in the network, with a high number of triangles implying segregation. The CC is the fraction of triangles around an individual node and is equivalent to the fraction of the node's neighbors that are also neighbors of each other. The LE is the GE computed on node neighborhoods, and is related to the CC.

A SW network is a type of network in which most nodes are not neighbors of one another, but the neighbors of any given node are likely to be neighbors of each other and most nodes can be reached from every other node by a small number of hops or steps (342). This is calculated by dividing the normalized CC between the normalized CPL.

A graphical representation can be seen in Figure 5.2. For a detailed explanation and the formulation of the metrics, see Rubinov and Sporns (2010). All the metrics were implemented in the Brain Connectivity Toolbox (brain-connectivity-toolbox.net) (171).

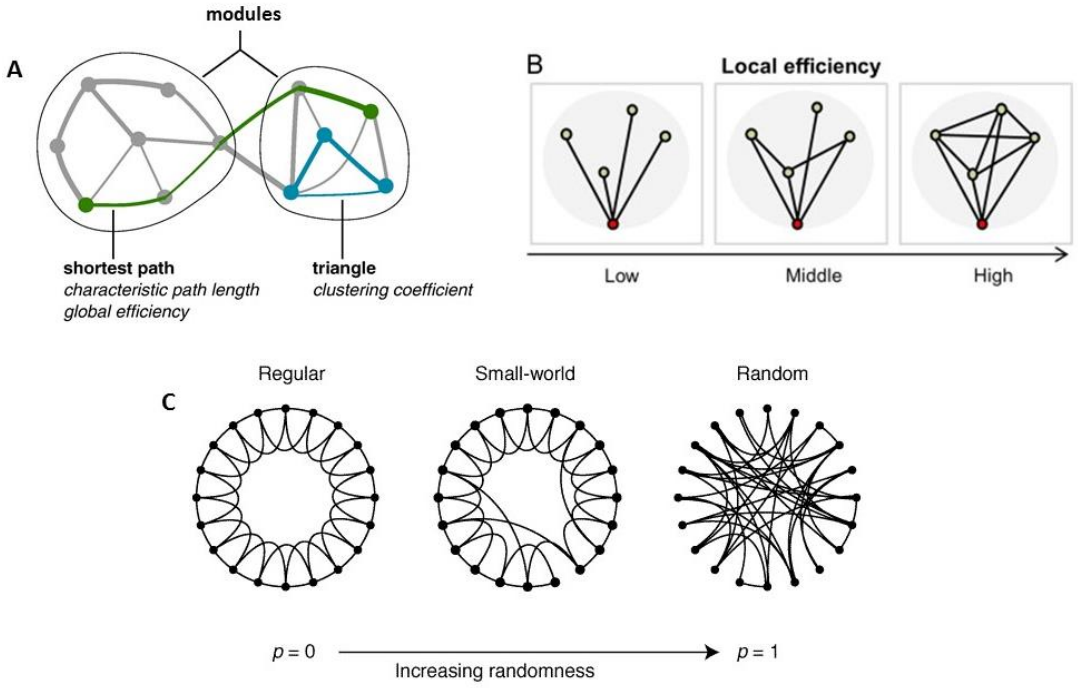

Figure 5.2. Graphical overview of the network metrics. A) The representation of CC, CPL and GE in a schematic network; B) How the increasing of the LE affects to a network, C) How a network goes to regular to random, passing to a SW network by increasing the randomness of its connections. Adapted from (171, 342, 345).

The connectivity matrices do not have the same density (sparsity, e.g. the number of connections in each connectivity matrix differs, due first to the removal of self-connections and second to the fact that not all the streamlines reach the different ROIs (340, 346). The density affects certain global topological parameters and comparisons at constant density make it possible to find differences related to the topological reorganization of links (347). To correct for this, each M^{w-NOS} was thresholded using its density in small steps from 0.02 to 0.5 in intervals of 0.02 (131, 344, 348). After this the matrix was binarized and used as a threshold to filter the M^{w-FA} for each subject (131).

5.2.3. Tract-based Spatial Statistics

TBSS analysis (123) was performed using a pipeline that was optimized for neonatal dMRI data (127). Using the most representative subject of the cohort as a target, an average FA map and mean FA skeleton (thresholded at FA > 0.15) were created from the aligned data representing the main WM tracts common to all subjects. RD, AD and MD were projected onto the FA skeleton for voxel wise comparisons.

5.2.4. Volumetric analysis

The brain tissue was separated from non-brain tissue using ALFA (256), and a brain mask was created. Volumes were corrected for field inhomogeneity using the N4 method (257) and were segmented using SEGMA (299). Every brain volume was segmented into: brainstem, cerebellum, cortical GM, CSF, dGM and WM (Figure 5.3). Volumes were calculated for each individual tissue type, and total brain tissue volume was calculated as the sum of all compartments with the exception of CSF.

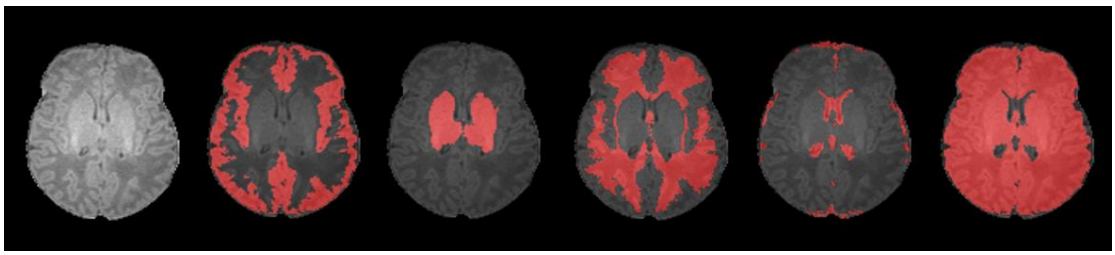

Figure 5.3: Tissue segmentations. From left to right: a single subject and the corresponding tissue segmentations for cortical gray matter, sub-cortical gray matter, WM, CSF and whole brain.

5.2.5 Exploratory analysis of dose effect

In exploratory analyses, we considered the effect of breast milk dose in group-wise comparisons using proportional daily breast milk intake threshold of ≥ 90%.

5.2.6. Statistics

Edge-wise comparison of connectivity matrices was performed using NBS (172) with a t-statistic exceeding a threshold of 3 (349). Groupwise difference in breast milk exposure in the five network measures was investigated using ANOVA (in the original matrices and also at each level of density). For TBSS, group comparisons were performed with FSL's Randomise tool using a general linear univariate model (350), with family-wise error correction for multiple comparisons using threshold-free cluster enhancement (TFCE) with a significance level of $p < 0.05$ (351). For volumetric comparisons group-wise analyses were performed using ANOVA. In all analyses post-menstrual age (PMA) at birth, PMA at image acquisition, BPD and exposure to chorioamnionitis were entered as covariates.

5.3. Results

5.3.1 Baseline characteristics

Forty-seven participants were studied. 27 received exclusive breastmilk feeds for ≥ 75% of their neonatal admission, and 20 received exclusive breastmilk feeds for <75% of their stay (Table 5.1). The demographic and clinical features of the population for the ≥ 90% exclusive breastmilk threshold are shown in Table 5.2.

Table 5.1: Demographic and clinical features of study participants (75%threshold)

	<75% exclusive BM (n=20)	≥75% exclusive BM (n=27)	p value
Mean GA at birth/weeks (range)	29^{+3} (23^{+2}-33^{+0})	29^{+3} (26^{+1}-32^{+6})	0.97
M:F ratio	8:12	12:15	0.76
Mean birthweight/g (range)	1121 (550-1450)	1160 (815-1465)	0.55
Mean birthweight z-score	-0.56	-0.37	0.55
Mean GA at scan/weeks (range)	39^{+5} (38^{+0}-42^{+2})	39^{+4} (38^{+0}-42^{+0})	0.83
Mean weight at scan/g (range)	2838 (2160-3480)	2862 (2070-4870)	0.87
Mean weight at scan z-score	-1.06	-1.01	0.88
Difference in mean weight z-score from birth to scan	-0.43	-0.65	0.32
Proportion of infants with BPD (%)	4/20 (20)	9/27 (33)	0.71
Proportion of infants with HCA (%)	6/20 (30)	9/27 (33)	0.81
Mean number of days in neonatal unit (range)	62 (19-151)	59 (26-94)	0.68
Mean number of TPN days (range)	9 (0-30)	9 (0-30)	0.90
Mean Urea concentration at 32 weeks GA/mmol/L (range)	2.5 (1.4-3.9)	2.7 (1.4-7.3)	0.64

Median number of exclusive formula days (range)	12 (0-107)	0 (0-10)	**<0.01**
Median number of exclusive breastmilk days (range)	19 (0-79)	57 (24-90)	**<0.01**
Median number of HMF days (range)	0 (0-58)	18 (0-62)	**<0.01**
Mean proportion of exclusive breastmilk days with supplemental DEBM, % (range)	18 (0-100)	3 (0-30)	**<0.01**

Table 5.2: Demographic and clinical features of study participants (90%threshold)

	<90% exclusive BM (n=24)	≥90% exclusive BM (n=23)	P value
Mean GA at birth/weeks (range)	29+4 (23+2-33+0)	29+1 (26+1-32+6)	0.47
M:F ratio	14:10	13:10	0.90
Mean birthweight/g (range)	1130 (550-1450)	1157 (815-1500)	0.67
Mean birthweight z-score	-0.66	-0.23	0.13
Mean GA at scan/weeks (range)	40+0 (38+0-42+2)	39+2 (38+0-42+0)	0.13
Mean weight at scan/g (range)	2823 (2070-3780)	2882 (2230-4870)	0.69
Mean weight at scan z-score	-1.17	-0.88	0.39
Difference in mean weight z-score from birth to scan	-0.46	-0.66	0.38
Proportion of infants with BPD (%)	5/24	8/23	0.29
Proportion of infants with HCA (%)	8/24	7/23	0.83
Mean number of days in neonatal unit (range)	61 (19-151)	59 (26-94)	0.72
Mean number of TPN days (range)	11 (0-30)	8 (0-16)	0.14
Mean Urea concentration at 32 weeks GA (mmol/L)	2.6 (1.4-6.0)	2.6 (1.3-7.3)	0.10
Median number of exclusive formula days (range)	11 (0-107)	0 (0)	**<0.01**
Median number of exclusive breastmilk days (range)	24 (0-79)	60 (24-90)	**<0.01**

Median number of HMF days (range)	0 (0-58)	20 (0-62)	**<0.01**
Mean proportion of exclusive breastmilk days with supplemental DEBM, % (range)	15 (0-100)	4 (0-30)	0.07

5.3.2. Edge-wise connectome comparison

A sub-network of M^{w-FA} shows increased FA in infants who received ≥ 75% of exclusive breast milk feeds compared to those who did not (p=0.0386, NBS) (Figure 5.4a); the complexity of the sub-network increased by the incorporation of more nodes and edges in infants who received ≥ 90% of exclusive breast milk feeds (p=0.0086, NBS) (Figure 5.4b). This sub-network included frontal to cingulate, frontal to precuneus and inter-hemispheric connections; detailed anatomical descriptions of the regions of interest are listed in Table 4.2.

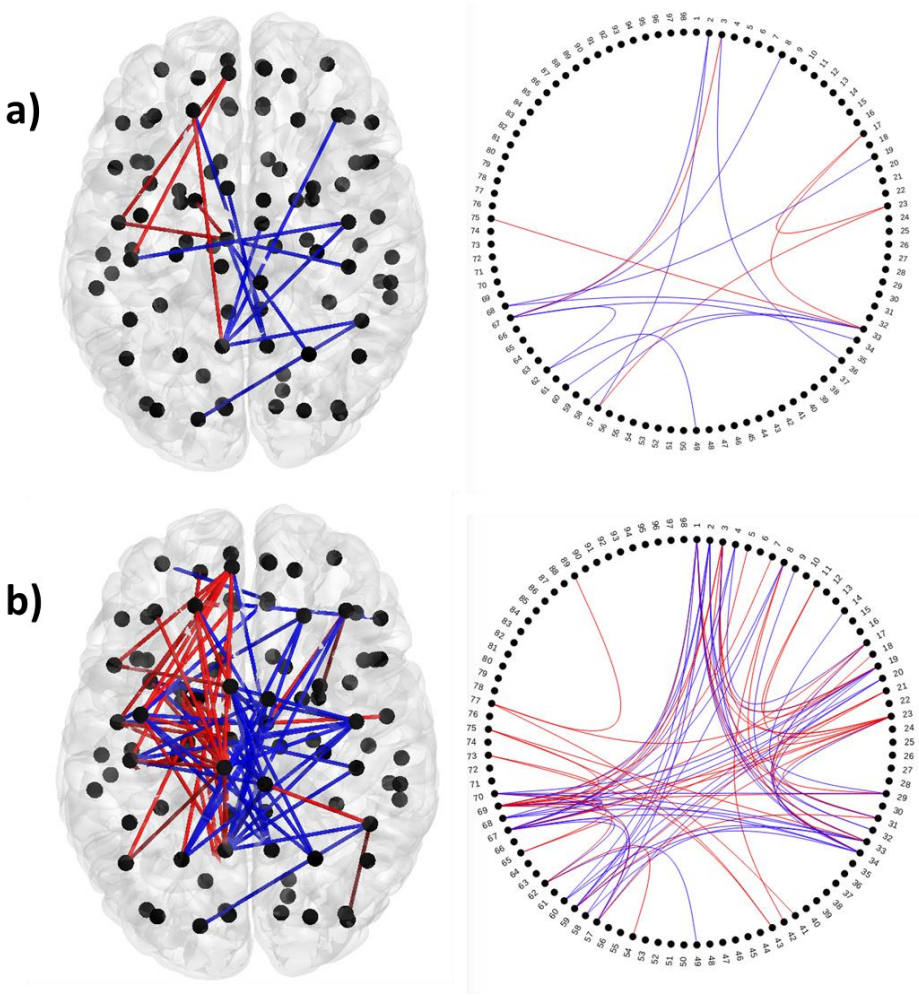

Figure 5.4: Sub-network showing differences in the FA-weighted connectome for the two thresholds: ≥ 75% (a) and ≥ 90% (b). Intra-hemispheric connections are shown in red, and inter-hemispheric connections in blue.

5.3.3. Network analysis

There were no statistically significant differences in global network metrics for M^{w-FA} at either milk intake threshold after FDR correction (Figure 5.5), nor were there significant differences in network measures corrected for density (Figure 5.6).

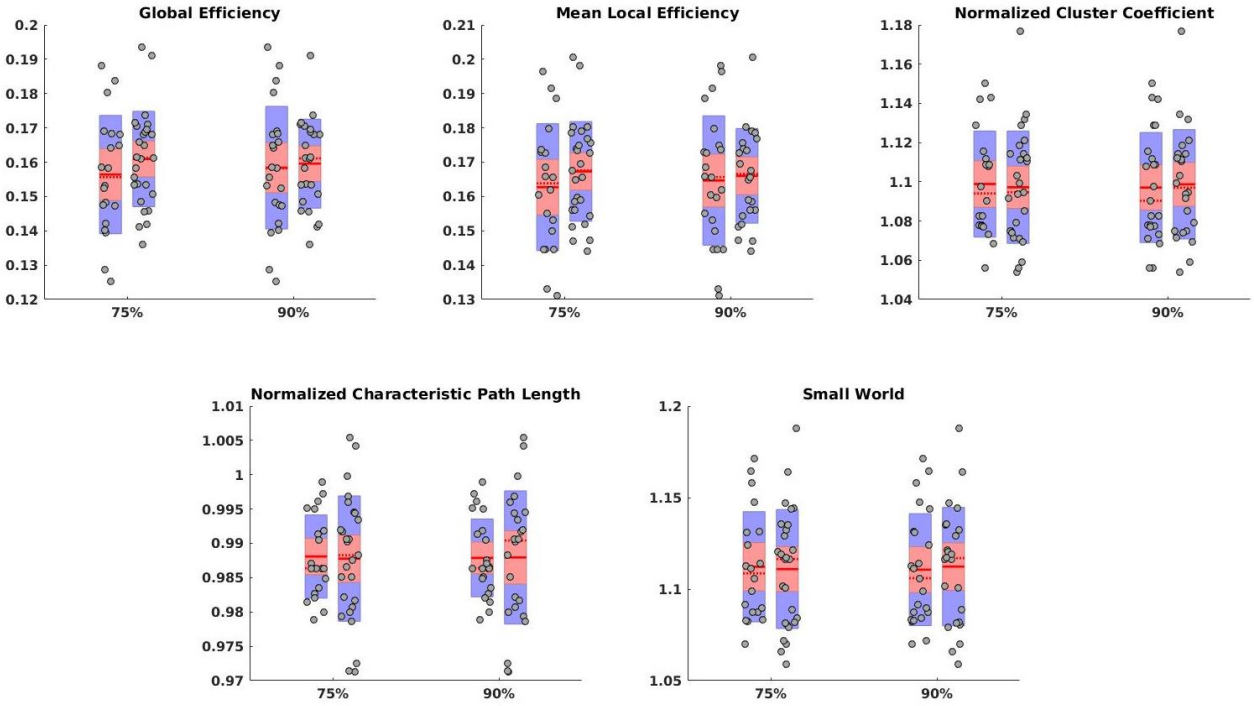

Figure 5.5: Plot of the different network metrics for the M^{w-FA} connectivity matrices. In each metric both thresholds are represented, namely ≥ 75% and ≥ 90%. For each threshold the box on the left represents the subjects with the lower breast milk dose and the box on the right the higher dose. The red line represents the mean; the red dotted line represents the median; the red box the 95% interval confidence of the mean; and the blue box the interval between the mean ± 1 standard deviation.

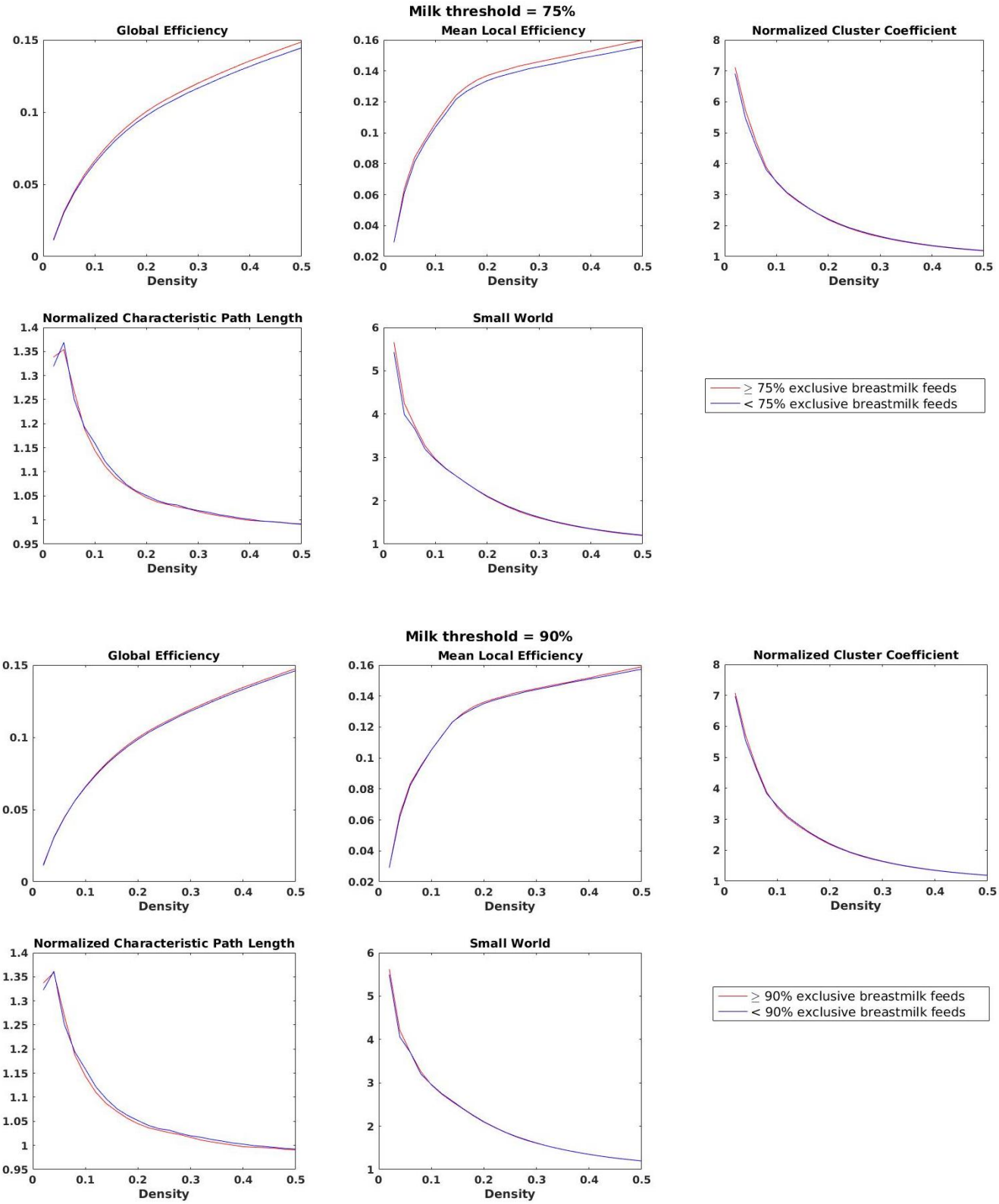

Figure 5.6: Plot of the different network metrics, as a function of the density. For the milk thresholds of 75% and 90%.

5.3.4. Tract-based spatial statistics

There were significant differences in water diffusion tensor parameters in major WM tracts associated with breast milk exposure. Specifically, in the group with ≥ 75% days of exclusive breast milk feeds, FA was higher in the splenium of corpus callosum, cingulum cingulate gyri, centrum semiovale, corticospinal tracts, the arcuate fasciculi and the posterior limbs of internal capsule. These differences were more widespread and symmetrical at the ≥ 90% exclusive breast milk days threshold. Infants who received ≥ 90% days exclusive breastmilk feeds had lower MD and RD (figure 5.7).

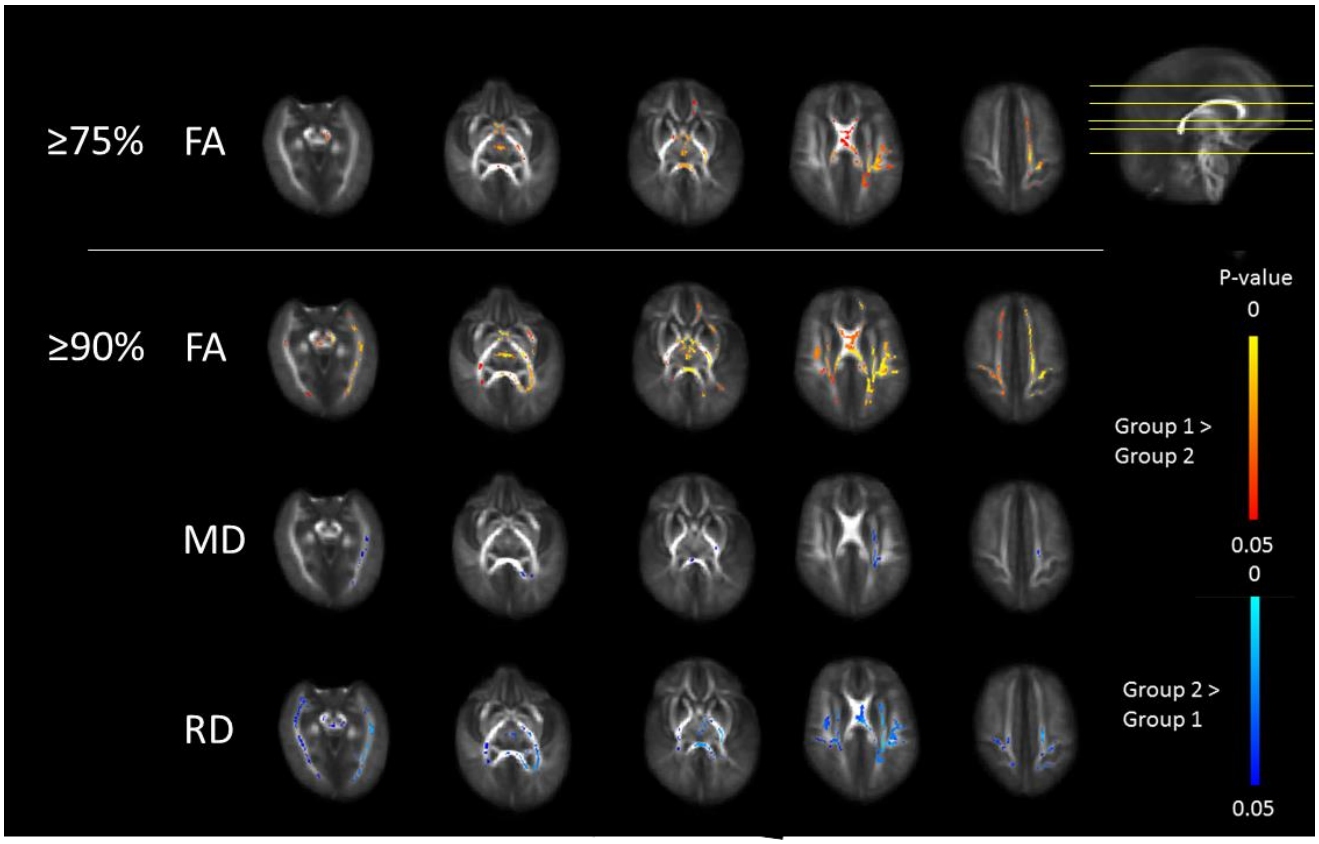

Figure 5.7: TBSS results showing differences in FA for each of the breast milk thresholds: 75% and 90%. Differences in MD and RD are highlighted in infants who received < 90% days exclusive breast milk. Group 1: higher than the specified threshold of exclusive breast milk and group 2: lower than the specified threshold of exclusive breast milk.

5.3.5. Volumetric Analysis

There were no significant differences in brain volumes between preterm infants who received ≥ 75% exclusive breast milk and those who received < 75% breast milk feeds (FDR corrected). The mean (SD) for the total brain tissue volume of the group with ≥ 75% breast milk exposure was 359.34 ml (38.76 ml), while for the group with < 75% breast milk exposure was 361.56 ml (34.65 ml). Values for tissue compartments and CSF are shown in Table

5.3. There were no significant differences either in brain volumes between preterm infants who received ≥ 90% exclusive breast milk and those who received < 90% breast milk feeds.

Table 5.3: Mean (SD) brain tissue and CSF volumes at term equivalent age.

	Mean volume (SD) / ml (≥75% exclusive breastmilk)	Mean volume (SD) / ml (< 75% exclusive breastmilk)	p-value
Cortical grey matter	169.81 (23.39)	170.64 (19.10)	0.87
Sub-cortical grey matter	25.99 (3.67)	25.52 (3.21)	0.58
White matter	135.17 (14.01)	136.27 (12.95)	0.79
Cerebrospinal fluid	75.42 (16.51)	81.50 (16.26)	0.16
Brainstem	5.07 (0.87)	5.30 (0.62)	0.28
Cerebellum	23.29 (3.28)	23.82 (3.21)	0.47
Whole Brain	359.34 (38.76)	361.56 (34.66)	0.81

5.4. Discussion

By combining nutritional data with brain MRI markers of preterm brain injury, we have shown that greater exposure to breast milk following preterm birth is associated with improved WM microstructure at term-equivalent age. We found differences in sub-networks of the FA-weighted connectome and increased FA within WM tracts of infants who received exclusive breast milk feeds for ≥ 75% days of neonatal in-patient care compared with infants who received exclusive breast milk for < 75% of days. These effects showed a dose-dependent relationship with breast milk exposure and were independent of known predictors of preterm brain injury including gestational age at birth, chorioamnionitis, and BPD. The observed effects are unlikely to be attributable to parenteral nutrition because exposure to this did not differ significantly between the groups.

Our data are consistent with neurodevelopmental outcome studies of preterm infants that report improved neurodevelopmental outcomes in association with breast feeding (35-38, 352). However, when outcomes are assessed in early childhood the effects of infant nutrition and other potential confounders limit inference about neonatal nutritional exposures. By parsing the complex behavioural trait of neurodevelopment to an intermediate phenotype (MRI markers of development at term equivalent age) we have shown that breast milk intake prior to discharge from hospital is critically important for optimal brain development after preterm birth. The results are consistent with observations that early life parenteral and enteral nutritional intake immediately after preterm birth is associated with altered brain development at term equivalent age (31, 329), but these data focus attention specifically on the role of breast milk. Breast milk is a complex nutritional substrate that has nutritional advantages over formula milk for promoting brain development. These include favourable composition and absorption of fats and protein, improved bioavailability of trace elements, and the presence of non-nutrient factors (milk oligosaccharides, immunoglobulins, lactoferrin and lysozymes) that may confer direct or indirect benefit (353, 354). Finally, the infant gut microbiome is affected by feeding practice (355); modifications to the gut-brain axis via microbiome are known to influence brain development and behaviour in mice (356) and to predict cognitive performance in infants at 2 years of age (357).

The main strength of the study is the comprehensive assessment of brain development using three measures that describe the encephalopathy of

prematurity: connectivity, tract microstructure, and local and global brain volumes. We were also able to explore dose effects. We evaluated infants at term equivalent age so are able to rule out confounding by nutrition throughout infancy and socio-economic features of the home environment. Finally, we used a pragmatic measure of breast milk exposure that is available to healthcare providers and parents from routinely recorded data, and does not require additional measurements.

A limitation of our work is that we were not able to investigate the effect of common genetic variation in fatty acid metabolism, which may interact with breast milk exposure to influence childhood cognition (358, 359) and WM development (326, 360); nor were we able to investigate genetic variants of the microglial inflammatory response linked to preterm WMI (327). Secondly, we performed a cross-sectional assessment at term equivalent age so could not investigate the putative benefits to the preterm brain of longer exposure to exclusive breast feeding through infancy. The sample size was not sufficient to study the effect of donor expressed breast milk or HMF on brain development.

We used cSD with probabilistic tracking because it is beneficial over standard diffusion tensor reconstructions for tractography in paediatric brain, even with low b-values (213). ACT and SIFT were used to reduce bias in the tractography reconstruction (152, 289, 340, 361), recent studies had shown this potential in the developing brain (131, 362). M^{w-FA} were chosen because FA is established as a reliable marker of brain development (127, 146, 193), but new models that rely on high b-value acquisitions to better

characterize crossing fibres within WM may provide additional insights into the effect of breast milk on early brain development (139).

5.5. Conclusion

In summary, these data show that WM tract microstructure and cerebral connectivity of preterm infants are increased at term equivalent age in association with higher exposure to breast milk.

6. Discussion

6.1. Main conclusions of the study

The main aim of this thesis was to create an optimized framework for structural connectivity creation, specially designed for the first wave of the TEBC. Going through all the steps involved in the process, first the parcellation, by creating an atlas derived from the cohort, followed by the optimisation of the pre-processing framework of the dMRI to be able to use ACT (152) and combine the connectome construction with along-tract statistics. The final framework was tested in different sub-cohorts derived from the EBC showing how different external factors, such as the usage of antenatal $MgSO_4$ and nutrition, can affect the structural connectivity of the preterm brain.

As has been discussed in the introduction, the neonatal structural connectivity framework still has several limitations compared with the adult frameworks.

I aimed to optimize the different steps involved in connectome construction by using tools specially designed/tested for neonates: to optimize the parcellation, an atlas especially developed from this cohort was created, allowing us to create a good parcellation of the T1w structural images collected in the cohort. For tractography creation, I proposed using up-sampled data to match the voxel size of the diffusion MRI data with the voxel size of the structural data to avoid losing resolution in the parcellation/segmentation of the data. Another important benefit derived from

up-sampling of the data is that with structural and diffusion data sharing the same resolution it is possible to correct for the EPI distortions inherent to phase encoding artefacts in the EPI sequence. By performing an EPI distortion correction with the accurate tissue segmentation created with SEGMA (299) and the ACT framework with GMWMI seeding (152, 154) which allowed us to create more biologically accurate tractography data, can be applied.

Finally, two steps for optimizing the tractography data were applied, namely LiFE (288) in the second chapter and SIFT (289) in the third. Every method has its own drawbacks and benefits over the other, but here, the goal of both is the same, specifically to minimize the biases associated with tractography generation. These problems include the fact that longer WM tracts present a greater volume from which to seed and in regions of complex architecture most streamline algorithms simply follow the most collinear fibre orientation introducing an imbalance in streamline densities (289). They achieve this goal by using different approaches. For example, LiFE uses the tractography data as an input to predict the original diffusion MRI data by modelling each tract using the “ball and stick” model and assigning its final weight to each tract in the reconstruction of the image. By doing this, the tracts with weight 0 can be removed from the tractography data. On the other hand, SIFT uses the tractography data as an input and tries to predict the FOD in each voxel by assigning the corresponding cross-sectional area of WM to each streamline. By multiplying this area with the streamline length through a

particular voxel, the volume occupied by the WM reconstructed by that individual streamline in that voxel is defined (289).

Both methods have been recently used in the literature and show improvements for the tractography reconstruction (288, 289, 310, 311, 340, 361, 363, 364). However, only SIFT has been used before in addition to ACT (340, 361), and to our knowledge, it has been used in neonates only by Batalle et al. (131).

This work presents an optimised and robust framework for analysing the structural connectome of the neonatal brain using methods specially designed for neonates and state of the art techniques. The framework has been designed and tested in the first wave of the TEBC. The results show an improvement of the tractography reconstruction data compared with commonly used methods, and this is reflected in the accuracy of the connectome construction and the derived connectivity measures.

The effect of different external factors on the preterm brain was tested. First and as a proof of concept to probe the accuracy of the framework, I tested the effect of antenatal $MgSO_4$ in a previously explored cohort reported by Anblagan et al.(29). I found similar results, namely an increase in FA and reduction in MD in the splenium of the corpus callosum (note that this is sometimes known as WM integrity, but this term is not the most appropriate except in cases of clinically-diagnosed conditions (134)). After the framework was designed and tested, it was applied to test the effect of the impact of breastmilk feeding on the preterm brain. An increment of FA was found, after correcting for some known factors that affect WM integrity, such as BPD and

chorioamnionitis. The results suggest that this improvement is dose dependent and is also localized in certain areas of the brain. The differences were found using NBS (172), but there were no differences in any of the explored global network topological measures, namely global and local efficiency, normalised characteristic path length, normalized clustering coefficient and small-worldness. TBSS (123, 127) and a volumetric analysis of the cohort were also performed. With TBSS the results were similar, an increase in the FA, which was also dose dependent, with higher exposure correlating with increased white matter connectivity. There were no differences in the volumes. These findings are consistent with previous results reported in the literature (365, 366).

6.2. Limitations

The data of the first wave of the TEBC was acquired between February 2013 and August 2015 using a single-shell protocol with a b-value of 750 s/mm^2 and a prioritization of T1w over the T2w scans. All the parameters were accurately selected at the time of data acquisition in order to start the project based on logic and precedents and were consistently kept throughout the whole project.

In the future these acquisition protocols could benefit from recent advances such as optimised multi-shell acquisitions with high b-values (367), reverse phase encoding acquisitions to improve the EPI distortion correction (368-

372), or basing the structural acquisitions on the T2w data to perform advance segmentations or surface based analysis methods (207, 373).

On the diffusion side, a high b-value would increase the angular resolution that it is possible to achieve with the FOD. Typically, with the data we acquired, researchers use a tensor based reconstruction with a deterministic tractography algorithm. However, even with this b-value, the tractography reconstruction can be improved using cSD with a probabilistic algorithm. This has been specially tested in paediatric and neonatal populations (213). With the reverse phase encoding acquisition, it will be possible to correct for EPI susceptibility distortions in a more accurate way (374). To have both structural and diffusion MRI data perfectly aligned and corrected for EPI distortion is one of the requirements for applying the ACT framework (152).

With a single-shell acquisition we are limited to the tensor derived metrics (FA, MD, etc.). These metrics have been used in the past to describe the integrity and complexity of the brain, and as a biomarker of brain development (375). However, it is also true that they have limitations in describing regions with complex WM microstructure. Due to this, new imaging maps (like NODDI (139)) should be used in addition to the previously existing maps, but the majority of those new maps require multi-shell acquisitions (139).

The choice of one of the methods for filtering the tractography data used also affects the final result. For example, LiFE models the WM using two compartments, the free water movement and the restricted diffusion. While this model is good for modelling the WM, when used in combination with

ACT, some of the tracts have segments inside both the GM and dGM regions. This results in the model not being accurate enough in these regions. Another potential limitation is that it is computationally expensive. For this reason I decided to track only 100,000 tracts in each brain (recently, a framework to encode structural brain connectomes and dMRI data using multidimensional arrays has been proposed and released, it reduces the memory requirements needed by a factor of 40 and is able to process much larger connectomes (376)); after the application of LiFE these tracts are reduced by 45-55%. The final number of streamlines is quite low to reliably ensure the reproducibility of the connectome. With SIFT, it is possible to process larger connectomes in a reasonable time. However, the main limitations of this method are that you need to manually choose the final number of tracts or a desired value for the convergence criteria (a new version of the algorithm is available, where instead of filtering the tractography, a weight is assigned to each tract (313)). Furthermore, the algorithm works by modelling the FOD from the tractography data, and if the FOD does not model the free water movement, the algorithm does not model it. Multi-shell acquisitions allow the CSF (free) to be modelled in the FOD, which will result in more accurate AFD measures and more precise fibre orientation estimates at the tissue interfaces, resulting in more accurate and precise fibre tracking in large parts of the brain (377).

6.3. Future work and direction

With the acquisition of the new datasets for the second wave of the TEBC, the proposed framework will evolve with the acquisition protocol and the new software developments. Recently, new tools have been developed for improving the preprocessing of the diffusion imaging data (323) that can be added to the framework. The new dataset comes with multi-shell data with reverse phase encoding acquisition and with T1w and T2w images acquired consistently for all subjects. This will allow us to improve the accuracy and speed of the processing. With reverse phase encoding it will be possible to apply field map based methods to correct for the EPI geometric distortion using topup/eddy (337, 368, 370). This will have two main benefits; first of all, an increase in the accuracy of the correction and registration of the structural imaging, as these methods have been shown to be more accurate than registration based methods (374). After this, to align the structural data with the diffusion data, a simple rigid registration step will be needed, thereby avoiding the non-linear registration step; the second inherent benefit will be an increase in the speed of the complete framework because up-sampling of the diffusion images won't be needed. This means less voxels would be involved in each proceeding step.

Multi-shell diffusion data has a lot of potential utilities and benefits over single shell acquisitions. In the tractography analysis, it will be possible to model different tissue responses (GM,WM and CSF) to obtain a FOD much more accurately (377). It will also allow the possibility to calculate more complex

diffusion maps (e.g. NODDI (139)) that better represents the complex WM microstructure in addition to the standard water diffusion tensor maps (FA, MD, etc.).

The consistent acquisition of T2w images is also very beneficial for parcellation/segmentation purposes (207), as it has been shown in the literature that structural analyses based on T2w images are more accurate that those based on T1w images (299).

The phenotypic data of the TEBC are very rich – socieconomics, genomics, eye-tracking, psychology – and when combined with imaging information in future analyses, will support mechanistic studies designed to discover causal tracts with regard to risk and resilience in brain growth, and early life biomarker development. These are essential steps in the research pathway of developing and evaluating new therapeutic strategies.

Another important issue for the development of this field is the creation of two large projects aimed at helping us to better understand the developing connectome: the developing human connectome project (dHCP) (http://www.developingconnectome.org/) and the baby connectome project (BCP) (http://www.babyconnectomeproject.org/) (378). Those two projects aim to better understand how a healthy human brain develops and works. Researchers will characterize human brain connectivity and map patterns of structural and functional connectivity to important behavioural skills from infancy to early childhood. Additional biological (e.g., genetic markers) and environmental measures (e.g., family demographics) will be collected and examined to provide a more comprehensive picture of the factors that affect

brain development. This knowledge will be tremendously useful in understanding brain function and how early interventions may shape our brain throughout our lifespan.

At some point it will be possible for researchers to combine these data (which will be available to all the research community) with their own datasets (for example the TEBC) and establish different collaborations with groups around the world to further the understanding of brain development in childhood and beyond.

7. References

1. Blencowe H, Cousens S, Chou D, Oestergaard M, Say L, Moller AB, et al. Born too soon: the global epidemiology of 15 million preterm births. Reprod Health. 2013;10 Suppl 1:S2.

2. Yoshida S, Martines J, Lawn JE, Wall S, Souza JP, Rudan I, et al. Setting research priorities to improve global newborn health and prevent stillbirths by 2025. Journal of Global Health. 2016;6(1):010508.

3. Liu L, Oza S, Hogan D, Perin J, Rudan I, Lawn JE, et al. Global, regional, and national causes of child mortality in 2000–13, with projections to inform post-2015 priorities: an updated systematic analysis. The Lancet. 2015;385(9966):430-40.

4. Lawn JE, Wilczynska-Ketende K, Cousens SN. Estimating the causes of 4 million neonatal deaths in the year 2000. International Journal of Epidemiology. 2006;35(3):706-18.

5. Romero R, Espinoza J, Kusanovic JP, Gotsch F, Hassan S, Erez O, et al. The preterm parturition syndrome. BJOG: An International Journal of Obstetrics & Gynaecology. 2006;113:17-42.

6. Behrman RE, Butler AS. In: Behrman RE, Butler AS, editors. Preterm Birth: Causes, Consequences, and Prevention. The National Academies Collection: Reports funded by National Institutes of Health. Washington (DC)2007.

7. Monnelly VJ, Anblagan D, Quigley A, Cabez MB, Cooper ES, Mactier H, et al. Prenatal methadone exposure is associated with altered neonatal

brain development. NeuroImage: Clinical. 2018;18:9-14.

8. Lockwood CJ, Toti P, Arcuri F, Paidas M, Buchwalder L, Krikun G, et al. Mechanisms of Abruption-Induced Premature Rupture of the Fetal Membranes : Thrombin-Enhanced Interleukin-8 Expression in Term Decidua. The American Journal of Pathology. 2005;167(5):1443-9.

9. Roizen JD, Asada M, Tong M, Tai H-H, Muglia LJ. Preterm Birth without Progesterone Withdrawal in 15-Hydroxyprostaglandin Dehydrogenase Hypomorphic Mice. Molecular Endocrinology. 2008;22(1):105-12.

10. Tobi EW, Heijmans BT, Kremer D, Putter H, Delemarre-van de Waal HA, Finken MJ, et al. DNA methylation of IGF2, GNASAS, INSIGF and LEP and being born small for gestational age. Epigenetics. 2011;6(2):171-6.

11. Zhang G, Feenstra B, Bacelis J, Liu X, Muglia LM, Juodakis J, et al. Genetic Associations with Gestational Duration and Spontaneous Preterm Birth. New England Journal of Medicine. 2017;377(12):1156-67.

12. Bezold KY, Karjalainen MK, Hallman M, Teramo K, Muglia LJ. The genomics of preterm birth: from animal models to human studies. Genome Medicine. 2013;5(4):34-.

13. Hassan SS, Romero R, Berry SM, Dang K, Blackwell SC, Treadwell MC, et al. Patients with an ultrasonographic cervical length ≤15 mm have nearly a 50% risk of early spontaneous preterm delivery. American Journal of Obstetrics and Gynecology. 2000;182(6):1458-67.

14. Chandiramani M, Shennan A. Preterm labour: update on prediction and prevention strategies. Current Opinion in Obstetrics and Gynecology.

2006;18(6):618-24.

15. Clark CAC, Woodward LJ, Horwood LJ, Moor S. Development of Emotional and Behavioral Regulation in Children Born Extremely Preterm and Very Preterm: Biological and Social Influences. Child Development. 2008;79(5):1444-62.

16. Elgen S, Leversen K, Grundt J, Hurum J, Sundby A, Elgen I, et al. Mental health at 5 years among children born extremely preterm: a national population-based study. European Child & Adolescent Psychiatry. 2012;21(10):583-9.

17. Johnson S, Hollis C, Kochhar P, Hennessy E, Wolke D, Marlow N. Psychiatric Disorders in Extremely Preterm Children: Longitudinal Finding at Age 11 Years in the EPICure Study. Journal of the American Academy of Child & Adolescent Psychiatry. 2010;49(5):453-63.e1.

18. Bhutta AT, Cleves MA, Casey PH, Cradock MM, Anand KS. Cognitive and behavioral outcomes of school-aged children who were born preterm: A meta-analysis. Jama. 2002;288(6):728-37.

19. Wood NS, Marlow N, Costeloe K, Gibson AT, Wilkinson AR. Neurologic and Developmental Disability after Extremely Preterm Birth. New England Journal of Medicine. 2000;343(6):378-84.

20. Kerr-Wilson CO, Mackay DF, Smith GCS, Pell JP. Meta-analysis of the association between preterm delivery and intelligence. Journal of Public Health. 2012;34(2):209-16.

21. Moore T, Hennessy EM, Myles J, Johnson SJ, Draper ES, Costeloe KL, et al. Neurological and developmental outcome in extremely preterm

children born in England in 1995 and 2006: the EPICure studies2012 2012-12-04 23:32:33.

22. Crump C, Winkleby MA, Sundquist K, Sundquist J. Preterm birth and psychiatric medication prescription in young adulthood: a Swedish national cohort study. International Journal of Epidemiology. 2010;39(6):1522-30.

23. Moster D, Lie RT, Markestad T. Long-Term Medical and Social Consequences of Preterm Birth. New England Journal of Medicine. 2008;359(3):262-73.

24. Nosarti C, Reichenberg A, Murray RM, et al. PReterm birth and psychiatric disorders in young adult life. Archives of general psychiatry. 2012;69(6):610-7.

25. Marlow N, Wolke D, Bracewell MA, Samara M. Neurologic and Developmental Disability at Six Years of Age after Extremely Preterm Birth. New England Journal of Medicine. 2005;352(1):9-19.

26. Vohr BR, Wright LL, Poole WK, McDonald SA. Neurodevelopmental Outcomes of Extremely Low Birth Weight Infants <32 Weeks' Gestation Between 1993 and 1998. Pediatrics. 2005;116(3):635-43.

27. Doyle LW, Crowther CA, Middleton P, Marret S. Magnesium sulphate for women at risk of preterm birth for neuroprotection of the fetus. Cochrane Database Syst Rev. 2007(3):CD004661.

28. Rouse DJ, Hirtz DG, Thom E, Varner MW, Spong CY, Mercer BM, et al. A Randomized, Controlled Trial of Magnesium Sulfate for the Prevention of Cerebral Palsy. New England Journal of Medicine. 2008;359(9):895-905.

29. Anblagan D, Bastin ME, Sparrow S, Piyasena C, Pataky R, Moore EJ, et al. Tract shape modeling detects changes associated with preterm birth and neuroprotective treatment effects. NeuroImage: Clinical. 2015;8(0):51-8.

30. Moore EJ, Boardman JP. Modifiable risk factors for preterm brain injury. Paediatrics and Child Health. 2014;24(9):401-6.

31. Coviello C, Keunen K, Kersbergen KJ, Groenendaal F, Leemans A, Peels B, et al. Effects of early nutrition and growth on brain volumes, white matter microstructure and neurodevelopmental outcome in preterm newborns. 2017.

32. Stephens BE, Walden RV, Gargus RA, Tucker R, McKinley L, Mance M, et al. First-Week Protein and Energy Intakes Are Associated With 18-Month Developmental Outcomes in Extremely Low Birth Weight Infants. Pediatrics. 2009;123(5):1337-43.

33. Tan M, Abernethy L, Cooke R. Improving head growth in preterm infants – a randomised controlled trial II: MRI and developmental outcomes in the first year. Archives of Disease in Childhood - Fetal and Neonatal Edition. 2008;93(5):F342-F6.

34. Anderson JW, Johnstone BM, Remley DT. Breast-feeding and cognitive development: a meta-analysis. The American journal of clinical nutrition. 1999;70(4):525-35.

35. Vohr BR, Poindexter BB, Dusick AM, McKinley LT, Wright LL, Langer JC, et al. Beneficial effects of breast milk in the neonatal intensive care unit on the developmental outcome of extremely low birth weight infants at 18 months of age. Pediatrics. 2006;118(1):e115-23.

36. Vohr BR, Poindexter BB, Dusick AM, McKinley LT, Higgins RD, Langer JC, et al. Persistent beneficial effects of breast milk ingested in the neonatal intensive care unit on outcomes of extremely low birth weight infants at 30 months of age. Pediatrics. 2007;120(4):e953-9.

37. Isaacs EB, Fischl BR, Quinn BT, Chong WK, Gadian DG, Lucas A. Impact of breast milk on intelligence quotient, brain size, and white matter development. Pediatr Res. 2010;67(4):357-62.

38. Lucas A, Morley R, Cole TJ. Randomised trial of early diet in preterm babies and later intelligence quotient. BMJ : British Medical Journal. 1998;317(7171):1481-7.

39. Foulder-Hughes LA, Cooke RWI. Motor, cognitive, and behavioural disorders in children born very preterm. Developmental Medicine & Child Neurology. 2003;45(2):97-103.

40. Marlow N, Hennessy EM, Bracewell MA, Wolke D. Motor and Executive Function at 6 Years of Age After Extremely Preterm Birth. Pediatrics. 2007;120(4):793-804.

41. Goyen T-A, Lui K. Developmental coordination disorder in “apparently normal” schoolchildren born extremely preterm. Archives of Disease in Childhood. 2009;94(4):298-302.

42. Saigal S, Ouden Ld, Wolke D, Hoult L, Paneth N, Streiner DL, et al. School-Age Outcomes in Children Who Were Extremely Low Birth Weight From Four International Population-Based Cohorts. Pediatrics. 2003;112(4):943-50.

43. Taylor HG, Klein N, Minich NM, Hack M. Middle-School-Age

Outcomes in Children with Very Low Birthweight. Child Development. 2000;71(6):1495-511.

44. Austeng D, Källen KM, Ewald UW, Jakobsson PG, Holmström GE. Incidence of retinopathy of prematurity in infants born before 27 weeks' gestation in sweden. Archives of Ophthalmology. 2009;127(10):1315-9.

45. Repka MX. Ophthalmological problems of the premature infant. Mental retardation and developmental disabilities research reviews. 2002;8(4):249-57.

46. Johnson S, Fawke J, Hennessy E, Rowell V, Thomas S, Wolke D, et al. Neurodevelopmental Disability Through 11 Years of Age in Children Born Before 26 Weeks of Gestation. Pediatrics. 2009;124(2):e249-e57.

47. Hintz SR, Kendrick DE, Vohr BR, Poole WK, Higgins RD. Changes in Neurodevelopmental Outcomes at 18 to 22 Months' Corrected Age Among Infants of Less Than 25 Weeks' Gestational Age Born in 1993–1999. Pediatrics. 2005;115(6):1645-51.

48. Jacobs SE, O'Brien K, Inwood S, Kelly EN, Whyte HE. Outcome of infants 23-26 weeks' gestation pre and post surfactant. Acta Pædiatrica. 2000;89(8):959-65.

49. Lefebvre F, Glorieux J, St-Laurent-Gagnon T. Neonatal survival and disability rate at age 18 months for infants born between 23 and 28 weeks of gestation. American Journal of Obstetrics and Gynecology. 1996;174(3):833-8.

50. Wilson-Costello D, Friedman H, Minich N, Fanaroff AA, Hack M. Improved Survival Rates With Increased Neurodevelopmental Disability for

Extremely Low Birth Weight Infants in the 1990s. Pediatrics. 2005;115(4):997-1003.

51. Mercier C FK, Howard D, Soll R. the Vermont Oxford Network Follow-up Study Group. Severe disability in surviving extremely low birth weight infants: The Vermont Oxford Network Experience. 2005.

52. Mikkola K, Ritari N, Tommiska V, Salokorpi T, Lehtonen L, Tammela O, et al. Neurodevelopmental Outcome at 5 Years of Age of a National Cohort of Extremely Low Birth Weight Infants Who Were Born in 1996–1997. Pediatrics. 2005;116(6):1391-400.

53. Hack M, Taylor H. Perinatal brain injury in preterm infants and later neurobehavioral function. Jama. 2000;284(15):1973-4.

54. Hansen BM, Greisen G. Is improved survival of very-low-birth weight infants in the 1980s and 1990s associated with increasing intellectual deficit in surviving children? Developmental Medicine & Child Neurology. 2004;46(12):812-5.

55. Doyle LW, Anderson PJ. Improved neurosensory outcome at 8 years of age of extremely low birthweight children born in Victoria over three distinct eras. Archives of Disease in Childhood - Fetal and Neonatal Edition. 2005;90(6):F484-F8.

56. Botting N, Powls A, Cooke RWI, Marlow N. Attention Deficit Hyperactivity Disorders and Other Psychiatric Outcomes in Very Low Birthweight Children at 12 Years. Journal of Child Psychology and Psychiatry. 1997;38(8):931-41.

57. Indredavik M, Vik T, Heyerdahl S, Kulseng S, Fayers P, Brubakk A.

Psychiatric symptoms and disorders in adolescents with low birth weight. Archives of Disease in Childhood Fetal and Neonatal Edition. 2004;89(5):F445-F50.

58. Nosarti C, Giouroukou E, Micali N, Rifkin L, Morris RG, Murray RM. Impaired executive functioning in young adults born very preterm. Journal of the International Neuropsychological Society. 2007;13(4):571-81.

59. Allin M, Walshe M, Fern A, Nosarti C, Cuddy M, Rifkin L, et al. Cognitive maturation in preterm and term born adolescents. Journal of Neurology, Neurosurgery & Psychiatry. 2008;79(4):381-6.

60. Fawke J, Lum S, Kirkby J, Hennessy E, Marlow N, Rowell V, et al. Lung Function and Respiratory Symptoms at 11 Years in Children Born Extremely Preterm: The EPICure Study. American journal of respiratory and critical care medicine. 2010;182(2):237-45.

61. McEniery CM, Bolton CE, Fawke J, Hennessy E, Stocks J, Wilkinson IB, et al. Cardiovascular consequences of extreme prematurity: the EPICure study. Journal of Hypertension. 2011;29(7):1367-73.

62. Johnson S, Marlow N. Early and long-term outcome of infants born extremely preterm. Archives of Disease in Childhood. 2016.

63. Hambleton G, Wigglesworth JS. Origin of intraventricular haemorrhage in the preterm infant. Archives of Disease in Childhood. 1976;51(9):651-9.

64. Ballabh P. Intraventricular Hemorrhage in Premature Infants: Mechanism of Disease. Pediatr Res. 2010;67(1):1-8.

65. Vohr B, Ment LR. Intraventricular hemorrhage in the preterm infant.

Early human development. 1996;44(1):1-16.

66. Volpe JJ. Neurobiology of Periventricular Leukomalacia in the Premature Infant. Pediatr Res. 2001;50:553.

67. Volpe JJ. Brain injury in premature infants: a complex amalgam of destructive and developmental disturbances. The Lancet Neurology. 2009;8(1):110-24.

68. Edwards AD, Redshaw ME, Kennea N, Rivero-Arias O, Gonzales-Cinca N, Nongena P, et al. Effect of MRI on preterm infants and their families: a randomised trial with nested diagnostic and economic evaluation. Archives of Disease in Childhood - Fetal and Neonatal Edition. 2017.

69. Inder TE, Warfield SK, Wang H, Hüppi PS, Volpe JJ. Abnormal Cerebral Structure Is Present at Term in Premature Infants. Pediatrics. 2005;115(2):286-94.

70. Woodward LJ, Anderson PJ, Austin NC, Howard K, Inder TE. Neonatal MRI to Predict Neurodevelopmental Outcomes in Preterm Infants. New England Journal of Medicine. 2006;355(7):685-94.

71. Hinojosa-Rodríguez M, Harmony T, Carrillo-Prado C, Van Horn JD, Irimia A, Torgerson C, et al. Clinical neuroimaging in the preterm infant: Diagnosis and prognosis. NeuroImage: Clinical. 2017;16(Supplement C):355-68.

72. Robinson S, Li Q, DeChant A, Cohen ML. Neonatal loss of γ–aminobutyric acid pathway expression after human perinatal brain injury. Journal of neurosurgery. 2006;104(6 Suppl):396-408.

73. Back SA, Luo NL, Mallinson RA, O'Malley JP, Wallen LD, Frei B, et al.

Selective vulnerability of preterm white matter to oxidative damage defined by F2-isoprostanes. Annals of neurology. 2005;58(1):108-20.

74. Haynes RL, Folkerth RD, Keefe RJ, Sung I, Swzeda LI, Rosenberg PA, et al. Nitrosative and oxidative injury to premyelinating oligodendrocytes in periventricular leukomalacia. Journal of neuropathology and experimental neurology. 2003;62(5):441-50.

75. Back SA, Miller SP. Brain injury in premature neonates: A primary cerebral dysmaturation disorder? Annals of neurology. 2014;75(4):469-86.

76. Billiards SS, Haynes RL, Folkerth RD, Borenstein NS, Trachtenberg FL, Rowitch DH, et al. RESEARCH ARTICLE: Myelin Abnormalities without Oligodendrocyte Loss in Periventricular Leukomalacia. Brain Pathology. 2008;18(2):153-63.

77. Thompson DK, Warfield SK, Carlin JB, Pavlovic M, Wang HX, Bear M, et al. Perinatal risk factors altering regional brain structure in the preterm infant. Brain. 2007;130(3):667-77.

78. Reiss AL, Kesler SR, Vohr B, Duncan CC, Katz KH, Pajot S, et al. Sex differences in cerebral volumes of 8-year-olds born preterm. J Pediatr. 2004;145(2):242-9.

79. Peterson BS, Vohr B, Staib LH, Cannistraci CJ, Dolberg A, Schneider KC, et al. Regional brain volume abnormalities and long-term cognitive outcome in preterm infants. Jama. 2000;284(15):1939-47.

80. Yang Z, Covey MV, Bitel CL, Ni L, Jonakait GM, Levison SW. Sustained neocortical neurogenesis after neonatal hypoxic/ischemic injury. Annals of neurology. 2007;61(3):199-208.

81. Sizonenko SV, Camm EJ, Dayer A, Kiss JZ. Glial responses to neonatal hypoxic–ischemic injury in the rat cerebral cortex. International Journal of Developmental Neuroscience. 2008;26(1):37-45.

82. Lee Y, Morrison BM, Li Y, Lengacher S, Farah MH, Hoffman PN, et al. Oligodendroglia metabolically support axons and contribute to neurodegeneration. Nature. 2012;487(7408):443-8.

83. Thompson DK, Lee KJ, Egan GF, Warfield SK, Doyle LW, Anderson PJ, et al. Regional white matter microstructure in very preterm infants: Predictors and 7 year outcomes. Cortex; a journal devoted to the study of the nervous system and behavior. 2014;52:60-74.

84. Nossin-Manor R, Card D, Morris D, Noormohamed S, Shroff MM, Whyte HE, et al. Quantitative MRI in the very preterm brain: Assessing tissue organization and myelination using magnetization transfer, diffusion tensor and T1 imaging. NeuroImage. 2013;64:505-16.

85. Chau V, Synnes A, Grunau RE, Poskitt KJ, Brant R, Miller SP. Abnormal brain maturation in preterm neonates associated with adverse developmental outcomes. Neurology. 2013;81(24):2082-9.

86. Brunssen SH, Jean Harry G. Diffuse White Matter Injury and Neurologic Outcomes of Infants Born Very Preterm in the 1990s. Journal of Obstetric, Gynecologic & Neonatal Nursing. 2007;36(4):386-95.

87. Panigrahy A, Wisnowski JL, Furtado A, Lepore N, Paquette L, Bluml S. Neuroimaging biomarkers of preterm brain injury: toward developing the preterm connectome. Pediatric radiology. 2012;42(0 1):S33-S61.

88. de Vries LS, Eken P, Dubowitz LMS. The spectrum of leukomalacia

using cranial ultrasound. Behavioural Brain Research. 1992;49(1):1-6.

89. Martinez-Biarge M, Groenendaal F, Kersbergen KJ, Benders MJNL, Foti F, Cowan FM, et al. MRI Based Preterm White Matter Injury Classification: The Importance of Sequential Imaging in Determining Severity of Injury. PloS one. 2016;11(6):e0156245.

90. Papile L-A, Burstein J, Burstein R, Koffler H. Incidence and evolution of subependymal and intraventricular hemorrhage: A study of infants with birth weights less than 1,500 gm. The Journal of Pediatrics. 1978;92(4):529-34.

91. Blankenberg FG, Loh N-N, Bracci P, D'Arceuil HE, Rhine WD, Norbash AM, et al. Sonography, CT, and MR Imaging: A Prospective Comparison of Neonates with Suspected Intracranial Ischemia and Hemorrhage. American Journal of Neuroradiology. 2000;21(1):213-8.

92. Martino F, Malova M, Cesaretti C, Parazzini C, Doneda C, Ramenghi LA, et al. Prenatal MR imaging features of isolated cerebellar haemorrhagic lesions. European Radiology. 2016;26(8):2685-96.

93. Skiöld B, Horsch S, Hallberg B, Engström M, Nagy Z, Mosskin M, et al. White matter changes in extremely preterm infants, a population-based diffusion tensor imaging study. Acta Pædiatrica. 2010;99(6):842-9.

94. Dyet LE, Kennea N, Counsell SJ, Maalouf EF, Ajayi-Obe M, Duggan PJ, et al. Natural history of brain lesions in extremely preterm infants studied with serial magnetic resonance imaging from birth and neurodevelopmental assessment. Pediatrics. 2006;118(2):536-48.

95. Inder TE, Wells SJ, Mogridge NB, Spencer C, Volpe JJ. Defining the

nature of the cerebral abnormalities in the premature infant: a qualitative magnetic resonance imaging study. The Journal of Pediatrics. 2003;143(2):171-9.

96. Inder T, Huppi PS, Zientara GP, Maier SE, Jolesz FA, di Salvo D, et al. Early detection of periventricular leukomalacia by diffusion-weighted magnetic resonance imaging techniques. The Journal of Pediatrics. 1999;134(5):631-4.

97. Counsell SJ, Allsop JM, Harrison MC, Larkman DJ, Kennea NL, Kapellou O, et al. Diffusion-weighted imaging of the brain in preterm infants with focal and diffuse white matter abnormality. Pediatrics. 2003;112(1 Pt 1):1-7.

98. Krishnan ML, Dyet LE, Boardman JP, Kapellou O, Allsop JM, Cowan F, et al. Relationship between white matter apparent diffusion coefficients in preterm infants at term-equivalent age and developmental outcome at 2 years. Pediatrics. 2007;120(3):e604-9.

99. Back SA. Perinatal white matter injury: the changing spectrum of pathology and emerging insights into pathogenetic mechanisms. Mental retardation and developmental disabilities research reviews. 2006;12(2):129-40.

100. De Vries LS, Van Haastert IL, Rademaker KJ, Koopman C, Groenendaal F. Ultrasound abnormalities preceding cerebral palsy in high-risk preterm infants. J Pediatr. 2004;144(6):815-20.

101. de Vries LS, Rademaker KJ, Groenendaal F, Eken P, van Haastert IC, Vandertop WP, et al. Correlation between neonatal cranial ultrasound, MRI in

infancy and neurodevelopmental outcome in infants with a large intraventricular haemorrhage with or without unilateral parenchymal involvement. Neuropediatrics. 1998;29(4):180-8.

102. Guzzetta F, Shackelford GD, Volpe S, Perlman JM, Volpe JJ. Periventricular intraparenchymal echodensities in the premature newborn: critical determinant of neurologic outcome. Pediatrics. 1986;78(6):995-1006.

103. Sherlock RL, Anderson PJ, Doyle LW. Neurodevelopmental sequelae of intraventricular haemorrhage at 8 years of age in a regional cohort of ELBW/very preterm infants. Early human development. 2005;81(11):909-16.

104. De Vries LS, Groenendaal F, van Haastert IC, Eken P, Rademaker KJ, Meiners LC. Asymmetrical myelination of the posterior limb of the internal capsule in infants with periventricular haemorrhagic infarction: an early predictor of hemiplegia. Neuropediatrics. 1999;30(6):314-9.

105. Bassan H, Limperopoulos C, Visconti K, Mayer DL, Feldman HA, Avery L, et al. Neurodevelopmental Outcome in Survivors of Periventricular Hemorrhagic Infarction. Pediatrics. 2007;120(4):785-92.

106. Fetters L, Huang H-h. Motor development and sleep, play, and feeding positions in very-low-birthweight infants with and without white matter disease. Developmental Medicine & Child Neurology. 2007;49(11):807-13.

107. Glass HC, Fujimoto S, Ceppi-Cozzio C, Bartha AI, Vigneron DB, Barkovich AJ, et al. White matter injury is associated with impaired gaze in premature infants. Pediatric neurology. 2008;38(1):10-5.

108. Rezaie P, Dean A. Periventricular leukomalacia, inflammation and white matter lesions within the developing nervous system. Neuropathology.

2002;22(3):106-32.

109. Gururaj AK, Sztriha L, Bener A, Dawodu A, Eapen V. Epilepsy in children with cerebral palsy. Seizure. 2003;12(2):110-4.

110. Dubowitz LM, Bydder GM, Mushin J. Developmental sequence of periventricular leukomalacia. Correlation of ultrasound, clinical, and nuclear magnetic resonance functions. Archives of Disease in Childhood. 1985;60(4):349-55.

111. Despotovi, #x107, I, Goossens B, Philips W. MRI Segmentation of the Human Brain: Challenges, Methods, and Applications. Computational and Mathematical Methods in Medicine. 2015;2015:23.

112. Arslan S, Ktena SI, Makropoulos A, Robinson EC, Rueckert D, Parisot S. Human brain mapping: A systematic comparison of parcellation methods for the human cerebral cortex. NeuroImage. 2017.

113. Glasser MF, Van Essen DC. Mapping Human Cortical Areas In Vivo Based on Myelin Content as Revealed by T1- and T2-Weighted MRI. The Journal of Neuroscience. 2011;31(32):11597-616.

114. Einstein A, Fürth R. Investigations on the theory of Brownian movement. New York, N.Y.: Dover Publications; 1956.

115. Stejskal EO, Tanner JE. Spin Diffusion Measurements: Spin Echoes in the Presence of a Time-Dependent Field Gradient. The Journal of Chemical Physics. 1965;42(1):288-92.

116. Le Bihan D, Breton E. Imagerie de diffusion in-vivo par résonance magnétique nucléaire. Comptes-Rendus de l'Académie des Sciences. 1985;93(5):27-34.

117. Moseley ME, Cohen Y, Mintorovitch J, Chileuitt L, Shimizu H, Kucharczyk J, et al. Early detection of regional cerebral ischemia in cats: Comparison of diffusion- and T2-weighted MRI and spectroscopy. Magnetic Resonance in Medicine. 1990;14(2):330-46.

118. Alexander ALH, S.L. Samsonov, A.A. Adluru, N. Hosseinbor, A.P. Mossahebi, P. Tromp, D.P.M. Zakszewski, E. Field, A.S. Characterization of Cerebral White Matter Properties Using Quantitative Magnetic Resonance Imaging Stains. Brain Connectivity 2012.

119. Basser PJ, Mattiello J, LeBihan D. MR diffusion tensor spectroscopy and imaging. Biophysical Journal. 1994;66(1):259-67.

120. Tuch DS. Q-ball imaging. Magnetic Resonance in Medicine. 2004;52(6):1358-72.

121. Tournier JD, Calamante F, Gadian DG, Connelly A. Direct estimation of the fiber orientation density function from diffusion-weighted MRI data using spherical deconvolution. NeuroImage. 2004;23(3):1176-85.

122. Wedeen VJ, Wang RP, Schmahmann JD, Benner T, Tseng WYI, Dai G, et al. Diffusion spectrum magnetic resonance imaging (DSI) tractography of crossing fibers. NeuroImage. 2008;41(4):1267-77.

123. Smith SM, Jenkinson M, Johansen-Berg H, Rueckert D, Nichols TE, Mackay CE, et al. Tract-based spatial statistics: voxelwise analysis of multi-subject diffusion data. Neuroimage. 2006;31(4):1487-505.

124. Alloza C, Bastin ME, Cox SR, Gibson J, Duff B, Semple SI, et al. Central and non-central networks, cognition, clinical symptoms, and polygenic risk scores in schizophrenia. Human Brain Mapping.n/a-n/a.

125. Buchanan CR, Pettit LD, Storkey AJ, Abrahams S, Bastin ME. Reduced structural connectivity within a prefrontal-motor-subcortical network in amyotrophic lateral sclerosis. Journal of Magnetic Resonance Imaging. 2015;41(5):1342-52.

126. Ball G, Aljabar P, Nongena P, Kennea N, Gonzalez-Cinca N, Falconer S, et al. Multimodal image analysis of clinical influences on preterm brain development. Annals of neurology. 2017;82(2):233-46.

127. Ball G, Counsell SJ, Anjari M, Merchant N, Arichi T, Doria V, et al. An optimised tract-based spatial statistics protocol for neonates: applications to prematurity and chronic lung disease. Neuroimage. 2010;53(1):94-102.

128. Pecheva D, Zhang H, Ball G, Rutherford M, Kennea N, Hajnal J, et al., editors. Tract-specific analysis of white matter fasciculi in a large cohort of preterm infants. ISMRM; 2016; Singapore.

129. van Kooij BJ, de Vries LS, Ball G, van Haastert IC, Benders MJ, Groenendaal F, et al. Neonatal tract-based spatial statistics findings and outcome in preterm infants. AJNR American journal of neuroradiology. 2012;33(1):188-94.

130. Anjari M, Srinivasan L, Allsop JM, Hajnal JV, Rutherford MA, Edwards AD, et al. Diffusion tensor imaging with tract-based spatial statistics reveals local white matter abnormalities in preterm infants. Neuroimage. 2007;35(3):1021-7.

131. Batalle D, Hughes EJ, Zhang H, Tournier JD, Tusor N, Aljabar P, et al. Early development of structural networks and the impact of prematurity on brain connectivity. NeuroImage. 2017;149:379-92.

132. Counsell SJ, Shen Y, Boardman JP, Larkman DJ, Kapellou O, Ward P, et al. Axial and radial diffusivity in preterm infants who have diffuse white matter changes on magnetic resonance imaging at term-equivalent age. Pediatrics. 2006;117(2):376-86.

133. Barnett ML, Tusor N, Ball G, Chew A, Falconer S, Aljabar P, et al. Exploring the multiple-hit hypothesis of preterm white matter damage using diffusion MRI. NeuroImage: Clinical. 2018;17(Supplement C):596-606.

134. Jones DK, Knösche TR, Turner R. White matter integrity, fiber count, and other fallacies: The do's and don'ts of diffusion MRI. NeuroImage. 2013;73(Supplement C):239-54.

135. Jeurissen B, Leemans A, Tournier JD, Jones DK, Sijbers J. Investigating the prevalence of complex fiber configurations in white matter tissue with diffusion magnetic resonance imaging. Hum Brain Mapp. 2013;34(11):2747-66.

136. Tournier J-D, Mori S, Leemans A. Diffusion tensor imaging and beyond. Magnetic Resonance in Medicine. 2011;65(6):1532-56.

137. Assaf Y, Basser PJ. Composite hindered and restricted model of diffusion (CHARMED) MR imaging of the human brain. NeuroImage. 2005;27(1):48-58.

138. Assaf Y, Blumenfeld-Katzir T, Yovel Y, Basser PJ. AxCaliber: A Method for Measuring Axon Diameter Distribution from Diffusion MRI. Magnetic resonance in medicine. 2008;59(6):1347-54.

139. Zhang H, Schneider T, Wheeler-Kingshott CA, Alexander DC. NODDI: Practical in vivo neurite orientation dispersion and density imaging of the

human brain. NeuroImage. 2012;61(4):1000-16.

140. Alexander DC, Dyrby TB, Nilsson M, Zhang H. Imaging brain microstructure with diffusion MRI: practicality and applications. NMR in biomedicine.e3841-n/a.

141. Mori S, Crain BJ, Chacko VP, van Zijl PC. Three-dimensional tracking of axonal projections in the brain by magnetic resonance imaging. Annals of neurology. 1999;45(2):265-9.

142. Conturo TE, Lori NF, Cull TS, Akbudak E, Snyder AZ, Shimony JS, et al. Tracking neuronal fiber pathways in the living human brain. Proceedings of the National Academy of Sciences of the United States of America. 1999;96(18):10422-7.

143. Berman J. Diffusion MR Tractography As a Tool for Surgical Planning. Magnetic Resonance Imaging Clinics of North America. 2009;17(2):205-14.

144. Corouge I, Fletcher PT, Joshi S, Gouttard S, Gerig G. Fiber tract-oriented statistics for quantitative diffusion tensor MRI analysis. Medical Image Analysis. 2006;10(5):786-98.

145. Goodlett CB, Fletcher PT, Gilmore JH, Gerig G. Group analysis of DTI fiber tract statistics with application to neurodevelopment. NeuroImage. 2009;45(1, Supplement 1):S133-S42.

146. Brown CJ, Miller SP, Booth BG, Andrews S, Chau V, Poskitt KJ, et al. Structural network analysis of brain development in young preterm neonates. NeuroImage. 2014;101:667-80.

147. van den Heuvel MP, Kersbergen KJ, de Reus MA, Keunen K, Kahn RS, Groenendaal F, et al. The Neonatal Connectome During Preterm Brain

Development. Cerebral cortex. 2015;25(9):3000-13.

148. Shi F, Yap P-T, Gao W, Lin W, Gilmore JH, Shen D. Altered structural connectivity in neonates at genetic risk for schizophrenia: A combined study using morphological and white matter networks. NeuroImage. 2012;62(3):1622-33.

149. Gupta A, Poe MD, Styner MA, Panigrahy A, Escolar ML. Regional differences in fiber tractography predict neurodevelopmental outcomes in neonates with infantile Krabbe disease. NeuroImage : Clinical. 2015;7:792-8.

150. Pieterman K, Batalle D, Dudink J, Tournier JD, Hughes EJ, Barnett M, et al. Cerebello-cerebral connectivity in the developing brain. Brain structure & function. 2017;222(4):1625-34.

151. Geng X, Gouttard S, Sharma A, Gu H, Styner M, Lin W, et al. Quantitative tract-based white matter development from birth to age 2 years. NeuroImage. 2012;61(3):542-57.

152. Smith RE, Tournier J-D, Calamante F, Connelly A. Anatomically-constrained tractography: Improved diffusion MRI streamlines tractography through effective use of anatomical information. NeuroImage. 2012;62(3):1924-38.

153. Girard G, Whittingstall K, Deriche R, Descoteaux M. Towards quantitative connectivity analysis: reducing tractography biases. Neuroimage. 2014;98:266-78.

154. Li L, Rilling JK, Preuss TM, Glasser MF, Hu X. The effects of connection reconstruction method on the interregional connectivity of brain networks via diffusion tractography. Human Brain Mapping. 2012;33(8):1894-

913.

155. Rutherford M, Srinivasan L, Dyet L, Ward P, Allsop J, Counsell S, et al. Magnetic resonance imaging in perinatal brain injury: clinical presentation, lesions and outcome. Pediatric radiology. 2006;36(7):582-92.

156. Kwon SH, Vasung L, Ment LR, Huppi PS. The role of neuroimaging in predicting neurodevelopmental outcomes of preterm neonates. Clinics in perinatology. 2014;41(1):257-83.

157. Back SA. Cerebral White and Gray Matter Injury in Newborns: New Insights into Pathophysiology and Management. Clinics in perinatology. 2014;41(1):1-24.

158. Sotiras A, Davatzikos C, Paragios N. Deformable medical image registration: a survey. IEEE transactions on medical imaging. 2013;32(7):1153-90.

159. Klein A, Andersson J, Ardekani BA, Ashburner J, Avants B, Chiang MC, et al. Evaluation of 14 nonlinear deformation algorithms applied to human brain MRI registration. Neuroimage. 2009;46(3):786-802.

160. Rueckert D, Sonoda LI, Hayes C, Hill DLG, Leach MO, Hawkes DJ. Nonrigid registration using free-form deformations: application to breast MR images. Medical Imaging, IEEE Transactions on. 1999;18(8):712-21.

161. Avants BB, Epstein CL, Grossman M, Gee JC. Symmetric diffeomorphic image registration with cross-correlation: evaluating automated labeling of elderly and neurodegenerative brain. Med Image Anal. 2008;12(1):26-41.

162. Hajnal JH, D.J. Hill, D.L. Medical image registration. 2001.

163. Bom IMJvd, Klein S, Staring M, Homan R, Bartels LW, Pluim JPW, editors. Evaluation of optimization methods for intensity-based 2D-3D registration in x-ray guided interventions. SPIE Medical Imaging; 2011: SPIE.

164. Klein S, Staring M, Pluim JP. Evaluation of optimization methods for nonrigid medical image registration using mutual information and B-splines. IEEE transactions on image processing : a publication of the IEEE Signal Processing Society. 2007;16(12):2879-90.

165. Maes F, Vandermeulen D, Suetens P. Comparative evaluation of multiresolution optimization strategies for multimodality image registration by maximization of mutual information. Medical Image Analysis. 1999;3(4):373-86.

166. Hagmann P. From diffusion MRI to brain connectomics: EPFL; 2005.

167. Sporns O, Tononi G, Kotter R. The human connectome: A structural description of the human brain. PLoS computational biology. 2005;1(4):e42.

168. Clayden JD. Imaging connectivity: MRI and the structural networks of the brain. Functional neurology. 2013;28(3):197-203.

169. Funnell MG, Corballis PM, Gazzaniga MS. Cortical and subcortical interhemispheric interactions following partial and complete callosotomy. Archives of neurology. 2000;57(2):185-9.

170. Fornito AZ, A.; Bullmore, E.T. Chapter 11 - Statistical Connectomics. Fundamentals of Brain Network Analysis. San Diego: Academic Press; 2016. p. 383-419.

171. Rubinov M, Sporns O. Complex network measures of brain connectivity: Uses and interpretations. NeuroImage. 2010;52(3):1059-69.

172. Zalesky A, Fornito A, Bullmore ET. Network-based statistic: Identifying differences in brain networks. NeuroImage. 2010;53(4):1197-207.

173. Ingalhalikar M, Smith A, Parker D, Satterthwaite TD, Elliott MA, Ruparel K, et al. Sex differences in the structural connectome of the human brain. Proceedings of the National Academy of Sciences of the United States of America. 2014;111(2):823-8.

174. Li Y, Liu Y, Li J, Qin W, Li K, Yu C, et al. Brain Anatomical Network and Intelligence. PLoS computational biology. 2009;5(5):e1000395.

175. Liu Y, Liang M, Zhou Y, He Y, Hao Y, Song M, et al. Disrupted small-world networks in schizophrenia. Brain. 2008;131(4):945-61.

176. Rubinov M, Bullmore E. Schizophrenia and abnormal brain network hubs. Dialogues in Clinical Neuroscience. 2013;15(3):339-49.

177. Damoiseaux JS, Greicius MD. Greater than the sum of its parts: a review of studies combining structural connectivity and resting-state functional connectivity. Brain Structure and Function. 2009;213(6):525-33.

178. Phillips DJ, McGlaughlin A, Ruth D, Jager LR, Soldan A, Alzheimer's Disease Neuroimaging I. Graph theoretic analysis of structural connectivity across the spectrum of Alzheimer's disease: The importance of graph creation methods. NeuroImage : Clinical. 2015;7:377-90.

179. Collin G, Heuvel MPvd. The Ontogeny of the Human Connectome. The Neuroscientist. 2013;19(6):616-28.

180. Calabrese E, Badea A, Cofer G, Qi Y, Johnson GA. A Diffusion MRI Tractography Connectome of the Mouse Brain and Comparison with Neuronal Tracer Data. Cerebral Cortex (New York, NY). 2015;25(11):4628-

37.

181. Donahue CJ, Sotiropoulos SN, Jbabdi S, Hernandez-Fernandez M, Behrens TE, Dyrby TB, et al. Using Diffusion Tractography to Predict Cortical Connection Strength and Distance: A Quantitative Comparison with Tracers in the Monkey. The Journal of Neuroscience. 2016;36(25):6758-70.

182. van den Heuvel MP, Bullmore ET, Sporns O. Comparative Connectomics. Trends in Cognitive Sciences.20(5):345-61.

183. Yap P-T, Fan Y, Chen Y, Gilmore JH, Lin W, Shen D. Development Trends of White Matter Connectivity in the First Years of Life. PloS one. 2011;6(9):e24678.

184. Evans AC. Networks of anatomical covariance. NeuroImage. 2013;80(Supplement C):489-504.

185. Ratnarajah N, Rifkin-Graboi A, Fortier MV, Chong YS, Kwek K, Saw S-M, et al. Structural connectivity asymmetry in the neonatal brain. NeuroImage. 2013;75(0):187-94.

186. Zhao T, Mishra V, Jeon T, Ouyang M, Peng Q, Chalak L, et al. Structural network maturation of the preterm human brain. bioRxiv. 2017.

187. Pannek K, Hatzigeorgiou X, Colditz PB, Rose S. Assessment of Structural Connectivity in the Preterm Brain at Term Equivalent Age Using Diffusion MRI and T2 Relaxometry: A Network-Based Analysis. PloS one. 2013;8(8):e68593.

188. Brown CJ, Moriarty KP, Miller SP, Booth BG, Zwicker JG, Grunau RE, et al. Prediction of Brain Network Age and Factors of Delayed Maturation in Very Preterm Infants. In: Descoteaux M, Maier-Hein L, Franz A, Jannin P,

Collins DL, Duchesne S, editors. Medical Image Computing and Computer Assisted Intervention − MICCAI 2017: 20th International Conference, Quebec City, QC, Canada, September 11-13, 2017, Proceedings, Part I. Cham: Springer International Publishing; 2017. p. 84-91.

189. Brown CJ, Miller SP, Booth BG, Zwicker JG, Grunau RE, Synnes AR, et al. Predictive Subnetwork Extraction with Structural Priors for Infant Connectomes. In: Ourselin S, Joskowicz L, Sabuncu MR, Unal G, Wells W, editors. Medical Image Computing and Computer-Assisted Intervention – MICCAI 2016: 19th International Conference, Athens, Greece, October 17-21, 2016, Proceedings, Part I. Cham: Springer International Publishing; 2016. p. 175-83.

190. Kawahara J, Brown CJ, Miller SP, Booth BG, Chau V, Grunau RE, et al. BrainNetCNN: Convolutional neural networks for brain networks; towards predicting neurodevelopment. NeuroImage. 2017;146(Supplement C):1038-49.

191. Keunen K, Benders MJ, Leemans A, Fieret-Van Stam PC, Scholtens LH, Viergever MA, et al. White matter maturation in the neonatal brain is predictive of school age cognitive capacities in children born very preterm. Developmental Medicine & Child Neurology. 2017;59(9):939-46.

192. Tymofiyeva O, Hess CP, Ziv E, Lee PN, Glass HC, Ferriero DM, et al. A DTI-Based Template-Free Cortical Connectome Study of Brain Maturation. PloS one. 2013;8(5):e63310.

193. van den Heuvel MP, Kersbergen KJ, de Reus MA, Keunen K, Kahn RS, Groenendaal F, et al. The Neonatal Connectome During Preterm Brain

Development. Cerebral Cortex (New York, NY). 2015;25(9):3000-13.

194. van den Heuvel MP, Sporns O. Rich-Club Organization of the Human Connectome. The Journal of Neuroscience. 2011;31(44):15775-86.

195. Ball G, Aljabar P, Zebari S, Tusor N, Arichi T, Merchant N, et al. Rich-club organization of the newborn human brain. Proceedings of the National Academy of Sciences. 2014;111(20):7456-61.

196. Wee C-Y, Tuan TA, Broekman BFP, Ong MY, Chong Y-S, Kwek K, et al. Neonatal neural networks predict children behavioral profiles later in life. Human Brain Mapping. 2017;38(3):1362-73.

197. Boardman JP, Counsell SJ, Rueckert D, Kapellou O, Bhatia KK, Aljabar P, et al. Abnormal deep grey matter development following preterm birth detected using deformation-based morphometry. NeuroImage. 2006;32(1):70-8.

198. Ball G, Boardman JP, Aljabar P, Pandit A, Arichi T, Merchant N, et al. The influence of preterm birth on the developing thalamocortical connectome. Cortex. 2013;49(6):1711-21.

199. Boardman JP, Craven C, Valappil S, Counsell SJ, Dyet LE, Rueckert D, et al. A common neonatal image phenotype predicts adverse neurodevelopmental outcome in children born preterm. NeuroImage. 2010;52(2):409-14.

200. Pandit AS, Robinson E, Aljabar P, Ball G, Gousias IS, Wang Z, et al. Whole-Brain Mapping of Structural Connectivity in Infants Reveals Altered Connection Strength Associated with Growth and Preterm Birth. Cerebral cortex. 2014;24(9):2324-33.

201. Telford EJ, Cox SR, Fletcher-Watson S, Anblagan D, Sparrow S, Pataky R, et al. A latent measure explains substantial variance in white matter microstructure across the newborn human brain. Brain Structure and Function. 2017.

202. Ball G, Pazderova L, Chew A, Tusor N, Merchant N, Arichi T, et al. Thalamocortical Connectivity Predicts Cognition in Children Born Preterm. Cerebral cortex. 2015;25(11):4310-8.

203. Fischl B, Salat DH, Busa E, Albert M, Dieterich M, Haselgrove C, et al. Whole brain segmentation: automated labeling of neuroanatomical structures in the human brain. Neuron. 2002;33(3):341-55.

204. Dickie D, Shenkin S, Anblagan D, Lee JY, Blesa Cabez M, Rodriguez D, et al. Whole brain magnetic resonance image atlases: a systematic review of existing atlases and caveats for use in population imaging. Frontiers in Neuroinformatics. 2017;11(1).

205. Serag A, Aljabar P, Ball G, Counsell SJ, Boardman JP, Rutherford MA, et al. Construction of a consistent high-definition spatio-temporal atlas of the developing brain using adaptive kernel regression. Neuroimage. 2012;59(3):2255-65.

206. Makropoulos A, Aljabar P, Wright R, Hüning B, Merchant N, Arichi T, et al. Regional growth and atlasing of the developing human brain. NeuroImage. 2016;125:456-78.

207. Makropoulos A, Robinson EC, Schuh A, Wright R, Fitzgibbon S, Bozek J, et al. The Developing Human Connectome Project: a Minimal Processing Pipeline for Neonatal Cortical Surface Reconstruction. bioRxiv.

2017.

208. Makropoulos., Gousias IS, Ledig C, Aljabar P, Serag A, Hajnal JV, et al. Automatic whole brain MRI segmentation of the developing neonatal brain. IEEE transactions on medical imaging. 2014;33(9):1818-31.

209. Van Leemput K, Maes F, Vandermeulen D, Suetens P. Automated model-based tissue classification of MR images of the brain. Medical Imaging, IEEE Transactions on. 1999;18(10):897-908.

210. Brown CJ, Miller SP, Booth BG, Poskitt KJ, Chau V, Synnes AR, et al. Prediction of Motor Function in Very Preterm Infants Using Connectome Features and Local Synthetic Instances. In: Navab N, Hornegger J, Wells MW, Frangi FA, editors. Medical Image Computing and Computer-Assisted Intervention -- MICCAI 2015: 18th International Conference, Munich, Germany, October 5-9, 2015, Proceedings, Part I. Cham: Springer International Publishing; 2015. p. 69-76.

211. Behrens TE, Berg HJ, Jbabdi S, Rushworth MF, Woolrich MW. Probabilistic diffusion tractography with multiple fibre orientations: What can we gain? Neuroimage. 2007;34(1):144-55.

212. Tournier JD, Calamante F, Connelly A, editors. Improved probabilistic streamlines tractography by 2nd order integration over fibre orientation distributions. Intl Soc Mag Reson Med (ISMRM); 2010; Stockholm.

213. Toselli B, Tortora D, Severino M, Arnulfo G, Canessa A, Morana G, et al. Improvement in White Matter Tract Reconstruction with Constrained Spherical Deconvolution and Track Density Mapping in Low Angular Resolution Data: A Pediatric Study and Literature Review. Frontiers in

Pediatrics. 2017;5(182).

214. Anblagan D, Pataky R, Evans MJ, Telford EJ, Serag A, Sparrow S, et al. Association between preterm brain injury and exposure to chorioamnionitis during fetal life. 2016;6:37932.

215. Sparrow S, Manning JR, Cartier J, Anblagan D, Bastin ME, Piyasena C, et al. Epigenomic profiling of preterm infants reveals DNA methylation differences at sites associated with neural function. Translational psychiatry. 2016;6:e716.

216. Merchant N, Groves A, Larkman DJ, Counsell SJ, Thomson MA, Doria V, et al. A patient care system for early 3.0Tesla magnetic resonance imaging of very low birth weight infants. Early human development. 2009;85(12):779-83.

217. Leuchter R, Gui L, Poncet A, et al. Association between early administration of high-dose erythropoietin in preterm infants and brain mri abnormality at term-equivalent age. Jama. 2014;312(8):817-24.

218. Evans AC, Janke AL, Collins DL, Baillet S. Brain templates and atlases. NeuroImage. 2012;62(2):911-22.

219. Wilke M, Schmithorst VJ, Holland SK. Normative pediatric brain data for spatial normalization and segmentation differs from standard adult data. Magn Reson Med. 2003;50(4):749-57.

220. Muzik O, Chugani DC, Juhasz C, Shen C, Chugani HT. Statistical parametric mapping: assessment of application in children. Neuroimage. 2000;12(5):538-49.

221. Kazemi K, Moghaddam HA, Grebe R, Gondry-Jouet C, Wallois F. A

neonatal atlas template for spatial normalization of whole-brain magnetic resonance images of newborns: preliminary results. Neuroimage. 2007;37(2):463-73.

222. Kuklisova-Murgasova M, Aljabar P, Srinivasan L, Counsell SJ, Doria V, Serag A, et al. A dynamic 4D probabilistic atlas of the developing brain. Neuroimage. 2011;54(4):2750-63.

223. Yoon U, Fonov VS, Perusse D, Evans AC. The effect of template choice on morphometric analysis of pediatric brain data. NeuroImage. 2009;45(3):769-77.

224. Vardhan A, Prastawa M, Vachet C, Piven J, Gerig G. Characterizing growth patterns in longitudinal MRI using image contrast. Proceedings of SPIE--the International Society for Optical Engineering. 2014;9034:90340D.

225. Serag A, Aljabar P, Counsell S, Boardman J, Hajnal JV, Rueckert D, editors. Tracking developmental changes in subcortical structures of the preterm brain using multi-modal MRI. Biomedical Imaging: From Nano to Macro, 2011 IEEE International Symposium on; 2011 March 30 2011-April 2 2011.

226. Knickmeyer RC, Gouttard S, Kang C, Evans D, Wilber K, Smith JK, et al. A structural MRI study of human brain development from birth to 2 years. J Neurosci. 2008;28(47):12176-82.

227. Matsuzawa J, Matsui M, Konishi T, Noguchi K, Gur RC, Bilker W, et al. Age-related volumetric changes of brain gray and white matter in healthy infants and children. Cerebral cortex. 2001;11(4):335-42.

228. Paus T, Collins DL, Evans AC, Leonard G, Pike B, Zijdenbos A.

Maturation of white matter in the human brain: a review of magnetic resonance studies. Brain Research Bulletin. 2001;54(3):255-66.

229. Lenroot RK, Giedd JN. Brain development in children and adolescents: Insights from anatomical magnetic resonance imaging. Neuroscience & Biobehavioral Reviews. 2006;30(6):718-29.

230. Sanchez CE, Richards JE, Almli CR. Age-specific MRI templates for pediatric neuroimaging. Developmental Neuropsychology. 2012;37(5):379-99.

231. Sanchez CE, Richards JE, Almli CR. Neurodevelopmental MRI brain templates for children from 2 weeks to 4 years of age. Developmental psychobiology. 2012;54(1):77-91.

232. Richards JE, Sanchez C, Phillips-Meek M, Xie W. A database of age-appropriate average MRI templates. NeuroImage. 2016;124, Part B:1254-9.

233. Fillmore PT, Richards JE, Phillips-Meek MC, Cryer A, Stevens M. Stereotaxic MRI brain atlases for infants from 3 to 12 months. Developmental neuroscience. 2015;37(6):515-32.

234. Gilmore JH, Lin W, Prastawa MW, Looney CB, Vetsa YS, Knickmeyer RC, et al. Regional gray matter growth, sexual dimorphism, and cerebral asymmetry in the neonatal brain. J Neurosci. 2007;27(6):1255-60.

235. Gousias IS, Edwards AD, Rutherford MA, Counsell SJ, Hajnal JV, Rueckert D, et al. Magnetic resonance imaging of the newborn brain: manual segmentation of labelled atlases in term-born and preterm infants. Neuroimage. 2012;62(3):1499-509.

236. Tzourio-Mazoyer N, Landeau B, Papathanassiou D, Crivello F, Etard

O, Delcroix N, et al. Automated anatomical labeling of activations in SPM using a macroscopic anatomical parcellation of the MNI MRI single-subject brain. Neuroimage. 2002;15(1):273-89.

237. Kabdebon C, Leroy F, Simmonet H, Perrot M, Dubois J, Dehaene-Lambertz G. Anatomical correlations of the international 10–20 sensor placement system in infants. NeuroImage. 2014;99(0):342-56.

238. Alexander B, Murray A, Chen J, Loh WY, Kelly C, Beare R, et al., editors. Novel probabilistic neonatal cortical brain atlas. ISMRM; 2015.

239. Desikan RS, Ségonne F, Fischl B, Quinn BT, Dickerson BC, Blacker D, et al. An automated labeling system for subdividing the human cerebral cortex on MRI scans into gyral based regions of interest. NeuroImage. 2006;31(3):968-80.

240. Shi F, Yap PT, Wu G, Jia H, Gilmore JH, Lin W, et al. Infant brain atlases from neonates to 1- and 2-year-olds. PloS one. 2011;6(4):e18746.

241. Wu J, Ashtari M, Betancourt LM, Brodsky NL, Giannetta JM, Gee JC, et al., editors. Cortical parcellation for neonatal brains. Biomedical Imaging (ISBI), 2014 IEEE 11th International Symposium on; 2014: IEEE.

242. Makropoulos A, Gousias IS, Ledig C, Aljabar P, Serag A, Hajnal JV, et al. Automatic whole brain MRI segmentation of the developing neonatal brain. IEEE transactions on medical imaging. 2014;33(9):1818-31.

243. Makropoulos A, Aljabar P, Wright R, Huning B, Merchant N, Arichi T, et al. Regional growth and atlasing of the developing human brain. Neuroimage. 2016;125:456-78.

244. Oishi K, Mori S, Donohue PK, Ernst T, Anderson L, Buchthal S, et al.

Multi-contrast human neonatal brain atlas: Application to normal neonate development analysis. NeuroImage. 2011;56(1):8-20.

245. Zhang Y, Chang L, Ceritoglu C, Skranes J, Ernst T, Mori S, et al. A Bayesian approach to the creation of a study-customized neonatal brain atlas. NeuroImage. 2014;101(0):256-67.

246. Serag A, Aljabar P, Counsell S, Boardman J, Hajnal JV, Rueckert D, editors. LISA: Longitudinal image registration via spatio-temporal atlases. Biomedical Imaging (ISBI), 2012 9th IEEE International Symposium on; 2012 2-5 May 2012.

247. Rohlfing T, Zahr NM, Sullivan EV, Pfefferbaum A. The SRI24 multichannel atlas of normal adult human brain structure. Hum Brain Mapp. 2010;31(5):798-819.

248. Fonov V, Evans AC, McKinstry RC, Almli CR, and Collins DL. Unbiased nonlinear average age-appropriate brain templates from birth to adulthood Neuroimage. 2009;47.

249. Fonov., Evans AC, Botteron K, Almli CR, McKinstry RC, Collins DL. Unbiased average age-appropriate atlases for pediatric studies. NeuroImage. 2011;54(1):313-27.

250. Avants BB, Yushkevich P, Pluta J, Minkoff D, Korczykowski M, Detre J, et al. The optimal template effect in hippocampus studies of diseased populations. NeuroImage. 2010;49(3):2457-66.

251. Meijering EHW. Spline interpolation in medical imaging: Comparison with other convolution-based approaches. European Signal Processing Conference; 4-8 Sept. ; Tampere, Finland2000.

252. Cook P, Bai Y, Nedjati-Gilani S, Seunarine K, Hall M, Parker G, et al. Camino: open-source diffusion-MRI reconstruction and processing. 14th scientific meeting of the international society for magnetic resonance in medicine. 2006;2759.

253. Modat M, Ridgway GR, Taylor ZA, Lehmann M, Barnes J, Hawkes DJ, et al. Fast free-form deformation using graphics processing units. Computer Methods and Programs in Biomedicine. 2010;98(3):278-84.

254. Ourselin S, Roche A, Subsol G, Pennec X, Ayache N. Reconstructing a 3D structure from serial histological sections. Image and Vision Computing. 2001;19(1–2):25-31.

255. Studholme C, Hill DLG, Hawkes DJ. An overlap invariant entropy measure of 3D medical image alignment. Pattern Recognition. 1999;32(1):71-86.

256. Serag A, Blesa M, Moore EJ, Pataky R, Sparrow SA, Wilkinson AG, et al. Accurate Learning with Few Atlases (ALFA): an algorithm for MRI neonatal brain extraction and comparison with 11 publicly available methods. Scientific Reports. 2016;6:23470.

257. Tustison NJ, Avants BB, Cook PA, Zheng Y, Egan A, Yushkevich PA, et al. N4ITK: improved N3 bias correction. IEEE transactions on medical imaging. 2010;29(6):1310-20.

258. Serag A, Gousias I, Makropoulos A, Aljabar P, Hajnal J, Boardman J, et al. Unsupervised Learning of Shape Complexity: Application to Brain Development. In: Durrleman S, Fletcher T, Gerig G, Niethammer M, editors. Spatio-temporal Image Analysis for Longitudinal and Time-Series Image

Data. Lecture Notes in Computer Science. 7570: Springer Berlin Heidelberg; 2012. p. 88-99.

259. Serag A, Kyriakopoulou V, Rutherford MA, Edwards AD, Hajnal JV, Aljabar P, et al. A Multi-channel 4D Probabilistic Atlas of the Developing Brain: Application to Fetuses and Neonates. Annals of the BMVA. 2012;2012(3):1-14.

260. Yoo J-C, Han TH. Fast Normalized Cross-Correlation. Circuits, Systems and Signal Processing. 2009;28(6):819-43.

261. Avants BB, Duda JT, Kilroy E, Krasileva K, Jann K, Kandel BT, et al. The pediatric template of brain perfusion. Scientific Data. 2015;2:150003.

262. Zhan J, Dinov ID, Li J, Zhang Z, Hobel S, Shi Y, et al. Spatial–temporal atlas of human fetal brain development during the early second trimester. NeuroImage. 2013;82:115-26.

263. Avants BB, Tustison NJ, Song G, Cook PA, Klein A, Gee JC. A reproducible evaluation of ANTs similarity metric performance in brain image registration. Neuroimage. 2011;54(3):2033-44.

264. Heckemann RA, Hajnal JV, Aljabar P, Rueckert D, Hammers A. Automatic anatomical brain MRI segmentation combining label propagation and decision fusion. NeuroImage. 2006;33(1):115-26.

265. Noorizadeh N, Kazemi K, Grebe R, Helfroush MS, Mahmoudzadeh M, Wallois F. A Tool to Investigate Symmetry Properties of Newborns Brain: The Newborns' Symmetric Brain Atlas. ISRN Neuroscience. 2013;2013:317215.

266. Toga AW, Thompson PM. Mapping brain asymmetry. Nat Rev Neurosci. 2003;4(1):37-48.

267. Klein A, Worth A, Tourville J, Landman B, Dal Canton T, Ghosh S, et al. An interactive tool for constructing optimal brain colormaps. Society for Neuroscience2010.

268. Bayer A, Altman J. The Human Brain During the Third Trimester: CRC Press; 2003.

269. Yushkevich PA, Piven J, Hazlett HC, Smith RG, Ho S, Gee JC, et al. User-guided 3D active contour segmentation of anatomical structures: significantly improved efficiency and reliability. Neuroimage. 2006;31(3):1116-28.

270. Black KJ, Koller JM, Snyder AZ, Perlmutter JS. Template Images for Nonhuman Primate Neuroimaging: 2. Macaque. NeuroImage. 2001;14(3):744-8.

271. Love SA, Marie D, Roth M, Lacoste R, Nazarian B, Bertello A, et al. The average baboon brain: MRI templates and tissue probability maps from 89 individuals. NeuroImage. 2016;132:526-33.

272. Ella A, Keller M. Construction of an MRI 3D high resolution sheep brain template. Magnetic Resonance Imaging. 2015;33(10):1329-37.

273. McLaren DG, Kosmatka KJ, Oakes TR, Kroenke CD, Kohama SG, Matochik JA, et al. A population-average MRI-based atlas collection of the rhesus macaque. NeuroImage. 2009;45(1):52-9.

274. Luders E, Gaser C, Jancke L, Schlaug G. A voxel-based approach to gray matter asymmetries. NeuroImage. 2004;22(2):656-64.

275. Dubois J, Benders M, Lazeyras F, Borradori-Tolsa C, Leuchter RH, Mangin JF, et al. Structural asymmetries of perisylvian regions in the preterm

newborn. Neuroimage. 2010;52(1):32-42.

276. Jenkinson M, Beckmann CF, Behrens TE, Woolrich MW, Smith SM. Fsl. Neuroimage. 2012;62(2):782-90.

277. Armstrong E, Schleicher A, Omran H, Curtis M, Zilles K. The Ontogeny of Human Gyrification. Cerebral cortex. 1995;5(1):56-63.

278. van der Knaap MS, van Wezel-Meijler G, Barth PG, Barkhof F, Ader HJ, Valk J. Normal gyration and sulcation in preterm and term neonates: appearance on MR images. Radiology. 1996;200(2):389-96.

279. Pienaar R, Fischl B, Caviness V, Makris N, Grant PE. A METHODOLOGY FOR ANALYZING CURVATURE IN THE DEVELOPING BRAIN FROM PRETERM TO ADULT. International journal of imaging systems and technology. 2008;18(1):42-68.

280. Shi F, Fan Y, Tang S, Gilmore JH, Lin W, Shen D. Neonatal brain image segmentation in longitudinal MRI studies. Neuroimage. 2010;49(1):391-400.

281. Beg MF, Miller M, Trouvé A, Younes L. Computing Large Deformation Metric Mappings via Geodesic Flows of Diffeomorphisms. Int J Comput Vision. 2005;61(2):139-57.

282. Boardman JP, Counsell SJ, Rueckert D, Hajnal JV, Bhatia KK, Srinivasan L, et al. Early growth in brain volume is preserved in the majority of preterm infants. Annals of neurology. 2007;62(2):185-92.

283. Thompson DK, Inder TE, Faggian N, Johnston L, Warfield SK, Anderson PJ, et al. Characterization of the corpus callosum in very preterm and full-term infants utilizing MRI. NeuroImage. 2011;55(2):479-90.

284. Ashburner J, Friston KJ. Voxel-Based Morphometry—The Methods. NeuroImage. 2000;11(6):805-21.

285. Serag A, Boardman JP, Wilkinson AG, Macnaught G, Semple SI, editors. A sparsity-based atlas selection technique for multiple-atlas segmentation: Application to neonatal brain labeling. 2016 24th Signal Processing and Communication Application Conference (SIU); 2016 16-19 May 2016.

286. Antonova E, Kumari V, Morris R, Halari R, Anilkumar A, Mehrotra R, et al. The Relationship of Structural Alterations to Cognitive Deficits in Schizophrenia: A Voxel-Based Morphometry Study. Biological psychiatry.58(6):457-67.

287. Job DE, Dickie DA, Rodriguez D, Robson A, Pernet C, Bastin ME, et al. A brain imaging repository of normal structural MRI across the life course: Brain Images of Normal Subjects (BRAINS). Neuroimage. 2016.

288. Pestilli F, Yeatman JD, Rokem A, Kay KN, Wandell BA. Evaluation and statistical inference for human connectomes. Nat Meth. 2014;11(10):1058-63.

289. Smith RE, Tournier J-D, Calamante F, Connelly A. SIFT: Spherical-deconvolution informed filtering of tractograms. NeuroImage. 2013;67:298-312.

290. Colby JB, Soderberg L, Lebel C, Dinov ID, Thompson PM, Sowell ER. Along-tract statistics allow for enhanced tractography analysis. NeuroImage. 2012;59(4):3227-42.

291. Ritchie SJ, Bastin ME, Tucker-Drob EM, Maniega SM, Engelhardt LE,

Cox SR, et al. Coupled changes in brain white matter microstructure and fluid intelligence in later life. The Journal of neuroscience : the official journal of the Society for Neuroscience. 2015;35(22):8672-82.

292. Berman JI, Mukherjee P, Partridge SC, Miller SP, Ferriero DM, Barkovich AJ, et al. Quantitative diffusion tensor MRI fiber tractography of sensorimotor white matter development in premature infants. NeuroImage. 2005;27(4):862-71.

293. Partridge SC, Mukherjee P, Berman JI, Henry RG, Miller SP, Lu Y, et al. Tractography-based quantitation of diffusion tensor imaging parameters in white matter tracts of preterm newborns. Journal of Magnetic Resonance Imaging. 2005;22(4):467-74.

294. Dubois J, Dehaene-Lambertz G, Soarès C, Cointepas Y, Le Bihan D, Hertz-Pannier L. Microstructural Correlates of Infant Functional Development: Example of the Visual Pathways. The Journal of Neuroscience. 2008;28(8):1943-8.

295. Gong G, Jiang T, Zhu C, Zang Y, Wang F, Xie S, et al. Asymmetry analysis of cingulum based on scale-invariant parameterization by diffusion tensor imaging. Human Brain Mapping. 2005;24(2):92-8.

296. Yeatman JD, Dougherty RF, Myall NJ, Wandell BA, Feldman HM. Tract Profiles of White Matter Properties: Automating Fiber-Tract Quantification. PloS one. 2012;7(11):e49790.

297. Pecheva D, Yushkevich P, Batalle D, Hughes E, Aljabar P, Wurie J, et al. A tract-specific approach to assessing white matter in preterm infants. NeuroImage. 2017.

298. Yushkevich PA, Zhang H, Simon TJ, Gee JC. Structure-specific statistical mapping of white matter tracts. NeuroImage. 2008;41(2):448-61.

299. Serag A, Wilkinson A, Telford E, Pataky R, Sparrow S, Anblagan D, et al. SEGMA: an automatic SEGMentation Approach for human brain MRI using sliding window and random forests. Frontiers in Neuroinformatics. 2017;11(2).

300. Veraart J, Novikov DS, Christiaens D, Ades-aron B, Sijbers J, Fieremans E. Denoising of diffusion MRI using random matrix theory. NeuroImage. 2016.

301. Tournier JD, Calamante F, Connelly A. MRtrix: Diffusion tractography in crossing fiber regions. International Journal of Imaging Systems and Technology. 2012;22(1):53-66.

302. Tournier JD, Calamante F, Connelly A. Robust determination of the fibre orientation distribution in diffusion MRI: non-negativity constrained super-resolved spherical deconvolution. Neuroimage. 2007;35(4):1459-72.

303. Veraart J, Fieremans E, Novikov DS. Diffusion MRI noise mapping using random matrix theory. Magnetic Resonance in Medicine. 2016;76(5):1582-93.

304. Leemans A, Jones DK. The B-matrix must be rotated when correcting for subject motion in DTI data. Magn Reson Med. 2009;61(6):1336-49.

305. Wu M, Chang LC, Walker L, Lemaitre H, Barnett AS, Marenco S, et al. Comparison of EPI Distortion Correction Methods in Diffusion Tensor MRI Using a Novel Framework. Medical image computing and computer-assisted intervention : MICCAI International Conference on Medical Image

Computing and Computer-Assisted Intervention. 2008;11(Pt 2):321-9.

306. Irfanoglu MO, Walker L, Sarlls J, Marenco S, Pierpaoli C. Effects of image distortions originating from susceptibility variations and concomitant fields on diffusion MRI tractography results. Neuroimage. 2012;61(1):275-88.

307. Pluim JPW, Maintz JBA, Viergever MA. Mutual-information-based registration of medical images: a survey. Medical Imaging, IEEE Transactions on. 2003;22(8):986-1004.

308. Avants BB, Tustison NJ, Wu J, Cook PA, Gee JC. An Open Source Multivariate Framework for n-Tissue Segmentation with Evaluation on Public Data. Neuroinformatics. 2011;9(4):381-400.

309. Tournier JD, Calamante F, Connelly A. Determination of the appropriate b value and number of gradient directions for high-angular-resolution diffusion-weighted imaging. NMR in biomedicine. 2013;26(12):1775-86.

310. Takemura H, Caiafa CF, Wandell BA, Pestilli F. Ensemble Tractography. PLoS computational biology. 2016;12(2):e1004692.

311. Qi S, Meesters S, Nicolay K, ter Haar Romeny BM, Ossenblok P. Structural brain network: What is the effect of LiFE optimization of whole brain tractography? Frontiers in Computational Neuroscience. 2016;10.

312. Maier-Hein KH, Neher PF, Houde J-C, Côté M-A, Garyfallidis E, Zhong J, et al. The challenge of mapping the human connectome based on diffusion tractography. Nature Communications. 2017;8(1):1349.

313. Smith RE, Tournier JD, Calamante F, Connelly A. SIFT2: Enabling dense quantitative assessment of brain white matter connectivity using

streamlines tractography. Neuroimage. 2015;119:338-51.

314. Calamante F, Tournier J-D, Jackson GD, Connelly A. Track-density imaging (TDI): Super-resolution white matter imaging using whole-brain track-density mapping. NeuroImage. 2010;53(4):1233-43.

315. Conti E, Mitra J, Calderoni S, Pannek K, Shen KK, Pagnozzi A, et al. Network over-connectivity differentiates autism spectrum disorder from other developmental disorders in toddlers: A diffusion MRI study. Human Brain Mapping. 2017;38(5):2333-44.

316. Benjamini Y, Hochberg Y. Controlling the False Discovery Rate: A Practical and Powerful Approach to Multiple Testing. Journal of the Royal Statistical Society Series B (Methodological). 1995;57(1):289-300.

317. Xia M, Wang J, He Y. BrainNet Viewer: A Network Visualization Tool for Human Brain Connectomics. PloS one. 2013;8(7):e68910.

318. Gu Z, Gu L, Eils R, Schlesner M, Brors B. circlize implements and enhances circular visualization in R. Bioinformatics. 2014;30(19):2811-2.

319. Clayden JD, Storkey AJ, Bastin ME. A probabilistic model-based approach to consistent white matter tract segmentation. IEEE transactions on medical imaging. 2007;26(11):1555-61.

320. Raffelt D, Tournier JD, Rose S, Ridgway GR, Henderson R, Crozier S, et al. Apparent Fibre Density: a novel measure for the analysis of diffusion-weighted magnetic resonance images. Neuroimage. 2012;59(4):3976-94.

321. Dyrby TB, Lundell H, Burke MW, Reislev NL, Paulson OB, Ptito M, et al. Interpolation of diffusion weighted imaging datasets. NeuroImage. 2014;103:202-13.

322. Zalesky A, Fornito A, Cocchi L, Gollo LL, van den Heuvel MP, Breakspear M. Connectome sensitivity or specificity: which is more important? NeuroImage. 2016;142:407-20.

323. Kellner E, Dhital B, Kiselev VG, Reisert M. Gibbs-ringing artifact removal based on local subvoxel-shifts. Magnetic Resonance in Medicine. 2016;76(5):1574-81.

324. Counsell SJ, Edwards AD, Chew ATM, Anjari M, Dyet LE, Srinivasan L, et al. Specific relations between neurodevelopmental abilities and white matter microstructure in children born preterm. Brain. 2008;131(12):3201-8.

325. van Kooij BJM, de Vries LS, Ball G, van Haastert IC, Benders MJNL, Groenendaal F, et al. Neonatal Tract-Based Spatial Statistics Findings and Outcome in Preterm Infants. American Journal of Neuroradiology. 2012;33(1):188-94.

326. Boardman JP, Walley A, Ball G, Takousis P, Krishnan ML, Hughes-Carre L, et al. Common Genetic Variants and Risk of Brain Injury After Preterm Birth. Pediatrics. 2014;133(6):e1655-e63.

327. Krishnan ML, Van Steenwinckel J, Schang A-L, Yan J, Arnadottir J, Le Charpentier T, et al. Integrative genomics of microglia implicates DLG4 (PSD95) in the white matter development of preterm infants. Nature Communications. 2017;8(1):428.

328. Morgan C, McGowan P, Herwitker S, Hart AE, Turner MA. Postnatal Head Growth in Preterm Infants: A Randomized Controlled Parenteral Nutrition Study. Pediatrics. 2013.

329. Beauport L, Schneider J, Faouzi M, Hagmann P, Hüppi PS, Tolsa J-F,

et al. Impact of Early Nutritional Intake on Preterm Brain: A Magnetic Resonance Imaging Study. The Journal of Pediatrics. 2017;181:29-36.e1.

330. Horta BL, Loret de Mola C, Victora CG. Breastfeeding and intelligence: a systematic review and meta-analysis. Acta Paediatrica. 2015;104:14-9.

331. Belfort MB, Anderson PJ, Nowak VA, Lee KJ, Molesworth C, Thompson DK, et al. Breast Milk Feeding, Brain Development, and Neurocognitive Outcomes: A 7-Year Longitudinal Study in Infants Born at Less Than 30 Weeks' Gestation. The Journal of Pediatrics. 2016;177:133-9.e1.

332. Horwood LJ, Fergusson DM. Breastfeeding and Later Cognitive and Academic Outcomes. Pediatrics. 1998;101(1):e9-e.

333. Luby JL, Belden AC, Whalen D, Harms MP, Barch DM. Breastfeeding and Childhood IQ: The Mediating Role of Gray Matter Volume. Journal of the American Academy of Child and Adolescent Psychiatry. 2016;55(5):367-75.

334. Kafouri S, Kramer M, Leonard G, Perron M, Pike B, Richer L, et al. Breastfeeding and brain structure in adolescence. International Journal of Epidemiology. 2013;42(1):150-9.

335. Deoni SC, Dean DC, 3rd, Piryatinsky I, O'Muircheartaigh J, Waskiewicz N, Lehman K, et al. Breastfeeding and early white matter development: A cross-sectional study. Neuroimage. 2013;82:77-86.

336. Villar J, Giuliani F, Fenton TR, Ohuma EO, Ismail LC, Kennedy SH. INTERGROWTH-21st very preterm size at birth reference charts. The Lancet. 2016;387(10021):844-5.

337. Smith SM, Jenkinson M, Woolrich MW, Beckmann CF, Behrens TEJ, Johansen-Berg H, et al. Advances in functional and structural MR image analysis and implementation as FSL. NeuroImage. 2004;23, Supplement 1(0):S208-S19.

338. Smith SM. Fast robust automated brain extraction. Human Brain Mapping. 2002;17(3):143-55.

339. Tournier JD, Yeh C-H, Calamante F, Cho K-H, Connelly A, Lin C-P. Resolving crossing fibres using constrained spherical deconvolution: Validation using diffusion-weighted imaging phantom data. NeuroImage. 2008;42(2):617-25.

340. Yeh C-H, Smith RE, Liang X, Calamante F, Connelly A. Correction for diffusion MRI fibre tracking biases: The consequences for structural connectomic metrics. NeuroImage. 2016.

341. de Reus MA, van den Heuvel MP. Estimating false positives and negatives in brain networks. NeuroImage. 2013;70:402-9.

342. Watts DJ, Strogatz SH. Collective dynamics of /`small-world/' networks. Nature. 1998;393(6684):440-2.

343. Latora V, Marchiori M. Efficient behavior of small-world networks. Physical review letters. 2001;87(19):198701.

344. Achard S, Bullmore E. Efficiency and Cost of Economical Brain Functional Networks. PLoS computational biology. 2007;3(2):e17.

345. Onoda K, Yamaguchi S. Dissociative contributions of the anterior cingulate cortex to apathy and depression: Topological evidence from resting-state functional MRI. Neuropsychologia. 2015;77:10-8.

346. Yeh C, Smith RE, Dhollander T, Calamante F, Connelly A, editors. The influence of node assignment strategies and track termination criteria on diffusion MRI-based structural connectomics. Intl Soc Mag Reson Med (ISMRM); 2016; Singapore.

347. Bordier C, Nicolini C, Bifone A. Graph Analysis and Modularity of Brain Functional Connectivity Networks: Searching for the Optimal Threshold. Frontiers in Neuroscience. 2017;11(441).

348. Wang J, Wang L, Zang Y, Yang H, Tang H, Gong Q, et al. Parcellation-dependent small-world brain functional networks: A resting-state fMRI study. Human Brain Mapping. 2009;30(5):1511-23.

349. Zalesky A, Solowij N, Yücel M, Lubman DI, Takagi M, Harding IH, et al. Effect of long-term cannabis use on axonal fibre connectivity. Brain. 2012;135(7):2245-55.

350. Winkler AM, Ridgway GR, Webster MA, Smith SM, Nichols TE. Permutation inference for the general linear model. NeuroImage. 2014;92:381-97.

351. Smith SM, Nichols TE. Threshold-free cluster enhancement: Addressing problems of smoothing, threshold dependence and localisation in cluster inference. NeuroImage. 2009;44(1):83-98.

352. Patra K, Hamilton M, Johnson TJ, Greene M, Dabrowski E, Meier PP, et al. NICU Human Milk Dose and 20-Month Neurodevelopmental Outcome in Very Low Birth Weight Infants. Neonatology. 2017;112(4):330-6.

353. Agostoni C, Buonocore G, Carnielli V, De Curtis M, Darmaun D, Decsi T, et al. Enteral Nutrient Supply for Preterm Infants: Commentary From the

European Society of Paediatric Gastroenterology, Hepatology and Nutrition Committee on Nutrition. Journal of Pediatric Gastroenterology and Nutrition. 2010;50(1):85-91.

354. Guesnet P, Alessandri JM. Docosahexaenoic acid (DHA) and the developing central nervous system (CNS) - Implications for dietary recommendations. Biochimie. 2011;93(1):7-12.

355. Pannaraj PS, Li F, Cerini C, et al. Association between breast milk bacterial communities and establishment and development of the infant gut microbiome. JAMA pediatrics. 2017;171(7):647-54.

356. Heijtz RD, Wang S, Anuar F, Qian Y, Björkholm B, Samuelsson A, et al. Normal gut microbiota modulates brain development and behavior. Proceedings of the National Academy of Sciences. 2011;108(7):3047-52.

357. Carlson AL, Xia K, Azcarate-Peril MA, Goldman BD, Ahn M, Styner MA, et al. Infant Gut Microbiome Associated With Cognitive Development. Biological psychiatry. 2017.

358. Caspi A, Williams B, Kim-Cohen J, Craig IW, Milne BJ, Poulton R, et al. Moderation of breastfeeding effects on the IQ by genetic variation in fatty acid metabolism. Proceedings of the National Academy of Sciences. 2007;104(47):18860-5.

359. Steer CD, Davey Smith G, Emmett PM, Hibbeln JR, Golding J. FADS2 polymorphisms modify the effect of breastfeeding on child IQ. PloS one. 2010;5(7):e11570.

360. Krishnan ML, Wang Z, Silver M, Boardman JP, Ball G, Counsell SJ, et al. Possible relationship between common genetic variation and white matter

development in a pilot study of preterm infants. Brain and behavior. 2016;6(7):e00434.

361. Smith RE, Tournier JD, Calamante F, Connelly A. The effects of SIFT on the reproducibility and biological accuracy of the structural connectome. Neuroimage. 2015;104:253-65.

362. Salvan P, Tournier JD, Batalle D, Falconer S, Chew A, Kennea N, et al. Language ability in preterm children is associated with arcuate fasciculi microstructure at term. Human Brain Mapping. 2017;38(8):3836-47.

363. Takemura H, Rokem A, Winawer J, Yeatman JD, Wandell BA, Pestilli F. A Major Human White Matter Pathway Between Dorsal and Ventral Visual Cortex. Cerebral cortex. 2016;26(5):2205-14.

364. Daducci A, Dal Palú A, Descoteaux M, Thiran J-P. Microstructure Informed Tractography: Pitfalls and Open Challenges. Frontiers in Neuroscience. 2016;10(247).

365. Ngo GC, C.; Vu, C.; Cerjanic, A.; Muthaiya, M.; Drottar, M.; Litt, J.; Frantz, I.; Larsen, R.; Gagoski, B.; Ellen Grant, P.; and Sutton, B.P., editor Assessing white matter tract development in formula fed versus breastfed infants at 1 month and 3 months. International Society of Magnetic Resonance in Medicine; 2017; Honolulu.

366. Ottolini KMA, N.; Kapse, K.; Limperopoulos, C., editor Impact of breastmilk on brain microstructural development in VLBW infants. Pediatric Academy Societies; 2017.

367. Caruyer E, Lenglet C, Sapiro G, Deriche R. Design of multishell sampling schemes with uniform coverage in diffusion MRI. Magnetic

Resonance in Medicine. 2013;69(6):1534-40.

368. Andersson JLR, Sotiropoulos SN. An integrated approach to correction for off-resonance effects and subject movement in diffusion MR imaging. Neuroimage. 2016;125:1063-78.

369. Andersson JLR, Graham MS, Zsoldos E, Sotiropoulos SN. Incorporating outlier detection and replacement into a non-parametric framework for movement and distortion correction of diffusion MR images. NeuroImage. 2016;141(Supplement C):556-72.

370. Andersson JLR, Skare S, Ashburner J. How to correct susceptibility distortions in spin-echo echo-planar images: application to diffusion tensor imaging. NeuroImage. 2003;20(2):870-88.

371. Andersson JLR, Sotiropoulos SN. Non-parametric representation and prediction of single- and multi-shell diffusion-weighted MRI data using Gaussian processes. NeuroImage. 2015;122:166-76.

372. Andersson JLR, Graham MS, Drobnjak I, Zhang H, Filippini N, Bastiani M. Towards a comprehensive framework for movement and distortion correction of diffusion MR images: Within volume movement. Neuroimage. 2017;152:450-66.

373. Schuh A, Makropoulos A, Wright R, Robinson EC, Tusor N, Steinweg J, et al., editors. A deformable model for the reconstruction of the neonatal cortex. 2017 IEEE 14th International Symposium on Biomedical Imaging (ISBI 2017); 2017 18-21 April 2017.

374. Wang S, Peterson DJ, Gatenby JC, Li W, Grabowski TJ, Madhyastha TM. Evaluation of Field Map and Nonlinear Registration Methods for

Correction of Susceptibility Artifacts in Diffusion MRI. Frontiers in Neuroinformatics. 2017;11:17.

375. Ment LR, Hirtz D, Huppi PS. Imaging biomarkers of outcome in the developing preterm brain. The Lancet Neurology. 2009;8(11):1042-55.

376. Caiafa CF, Pestilli F. Multidimensional encoding of brain connectomes. Scientific Reports. 2017;7(1):11491.

377. Jeurissen B, Tournier J-D, Dhollander T, Connelly A, Sijbers J. Multi-tissue constrained spherical deconvolution for improved analysis of multi-shell diffusion MRI data. NeuroImage. 2014;103(Supplement C):411-26.

378. Cao M, Huang H, He Y. Developmental Connectomics from Infancy through Early Childhood. Trends in Neurosciences. 2017;40(8):494-506.

Appendix 1

The following table explains the parameters used in the calculation of the structural connectivity of the chapters four and five.

Table A1: Detailed parameters of the steps involved in connectome creation

Step	Chapter 4	Chapter 5
Denoising of the dMRI	dwidenoise (mrtrix RC1) default parameters	dwidenoise (mrtrix RC2) default parameters
Upsampling of the dMRI	mrresize (mrtrix RC1) -vox 1,1,1	mrresize (mrtrix rc2) -scale 2
Eddy current correction	eddy_correct (FSL) default parameters	
Skull stripping	Propagated from the T1w to the fisrst B0 (Niftyreg) using affine and nonrigid registration (default parameters)	bet2 (FSL) -f 0.3 on the main B0 + manual editting
Bias field correction of the dMRI	dwibiascorrect (mrtrix RC1) default parameters	dwibiascorrect (mrtrix RC2) default parameters
Bias field correction T1w	N4BiasFieldCorrection (ANTs) default parameters	
Skull stripping T1w	ALFA default parameters*	
EPI distortion	T1w to first B0 rigid registration (Niftyreg) default	

correction	parameters; Non-rigid registration restricted to the phase encoded direction of the B0 to the co-registered T1w (ANTs) SyN registration, -g 1x0x0 and mutual information	
Tissue segmentation of the aligned T1w	antsRegistration (ANTs) with the recommended parameters for large deformation** + Segma default parameters*	
Parcellation of the aligned T1w	antsRegistration (ANTs) with the recommended parameters for large deformation**	
Response function calculation	dwi2response (mrtrix RC1) tournier algorithm with default parameters	dwi2response (mrtrix RC2) tournier algorithm with default parameters
FOD calculation	dwi2fod (mrtrix RC1) csd algorithm with default parameters	dwi2fod (mrtrix RC2) csd algorithm with default parameters
Tractography	tckgen (mrtrix RC1) iFOD2 algorithm, -cutoff 0.15, -number 100000 and ACT default parameters for up-sampled data	tckgen (mrtrix RC2) iFOD2 algorithm, -number 10000000 and ACT default parameters for up-sampled data
Filtering tractogram	LiFE default parameters on a mask created from the WM tracts using	tcksift (mrtrix RC2) with act image, -term_number 2000000 and -

	tckmap -contrast tdi and threshold to a value of 1	fd_scale_gm
Tensor maps creation	dtifit (FSL) with -w	
Connectome creation	tck2connectome (mrtrix RC1) with -assignment_end_voxels and -zero_diagonal on the streamline weighted connectome	tck2connectome (mrtrix RC2) with -assignment_end_voxels and -zero_diagonal on the streamline weighted connectome the FA weighted, created using tcksample -stat_tck mean and the options -scale_file, -assignment_end_voxels, -zero_diagonal and -stat_edge mean in tck2connectome

*For this algorithm there are not default parameters, only guidelines about his performance with different datasets, including our dataset. For the recommended values, please see the original publications

**The parameters for large deformation are extracted from the ANTs manual (http://stnava.github.io/ANTs/)